Trapping and Plasmon-Enhanced Emission from a Single Upconverting Nanocrystal

by

Amirhossein AlizadehKhaledi

B.Sc., Iran University of Science and Technology, 2013

M.Sc., Tarbiat Modares University, 2016

A Dissertation Submitted in Partial Fulfillment
of the Requirements for the Degree of

DOCTOR OF PHILOSOPHY

in the Department of Electrical and Computer Engineering

University of Victoria

Supervisory Committee

Trapping and Plasmon-Enhanced Emission from a Single Upconverting Nanocrystal

by

Amirhossein AlizadehKhaledi

B.Sc., Iran University of Science and Technology, 2013

M.Sc., Tarbiat Modares University, 2016

Supervisory Committee

Dr. Reuven Gordon, Department of Electrical and Computer Engineering

Supervisor

Dr. Thomas Tiedje, Department of Electrical and Computer Engineering

Departmental Member

Dr. David Harrington, Department of Chemistry

Outside Member

Abstract

Supervisory Committee

Dr. Reuven Gordon, Department of Electrical and Computer Engineering

Supervisor

Dr. Thomas Tiedje, Department of Electrical and Computer Engineering

Departmental Member

David Harrington, Department of Chemistry

Outside Member

Plasmonics has been used to increase the interaction of an emitter and light. This enhancement can be achieved by using plasmonic resonators at the emission and/or absorption wavelengths of the emitter. This dissertation is based on four projects which are mainly about the interaction of light and upconversion nanocrystals (UCNCs) using plasmonic resonators.

In the first project, rectangular apertures on a gold film are fabricated and used to trap and study single UCNC. These apertures are finely tuned to find the highest upconversion emission enhancement. Results show significant up to 400× enhancement along with many other interesting observations for trapped UCNCs. Finite-difference time-domain (FDTD) simulations show multiple plasmonic resonances at emissions and absorption UCNC wavelengths, which justify the experimental results. These results could pave the way for understanding the interaction of light and UCNC at very subwavelength scales and can find the applications of UCNCs in photovoltaics, single-photon sources, and bio-imaging.

Single-photon sources are emission sources that can emit a single photon as demanded. One way to achieve a single-photon source at telecommunication wavelengths at 1550 nm is by using a single lanthanide ion inside a cavity with a huge emission enhancement factor. In the second project, using the already designed plasmonic resonator in the first project, the upconversion emission of very low erbium (Er) concentration is investigated. Results show discrete levels of emissions depending on the number of Er inside the UCNC. These results would be a great way to design a single-photon source working at 1550 nm wavelength using Er. Because it can solve two major problems of previous works in this field; First, increasing the low emission rate of Er and second, solving random distribution of ion emitters inside the cavity by trapping and isolating a particle contains a single Er emitter.

In the third project, the different upconverted lights from samples with gold nanoparticles on mono dielectric layers on top of the gold samples are investigated. Under 1550 nm pulsed laser illumination, we observe second and third harmonic generations, two-photon photoluminescence, and bright broadband upconverted emission, which we believe is due to light-induced inelastic tunneling emission. In the last project, we show dual-wavelength (1210 nm and 1520 nm) excitation upconversion with plasmonic enhancement, which can increase the efficiency of solar cells by upconverting

near-infrared wavelengths to shorter wavelengths.

Table of Contents

2 Methods and Review 8

3 Contribution 32

List of Figures

Acknowledgements

"Pour a jug of wine, since you'll never know if this is your last breath or not!"

Omar Khayam, Persian mathematician, astronomer, and poet (1048-1131)

I would like to express my deepest gratitude to **my supervisor, Professor Reuven Gordon,** for all invaluable contentious guidance and support throughout my program of study.

I gratefully acknowledge the critical contributions by my collaborators throughout my study: **Professor C. J. M. van Veggel, Professor Stephen Hughes, Adriaan L. Frencken, Eradzh Rakhmatov, Dr. Ali Khademi and Dr. Mohsen Kamandar Dezfouli**.

I would like to thank all the members of the Nanoplasmonics Research Lab specially **Adarsh Lalitha Ravindranath, Ryan Peck, Jeffrey Mark Burkhartsmeyer, and Dr. Yan Wang** for their great help and supports.

My gratitude also goes out **the CAMTEC faculty and staff** for their support.

Finally and most importantly, I would like to thank **my family** for their unconditional love, support, and encouragement to continue my studies even in difficult moments of my life.

Dedication

To my family

Glossary

Common Abbreviations

Abbreviation	Meaning
APD	avalanche photodiode
CCD	charge-coupled device
CW	continuous wave
DAQ	data acquisition
DM	dichroic mirror
EM	electromagnetic
FDTD	finite-difference time-domain
FIB	focused ion beam
HWP	half-wave plate
IR	infrared
LP	linear polarizer
LSP	localized surface plasmon
NA	numerical aperture
NP	nanoparticle
LITE	light-induced inelastic tunneling emission
LPF	long pass filter
PML	perfectly matched layer
SAM	self assembled mono layer
SEM	scanning electron microscope
SHG	second harmonic generation
SPF	short pass filter
SPP	surface plasmon polariton
TE	transverse electric field
TFSF	total-field scattered-field
THG	third harmonic generation
TM	transverse magnetic field
TPPL	two photon photoluminescence
UCNC	upconversion nanocrystal

Glossary

Symbols

Symbol	Meaning
α	polarizability
β	propagation constant
ϵ	permittivity
ϵ_0	vacuum permittivity
$\epsilon(\omega)$	frequency dependent permittivity of metal
ω	angular frequency
ω_p	plasma frequency
λ	wavelength
τ	electron relaxation time
c	light speed in vacuum
E	electric field strength
H	magnetic field strength
F_{grad}	gradient force
F_{scat}	scattering force
I	light intensity
k	wavenumber
n	refractive index
L	electric field enhancement factor
p	dipole moment
P	polarization vector
P_{lum}	luminescence power
T	optical transmission
U	potential energy

Chapter 1

Introduction

The main goal of this dissertation is to investigate the interaction of light with metallic nanostructures, and lanthanide-doped upconversion nanocrystals. The motivations behind this dissertation, the reasons researchers are interested in plasmonics, and why UCNCs are useful are presented in this chapter. The organization of this dissertation is detailed here in section 1.2. This dissertation can be divided into four projects. The contribution of all the authors in each project is listed in the last section of this chapter.

1.1 Motivation

Electromagnetic (EM) waves play a key role in almost every modern device. EM waves are synchronized oscillations of electric and magnetic fields (classical physics) or quanta packages of energy called photons (quantum physics). Based on the energy of a photon, electromagnetic waves are classified into radio (very low energy), microwave, infrared (IR), visible, ultraviolet, X-ray, and gamma-ray (very high energy). Each class of this broadband spectrum has various applications including medical purposes, military weapons, communications, detecting, and energy conversion.

Human eyes are sensitive to EM waves with wavelengths from around 400 to 700 nm (visible light) with the highest sensitivity for green light (approximately 500 nm). This order of EM wavelengths is interesting since the main source power energy of the earth (Sun) has the highest spectrum power in these wavelengths. Due to evolution mechanisms, almost every single living cell in the earth operates or interacts in these wavelengths (some animals use near IR wavelengths which are also part of the solar spectrum) [4]. As a result, humans try to understand the interaction of light and matter in these wavelengths which let us design many devices operating in visible light including cameras, light sources, detectors, and solar cells.

Some metals like gold and silver, show interesting interactions with visible light; this phenomena is called plasmonics. In summary, conduction electrons of a metal (negative permittivity) at the interface with a dielectric (positive permittivity) can oscillate due to the interaction with visible light. The oscillations of a metal's free electrons can be coupled to incident electromagnetic fields and cause surface electromagnetic waves propagating on the interface of a metal and dielectric layers (evanescently confined in the normal direction of the interface). These propagating surface electromagnetic waves are called propagating surface plasmon polaritons. Also, conductive electrons of a subwavelength metallic nanoparticle can couple to electromagnetic excitation fields and cause non-propagating localized surface plasmons. Couplings of the incident electromagnetic field at the interface of negative and positive permittivity materials confine the light on the order or smaller than the light's wavelength. Depending on metal and dielectric permittivities, interfaces, temperature, shape, and size, plasmonic oscillation frequencies can change. For example, spherical gold nanoparticles with 20, 50 and 100 nm diameters show plasmonic resonances at 524, 535, and 572 nm while increasing the gold nanoparticle's diameter causes widening of the plasmonic absorption peak.

Developments in the fabrication processes help researchers to design and fabricate nonstructural metals to obtain desired plasmonic wavelengths for different applications including spectroscopy [5, 6], sensing [7, 8], solar cells [9] and single-photon sources[10].

The other interesting interaction of light and matter can be seen in optical tweezers, introduced by Arthur Ashkin [11]. Optical tweezers trap and manipulate small objects by using the momentum of photons. Plasmonics could be very helpful here since it can confine the EM waves and increase the optical trapping probability.

Lanthanides are interesting materials since they are non-blinking stable emitters. Lanthanides can upconvert the IR wavelengths to the visible light. The upconversion efficiency of lanthanides is generally higher than other upconversion mechanisms like harmonic generation. Although the upconversion efficiency is usually higher than other non-linear optical processes, it's not great enough for practical applications. Plasmonics can be useful here by increasing the interaction of light and lanthanide electrons, which can increase the upconversion efficiency. This can ease the use of lanthanide in applications like bio-imaging [12, 13], solar cells [14, 12] and single-photon sources [15, 16].

In this dissertation, the goal is to trap a single lanthanide-doped upconversion nanocrystal to study the interaction of UCNCs and plasmonic structures and the ways that the upconversion emission can be increased for applications like single-photon sources and solar cells.

1.2 Organization of the Dissertation

The dissertation is written based on four manuscripts that have either been published or submitted to peer-reviewed journals. Below, the contribution of all authors is listed. In the second chapter, the theory of plasmonics, UCNCs, and optical tweezer are presented. In chapter three, a summary of each manuscript is presented. The complete manuscripts are added to the appendix section (A-D). Summary, conclusion, and possible future works are presented in chapter four.

1.3 Major Contributions

1.3.1 Cascaded Plasmon-Enhanced Emission from a Single Upconverting Nanocrystal [1]

A. Alizadehkhaledi performed the fabrication of the samples, trapping experiments, and simulations. A.L.F. and F.C.J.M.v.V. were responsible for nanocrystal synthesis and characterization. M.K.D. and S.H. provided a theory to interpret the experimental findings. R.G. conceived the experiment. All authors assisted in writing the manuscript.

1.3.2 Isolating Nanocrystals with an Individual Erbium Emitter: A Route to a Stable Single-Photon Source at 1550 nm wavelength [2]

A. Alizadehkhaledi performed the fabrication of the samples, and trapping experiments. A.L.F. and F.C.J.M.v.V. were responsible for nanocrystal synthesis and characterization. R.G. conceived the experiment. All authors assisted in writing the manuscript.

1.4 Minor Contributions

1.4.1 Bright Upconverted Emission from Light-Induced Inelastic Tunneling

A. Alizadehkhaledi contributed to this work by assisting in preparing the samples, measurements, and simulation. E.R. prepared and measured the samples and performed the simulation. G.H. assisted in the measurements. R.G. conceived the experiment. All authors contributed to writing the manuscript.

1.4.2 Harvesting Dual-Wavelength Excitation with Plasmon-Enhanced Emission from Upconverting Nanoparticles [3]

A. Alizadehkhaledi contributed to this work by assisting in upconversion measurements. M.S.S. prepared and measured the samples. A.K. assisted in the measurements. A.L.F. synthesized and characterized the nanoparticles under the supervision of F.v.V. R.G. supervised the project, providing ideas and facilities, and performed the simulations. All authors contributed to writing the manuscript.

Chapter 2

Methods and Review

The main goal of this project was to enhance UCNCs using plasmonic resonators for both emission and absorption processes by tailoring the local electric field. To do so, understanding three different branches of science is necessary. In this chapter, at first, a brief review of plasmonics and its applications are presented. Then, lanthanide-doped nanocrystals and the upconversion mechanisms are introduced. Optical tweezers as a method of studying and manipulating tiny particles is later discussed. Metallic sub-wavelength apertures are discussed as a tool for enhancing optical trapping. Optical nonlinearity, and harmonic generation of the gold are presented. In the last section, a brief review of the finite-difference time-domain method (FDTD) which yields approximate solutions for Maxwell's equations is presented.

2.1 Plasmonics

Visible light can be concentrated to nanometer dimensions smaller than its wavelength. This happens from an interesting phenomenon arising from the interaction of light and metal and is referred to broadly as plasmonics [17]. Concentrating light to smaller dimensions compared to its wavelength resulting in the increased local electric field has found many applications from solar energy conversion to sensing and detection methods [18, 19]. Both photon absorption and emission processes are dependant on the local electric field intensity. Using a plasmonic structure with resonant frequencies at desired wavelengths can enhance both absorption and emission processes. The increment of luminescence near a plasmonic resonator can scale as [17]:

$$P_{lum} \propto L(\lambda_{ext})^2 \times L(\lambda_{em})^2, \tag{2.1}$$

where λ_{ext} and λ_{em} are excitation and emission wavelength. L represents the enhancement of the electric field due to the plasmonic resonator. One of the practical applications for plasmonics is enhancing Raman scattering. In Raman scattering, molecules absorb the incident photon and re-emit with lower or higher energy. The difference in energy can be used as a fingerprint for these molecules. As it is shown in equation 2.1 both photon absorption and emission processes are dependants on the local electric field intensity. Since the absorption and emission frequency in Raman are close to each other, a plasmonic resonator can cover both of them and as a result, enhance the Raman scattering significantly. This helps researchers to achieve Raman scattering with single-molecule sensitivity [5, 6].

One can conclude that, generally, any multi-photon processes can benefit from plasmonics. Many multi-photon processes require different wavelengths and subsequently different plasmonic resonances [20]. Plasmonic resonances are generally quite broadband, but still may not be enough to cover all desired wavelengths. Consequently, the aim is to design a plasmonic structure that can cover different wavelengths involved in multi-photon processes [21].

2.1.1 Metals: Drude Model

For understanding the plasmonic effect, let's begin with the Drude model for the metals. Free electrons in the metal can be considered as a plasma gas where electrons are moving against fixed positive ions. In the presence of EM fields, electrons oscillate as a response to EM fields, and these oscillations are damped via collisions occurring with the free electrons' relaxation time τ. The equation of moving electrons in the presence of an applied electric field (E) can be written as;

$$mx^{''} + \frac{m}{\tau}x^{'} = -eE \tag{2.2}$$

where $x^{''}$,$x^{'}$ are second and first derivative of x (electron position), e and m are the electron charge and mass. Assuming a harmonic electric field ($E(t) = E_0e^{-i\omega t}$), then the electron position, $x(t)$, can be written as;

$$x(t) = \frac{e}{m(\omega^2 + i\frac{\omega}{\tau})}E(t) \tag{2.3}$$

where ω is the electric field oscillation frequency. Considering microscopic polarization $P = -nex$, where n is the number of electrons, P can be derived from equation 2.3 as;

$$P = -\frac{ne^2}{m(\omega^2 + i\frac{w}{\tau})}E \tag{2.4}$$

In general, the polarization magnitude is defined as;

$$P = \chi\epsilon_0 E \tag{2.5}$$

where the electric susceptibility (χ) is $\chi = \epsilon_r - 1$ and ϵ_r is the relative permittivity. The real ($\epsilon_1(\omega)$) and imaginary ($\epsilon_2(\omega)$) parts of ϵ can be derived as;

$$\epsilon_1(\omega) = 1 - \frac{\omega_p^2 \tau^2}{1 + \omega^2 \tau^2} \tag{2.6}$$

$$\epsilon_2(\omega) = \frac{\omega_p^2 \tau}{\omega(1 + \omega^2 \tau^2)} \tag{2.7}$$

where $\omega_p^2 = \frac{ne^2}{\epsilon_0 m}$ is the plasma frequency of free electrons in the metal. Two different regimes for $\omega < \omega_p$ can be observed. First, if ω is large and close to ω_p and $\omega\tau >> 1$; this makes the imaginary part of ϵ negligible (the inter-band transitions in metals change the imaginary part in this regime, and it's not negligible). Second, if the frequency is small, the imaginary part becomes a large value, and metals are behaving as significant absorbing materials. In these two regimes, the real part of ϵ is negative. If $\omega > \omega_p$ the electrons in metals can not follow the oscillations of the electric field and metals become transparent for large frequencies (usually in ultraviolet frequencies or even more).

2.1.2 Surface Plasmon Polaritons

Let's now consider a system with metal (negative ϵ) and a dielectric (positive ϵ) under the illumination of EM fields (2.1). To understand the physics of this system, we need

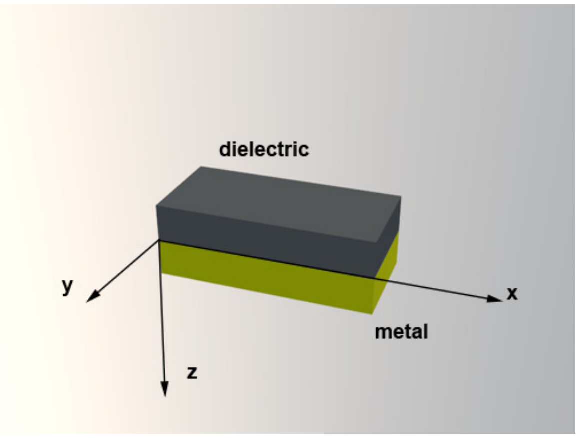

Figure 2.1: Surface plasmon propagation at the interface of a dielectric and metal.

to solve Maxwell's equations. After some assumptions, we can derive the equation below (Helmholtz's wave equation);

$$\nabla^2 E + k_0^2 \epsilon E = 0 \tag{2.8}$$

where $k_0 = \frac{\omega}{c}$ is the magnitude of wave vector in the vacuum. By solving this equation for two different mediums and applying boundary conditions, we can get two sets of answers, depend on the electric field polarization. Transverse magnetic field (TM) where there is no magnetic field component in the propagation direction (z) and transverse electric field (TE) where there is no electric field component in the propagation direction (z). Solving the equations for these conditions shows interface wave propagation (x) for TM mode and no propagation for TE mode. The complete set of equations can be found elsewhere [17].

The TM solutions show an evanescent decay electric field component ($\propto e^{-k_2 z}$)

perpendicular to the interface (z), and a propagation wave at the interface (x). The dispersion relation of the wave propagating at the interface can be found;

$$\beta = k_0\sqrt{\frac{\epsilon_m \epsilon_d}{\epsilon_m + \epsilon_d}} \tag{2.9}$$

where β is propagation constant, k_0 is the magnitude of free space wave vector, and ϵ_m and ϵ_d are the permittivities of metal and dielectric. It can be seen that if ϵ_m approaches $-\epsilon_d$, then β , the propagation constant, becomes very large and as a result, the wavelength becomes very small at the interface. Consequently, the electric field is confined to the surface and decays exponentially perpendicularly to the surface (z). These phenomena are called surface plasmon polaritons where the electric fields are confined and propagate at the surface of two materials with negative and positive epsilon.

2.1.3 Localized Surface Plasmons

The other fundamental plasmonic effect are localized surface plasmons where non-propagating excitations of the conduction electrons of a metallic nanostructure are coupled to the electromagnetic field. This happens when an oscillating electric field is applied to a subwavelength metallic nanoparticle. Let's consider a small nanoparticle

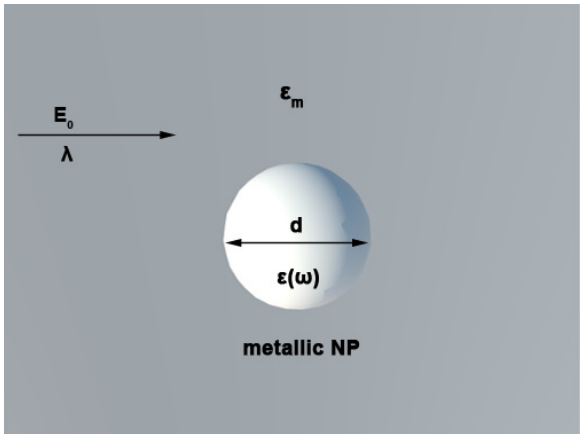

Figure 2.2: Localized surface plasmon. Spherical nanoparticle with permittivity $\epsilon(\omega)$ inside a dielectric medium with permittivity ϵ_m under the illumination of an electric field E_0.

with diameter (d), under the illumination of an EM field with wavelength λ where $d << \lambda$. In this case, the phase of the harmonically oscillating EM field is constant over the volume of the particle. As a result, we can solve a quasi-static approximation of the Laplace equation ($\nabla^2\phi = 0$) where the electric field is applied to a tiny particle. The electric field inside (E_{in}) and outside (E_{out}) of the particle can be found by getting a gradient from the potential (ϕ);

$$E_{in} = \frac{3\epsilon_m}{\epsilon(\omega) + 2\epsilon_m} E_0 \tag{2.10}$$

$$E_{out} = E_0 + \frac{3n(n.p) - p}{4\pi\epsilon_0\epsilon_m r^3} \tag{2.11}$$

where p is the electric dipole moment ($p = \epsilon_0\epsilon_m\alpha E_0$) under illumination of E_0, $\epsilon(\omega)$ and ϵ_m are metal nanoparticle and medium permittivities. As we can see in the equations, the electric fields experience the resonance when $\mid \epsilon(w) + \epsilon_m \mid$ becomes minimum. Under this condition, the electric field inside a particle increases for the resonance frequency. This enhancement and confinement of the electric field inside a nanoparticle is called a localized surface plasmon.

2.2 Lanthanide-Doped Upconversion Nanocrystals

Lanthanide-doped upconversion is a multi-photon process that can benefit from plasmonics [22, 23]. Lanthanide-doped nanoparticles are made from a transparent host material usually $NaYF_4$, $NaGdF_4$, $LiYF_4$, YF_3 or CaF_2 which is doped with lanthanide ions such as Er^{3+},Yb^{3+},Tm^{3+} or Yb^{3+} [24].

One of the popular combinations is Yb^{3+} and Er^{3+}. Figure 2.3 displays energy-transfer upconversion diagram for the Yb^{3+} and Er^{3+} codoped upconversion materials. First, Yb^{3+} acts as an antenna by absorbing the incident 980 nm wavelength and then transferring the energy to an Er^{3+}. This allows the Er^{3+} to emit either green (550 nm) or red (650 nm). As we see for 550 nm emission, two 980 nm photons are absorbed, and a 550 nm photon is emitted, which makes this upconversion process a three-photon process which has a great potential for improved plasmonic enhancement[25]. Based on equation 2.1, the enhancement of emission at 550 nm and 650 nm can scale as

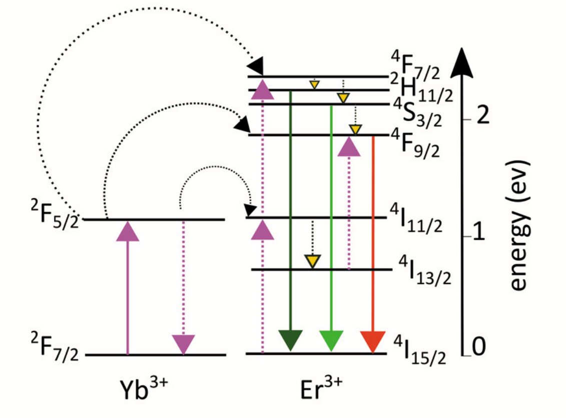

Figure 2.3: Energy transitions schematic of upconversion mechanism for the Er^{3+}, Yb^{3+}. Upconversion absorption (solid purple arrow), energy transfer (dashed purple arrows), nonradiative relaxation (dotted yellow arrows), and 520 nm, 550 nm, 650 nm emissions (dark green, light green and red arrows) are illustrated.

$$P_{lum@550} \propto L(980\ nm)^4 \times L(550\ nm)^2, \tag{2.12}$$

$$P_{lum@650} \propto L(980\ nm)^4 \times L(650\ nm)^2, \tag{2.13}$$

where L(980 nm), L(550 nm) and L(650 nm) are the increment of the electric fields at 980 nm, 550 nm and 650 nm due to plasmonic resonances. It is worth mentioning that even though plasmonics can increase the absorption by increasing the local electric fields and increase the emission by increasing the radiative decay rate, it can also hinder the upconversion process by increasing the non-radiative decay rate [23]. This mainly happens due to energy transfer between the plasmonics structure and

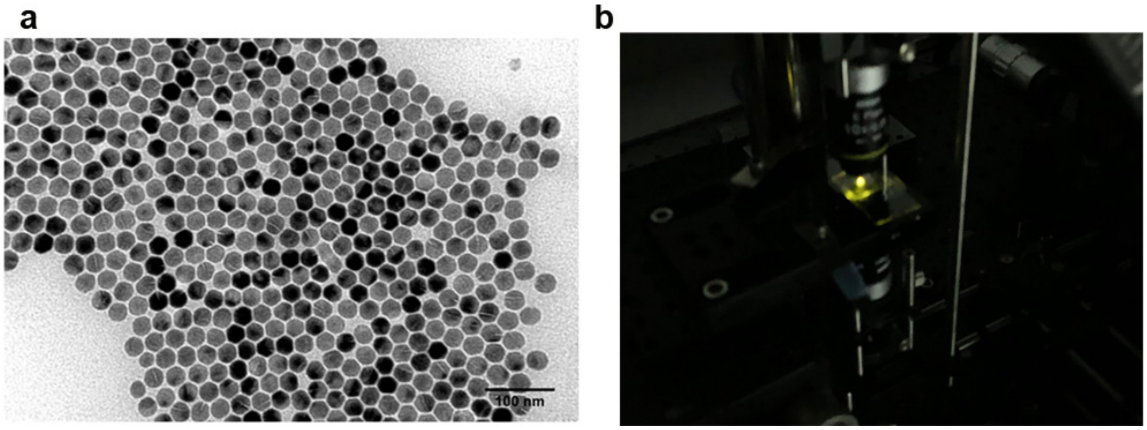

Figure 2.4: Upconversion nanocrystals. **(a)**, TEM image of hexagonal $NaYF_4$ UCNCs codoped with Er and Yb. **(b)**, UCNCs solved in hexane under illumination of the 980 nm laser.

photoluminescence molecule at the nanoscale distance [26].

Figure 2.4 (a) shows the transmission electron microscopy (TEM) image of synthesized UCNCs with Er (2%) and Yb (18%) codoped in the host $NaYF_4$ nanocrystals. The UCNCs are hexagonal with a diameter of about 25 nm. Figure 2.4 (b) shows the upconversion emission of $8\mu L$ of these UCNCs dissolved in hexane (14 mg/mL) under the illumination of a continuous wave (CW) 980 nm laser. Under high illumination power with high concentration, the yellow upconversion emissions (mixed of green and red) can be seen with the naked eyes.

Although upconversion nanocrystals are stable materials, they suffer from weak conversion efficiency which limits their applications in improving solar energy harvesting [14, 12], photocatalysis [27], single photon sources [15, 16] and bio-imaging [28, 12, 13].

2.3 Optical Tweezers

Arthur Ashkin won the 2018 Nobel Prize in Physics for the invention of the optical trapping, and its' application in biological systems [29]. Optical tweezers make use of a highly focused electromagnetic wave incident on a particle to trap, hold, and manipulate it [30]. Ray optics can easily explain trapping of a particle in the Mie regime (where the particle's size is larger than the incident wavelength). Figure 2.5 shows a Gaussian incident beam on a particle. Arrows (a) and (b) represent two rays, where (b) has a higher intensity than (a) since it's closer to the middle of the Gaussian beam. Using the conservation of momentum, F_a and F_b can be drawn and separated into two components, which are generally referred to as scattering and gradient forces. Since the gradient component for ray (b) is greater than (a), the particle moves toward the center of the Gaussian beam where the gradient forces are symmetric and cause stable trapping of the particle in the middle of Gaussian beam. If the particle moves out of the trapping site, the gradient force moves it back to the center of the Gaussian beam.

In the Rayleigh regime (where the diameter of particle is much smaller than the incident wavelength), the scattering and gradient forces can be derived considering

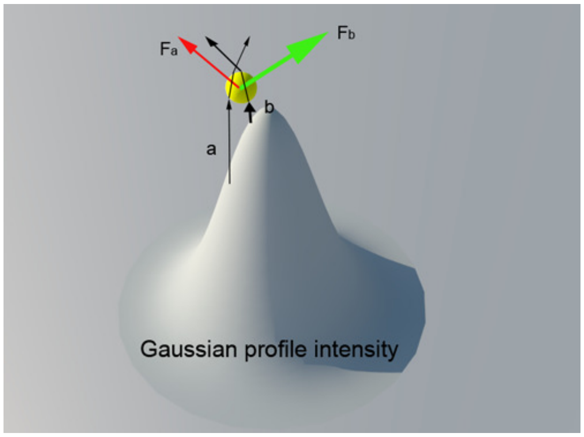

Figure 2.5: Incident EM with Gaussian profile over a particle. F_a and F_b are two force vectors in the result of incident optic rays a and b. Since $F_a > F_b$ the particle moves to the right (center of the Gaussian beam).

the particle as a point dipole interacting with the incident beam [31];

$$F_{scat} = \frac{I_0}{c}\frac{128\pi^2(\frac{d}{2})^6}{3\lambda^4}(\frac{n_p^2 - n_m^2}{n_p^2 + 2n_m^2})^2\ n_m, \tag{2.14}$$

$$F_{grad} = \frac{1}{2}n_m\alpha\nabla|E|^2 = \frac{n_m^3(\frac{d}{2})^3}{2}(\frac{n_p^2 - n_m^2}{n_p^2 + 2n_m^2})^2\nabla|E|^2 \tag{2.15}$$

where I_0 and λ are the beam intensity and wavelength. c and d are the speed of light and diameter of the particle. n_m and n_p are the refractive indexes of the surrounding medium and particle. α and E show the polarizability of the particle and the electric field. Equation 2.15 shows that the gradient force scales with the diameter of the particle, gradient of the electric field, difference and absolute value of the particle and medium refractive indexes. One can conclude that the feasibility of trapping usually becomes smaller for smaller particles since for example the polarizability of an object is proportional to the volume. As a result, for trapping small objects a large electric field is required [32]. This can also be shown by the potential energy of trapping (U) which can be derived by integrating of the trapping force; Equation 2.15 [31];

$$U = -\frac{2\pi n_m(\frac{d}{2})^3}{c}(\frac{n_p^2 - n_m^2}{n_p^2 + 2n_m^2})I \tag{2.16}$$

where, I is the intensity of beam at trapping point and can be written as;

$$I = \frac{1}{2}\epsilon_0 cE^2 \tag{2.17}$$

Equation 2.16 shows the dependence of potential energy to the third power of particle size and the second power of the electric field. For trapping of a particle, this potential energy should overcome the Brownian motion of the particle in the trapping medium. The thermal kinetic energy of the particles arising from Brownian motion is k_BT, where k_B is Boltzmann's constant and T is temperature. Here again, plasmonics could help trap tiny particles since it can enhance the local electric fields.

Nanoapertures in metal films would be a great way of using plasmonics for trapping objects [33]. Moreover, metal films have a high thermal conductivity, which is a vital point for trapping fragile tiny particles since we need a high electric field for trapping them, which can change the local temperature significantly[32]. The high temperature at the trapping site increases the Brownian motion, which demands more potential energy and more electric field. Moreover, this high temperature damages fragile biological particles like proteins and DNA.

Figure 2.6 shows the modified Thorlabs optical trapping setup used in this dissertation. A CW 980 nm single-beam laser was collimated and linearly polarized in the desired direction using a linear polarizer (LP) and a half-wave plate (HWP). Then, the beam area was expanded to nearly three times greater using two lenses. A white LED was used as a light source of optical microscopy to shine the sample and finding a subwavelength aperture through a charged-coupled device (CCD) camera. Two short pass dichroic mirrors (D1 and D2, 805 nm Thorlabs) were used to separate the path of 980 nm laser and LED light. The 980 nm laser beam was focused on

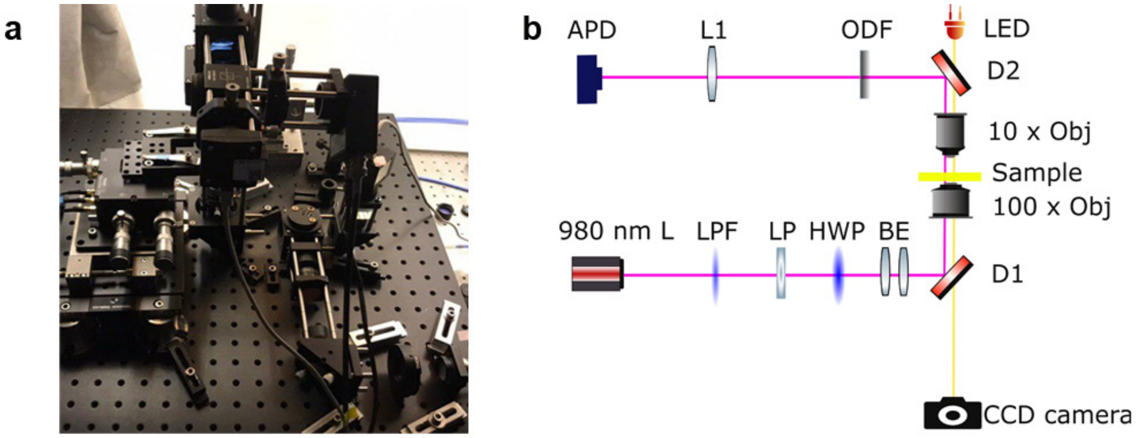

Figure 2.6: Optical trapping. **(a)**, Thorlabs optical trapping setup. **(b)**, schematic of optical trapping setup. Abbreviations used: CCD camera = charge-coupled device camera, LP = linear polarizer, L = lens, D = dichroic mirror, HWP = half-wave plate, BE = beam expander, 980 nm L = 980 nm laser, Obj = objective lens, ODF = optical density filter and APD = avalanche photo-detector.

the sample using a 100× oil immersion microscope objective (1.25 numerical aperture). A 10× condenser microscopic objective (0.25 numerical aperture) was used to collect the transmitted signal through the rectangle aperture and was measured by a silicon-based avalanche photodetector (Thorlabs APD110A). A piezoelectric controlled 3-axis sample stage was used to align the beam through the apertures with 20 nm positioning precision.

2.4 Sub-Wavelength Apertures

Many nanoaperture designs (double nanohole, circular, rectangular, bow-tie) have been used for trapping and manipulating small particles like proteins and DNA [34, 33, 35, 36, 37].

Rectangular apertures are interesting designs since they demonstrate stronger polarization dependence, higher transmittance, and supporting transmission resonances [38] comparing to circular and square apertures. Also, rectangular apertures help provide multiple plasmonic resonances due to the difference in the length of the axes. This can be very helpful for designing a plasmonic structure for multi-photon processes with different wavelengths.

Bethe calculated the transmission of a subwavelength circular hole aperture inside an infinitely thin, perfect conductor film [39]. The subwavelength aperture can be modeled as a small magnetic dipole assuming the light intensity (I) is constant over the aperture for normal incidence. The transmission coefficient is then given by;

$$T = \frac{64}{27\pi^2}(kr)^4 \propto (\frac{r}{\lambda_0})^4 \tag{2.18}$$

Equation 2.18 shows that the transmission for sub-wavelength aperture is very small and scales as $(\frac{r}{\lambda_0})^4$. If the incident light excites the localized surface plasmon at the subwavelength aperture, then the transmission (T) is changing because of three important consequences;

- It increases the fundamental cut-off wavelength (λ_{max}) of the waveguide [40].
- Surface plasmon propagating modes can exist and assist the transmission even for the frequencies lower than the plasma frequency [41].
- The dimension and geometry of the sub-wavelength aperture can change the position and bandwidth of surface plasmon modes and as a result the transmission through the aperture [17].

Figure 2.7 shows the samples of fabricated rectangular (a) and double nanohole (b) apertures using focused ion beam (Hitachi FB-2100 FIB).

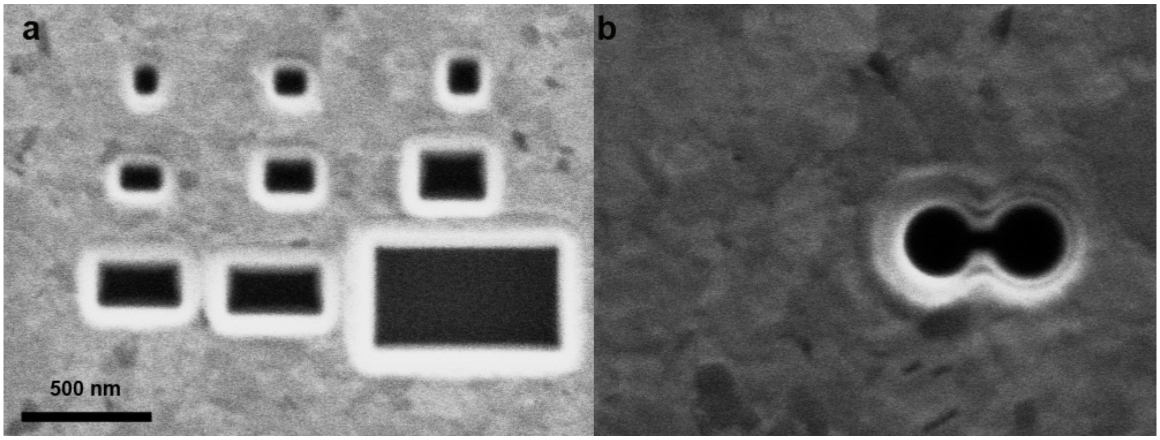

Figure 2.7: Focused ion beam image of fabricated rectangular **(a)** and double nanohole **(b)** apertures

2.5 Nonlinear Optics

We saw that the polarization vector linearly depends on the electric field, however, by increasing the electric field, the polarization eventually becomes saturated, and this saturation can be modelled by nonlinear susceptibility;

$$P = \epsilon_0 \chi^{(1)} E + \epsilon_0 \chi^{(2)} E^2 + \epsilon_0 \chi^{(3)} E^3 + ... \tag{2.19}$$

where χ^n is nth-order nonlinear susceptibility, E is the electric field, and ϵ_0 is the vacuum permittivity. Nonlinear optics can be used to produce upconverted light with twice (second harmonic) [42, 43]), and three times (third harmonic [44, 45]) the incident EM's frequency. The nonlinear behavior occurs whenever the electric field is comparable to the binding energy between the electron and atom ($\sim 10^{10}$- 10^{11} V/m). Any materials can show nonlinear behavior; however, a huge electric field is usually required. The nonlinear behavior can be achieved by a much smaller electric field using the phase matching condition [46]. Gold has inversion symmetry, which causes the even orders of χ^n to become zero, and consequently, there is no even harmonic generation. However, any broken symmetry in the gold structure like the gold surfaces can produce even orders of harmonic generation.

2.6 FDTD Method

The finite difference time domain (FDTD) method is a numerical method to find approximate solutions for two Maxwells' curl equations (Faraday's and Ampere's laws). In this method, the computational space is discretized using Yee's scheme (rectangular grid considering uniform electric fields at edges and magnetic fields at the surfaces of a grid) [47]. In addition, it uses the leapfrog method by sampling the electric fields at times $n\Delta t$ and magnetic fields at times $(n+\frac{1}{2})\Delta t$. The two Maxwells' curl equations (Faraday's and Ampere's laws) can be written as;

$$\nabla \times E = -\mu \frac{\partial H}{\partial t} \tag{2.20}$$

$$\nabla \times H = -\epsilon \frac{\partial E}{\partial t} + \sigma E \tag{2.21}$$

where E and H are electric and magnetic fields. μ and ϵ are permeability and permittivity. t and σ are time and electric conductivity. These two equations show that changing of the magnetic fields in time generates the electric fields and vice versa. Using finite-difference approximations, equations 2.20 and 2.21 can be written as;

$$\frac{H(t+\frac{\Delta t}{2}) - H(t-\frac{\Delta t}{2})}{\Delta t} = -\frac{1}{\mu}\nabla \times E(t) \tag{2.22}$$

$$\frac{E(t+\Delta t)-E(t)}{\Delta t}=\frac{1}{\epsilon}\nabla\times H(t+\frac{\Delta t}{2}) \tag{2.23}$$

Electric fields for a specific time step are calculated and stored in memory based on the previously calculated magnetic fields. Then, the magnetic fields are calculated and stored in memory based on previously calculated electric fields and so on. Using a single time-domain simulation (for example a pulse signal) can cover a wide range of frequency responses of the system.

Two important parameters in FDTD simulations are the grid size and time step (Δt). The grid size should be much smaller than the smallest wavelength, especially for plasmonic studies (since propagation constant becomes very large and reversely wavelength becomes very small). The other factor for choosing the grid size is the geometry of the structure. The grid size should be smaller than geometrical features of the structure which can result in a very long time for FDTD simulations for the rough surfaces.

When the electromagnetic field is moving across a discrete spatial grid in discrete time steps, the time steps should be smaller than the time it takes for the wave to go across a spatial grid. This leads to the Courant-Friedrichs-Lewy stability condition as it is written bellow [48];

$$\Delta t\leq(c\sqrt{\frac{1}{\Delta x^2+\Delta y^2+\Delta z^2}})^{-1} \tag{2.24}$$

where c is the largest EM wave propagation velocity in the problem, and Δx, Δy and Δz are spatial grid sizes.

The other important factor in FDTD simulation is the boundary condition which truncates the simulation area. The usual boundaries are Perfectly Matched Layer (PML), Perfect Electric Conductor (PEC), Perfect Magnetic Conductor (PMC) and Periodic Boundary Condition (PBC). PML boundaries absorbs all EM waves incident on them (reflection-less). PEC and PMC are perfectly reflecting boundaries for electric and magnetic fields. PBC boundaries are used when both the structures and EM fields are periodic. The boundary condition in this dissertation is PML since we have open boundaries in experiments and PML absorb all EM and does not reflect EM waves to simulation area (ideally).

The Lumerical FDTD simulation is used for different projects in this dissertation. Figure 2.8 shows a sample of FDTD simulation of rectangular aperture (100 $y\times$ 200 nm (x)) inside a gold film with 100 nm thickness (z). The surrounding mediums are hexane (on top and inside the hole) and glass (bottom). A total-field scatter-field (TFSF) is used to illuminate the sample with 980 nm wavelength linearly polarized along the short axis y of the aperture. Figure 2.8 (a) shows the profile of the electric field at the surface of aperture $x-y$, and (b) shows the profile of the electric field at a cross-section view $y-z$. The electric field shows higher intensities along the long axis at the edges of the rectangular aperture where the trapping is happening. More information can be found in the simulation method of each paper (Appendix A-D).

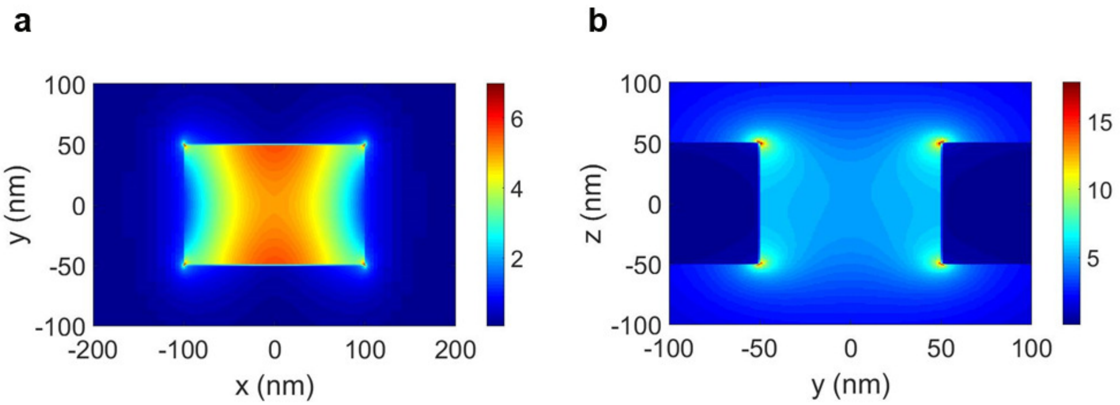

Figure 2.8: FDTD simulation of a rectangular aperture inside a gold film. **(a)**, electric field profile at the surface of the aperture$x - y$. **(b)**, electric field profile at the cross section of the aperture $y - z$.

Chapter 3

Contribution

In this chapter, a brief review of the theories and results of the four studies is presented. In appendix A through D, all these four studies presented as manuscripts with full details. In the first section, the fabrication of multiple rectangular apertures to achieve multiple plasmonic resonances for trapping and enhancing UCNCs is presented. In section 3.2, by using the already fabricated rectangular aperture with 410× emission enhancement, the possibility of trapping and counting the number of active Er doped in an UCNC based on upconversion emission is described. In the section 3.3, the interactions of 1550 nm pulsed laser with gold nanoparticles on SAM on top of gold samples are explored. In the last section, the possibility of dual-band excitation of Er-doped UCNCs with plasmonic enhancements and the potential for solar cells enhancement is presented.

3.1 Cascaded Plasmon-Enhanced Emission from a Single Upconverting Nanocrystal (Appendix A)

The goal of this project is to enhance upconversion using plasmonics for both emission and absorption processes by tailoring the local electric field. There have been many reports using plasmonic enhancement for absorption [49, 50] and emission [51, 52] wavelengths of UCNCs. Also, using plasmonic enhancement for both excitation and emission wavelengths has been reported for aperture arrays in metals [53, 54]. There are also some other studies on plasmonic upconversion enhancement of a single upconversion nanocrystal [55, 56].

In these studies, nanorod-UCNC interactions have been explored due to the existence of multiple resonances in nanorod structures. However, using these kinds of structures would not be an accurate method to study upconversion-plasmonics interactions beacuse of; first, finding the exactly matched plasmonic resonances with UCNCs is difficult since these structures are not well tunable. Second, the distance of plasmonic resonators and UCNCs also is not that much control-able. Here, we used a rectangular aperture on gold film for trapping a single UCNC since:

- Achieving multiple resonances for both emission and absorption wavelengths of

UCNC is possible.

- These apertures are made using a focused-ion beam method, which lets us tune the apertures to an accuracy of 2 nm.
- Trapping a single UCNC lets us have a better insight into plasmonics-upconversion interaction.
- Rectangular aperture shows strong polarization dependence, which can alter the UCNCs polarization emission.

In this study, after the fabrication of different rectangular apertures using a focused ion beam (FIB), 100 nm was chosen as a fixed axis, and the other axis was tuned from 100 nm to 226 nm with 2 nm fine steps (Analysing the FIB image of the rectangular apertures using ImageJ software shows the variation of of the rectangle's width between 97 and 104 nm). Adriaan L. Frencken, under the supervision of Prof. Frank C. J. M. van Veggel, synthesized and characterized UCNCs. These UCNCs were Er-Yb co-doped in $NaYF_4$, which emit Green (550 nm) and Red (650 nm) lights by absorbing 980 nm. The synthesized UCNCs were diluted in hexane with 3×10^{10} UCNCs/ cm^3 concentration. Then, the fabricated rectangular apertures are used to trap a single UCNC by using 980 nm CW laser and the upconverted emission recorded using a fiber-coupled spectrometer at reflection side.

Results showed significant 100 × enhancements from a single UCNC inside a 100 × 212 nm aperture comparing to other apertures. Moreover, comparing emission from single UCNCs at this aperture to a free solution with approximately 30 particles at the focusing area gave us 400 × enhancement.

Figure 3.1 (a) shows a schematic of the experimental setup. A 980 nm collimated laser is focused on a rectangular gold aperture on a gold film cause trapping and exciting single UCNC. The trapped excited UCNC emits green (550 nm) and red (650 nm) lights detected by a spectrometer on the reflection side. A focused ion beam image of a test pattern of all 64 rectangular apertures is shown in the figure 3.1. Figure 3.1 (b) displays the emission enhancement for 550 and 650 nm emission for different rectangular aperture lengths comparing to free solution. The other interesting observation was the emission ratio between 650 nm and 550 nm which was increasing with both plasmonics enhancements and incident power.

To explore more the impact of aperture plasmonics resonances on the upconversion emission, emission polarization dependence measurement was carried out by adding a linear polarizer before the spectrometer which gave us interesting results that the 650 nm and 550 nm emissions were perpendicularly polarized by factor of the 0.7. The 650 nm emission followed the polarization of incident 980 nm laser.

Mohsen Kamandar Dezfouli under the supervision of Prof. Stephen Hughes performed FDTD simulation which justified the experimental results showing the existence of plasmonics resonances at 550 nm, 650 nm, and 980 nm. Results were published in ACS Photonics (see Appendix A) [1].

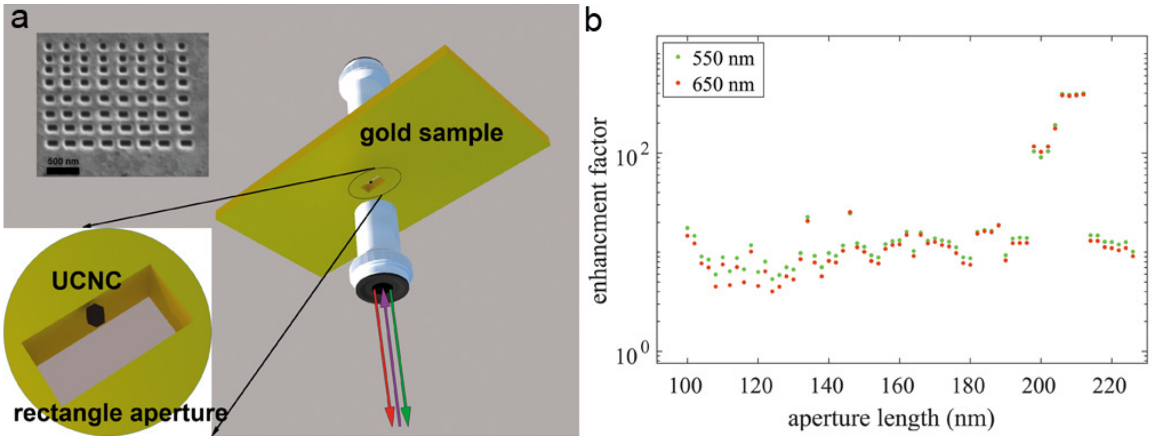

Figure 3.1: Plasmonic upconversion emission enhancement factor by tuning the aperture length. **(a)**, Schematic of a rectangular aperture in the gold film with a trapped UCNC placed at the highest electric field profile. Green, red, and purple arrows represent 550, 650, and 980 nm wavelengths. The focused ion beam image of a test pattern of the rectangular aperture is shown at the top left. The short axis of the aperture is fixed at 100 nm, and the long axis is varied from 100 to 226 nm in 2 nm steps. **(b)**, Enhancement factor for 550 and 650 nm upconversion emissions of a single trapped UCNC trapped in different rectangular apertures comparing to free solution measurement. © Reprinted, with permission, from American Chemical Society, 2019 [1]

3.2 Isolating Nanocrystals with an Individual Erbium Emitter: A Route to a Stable Single-Photon Source at 1550 nm Wavelength (Appendix B)

As it is presented in section 3.1, we designed a plasmonic cavity with approximately 400× enhancement for trapping a UCNC contained approximately 2,000 erbium ions. This experiments showed that we can detect the single Er ion emission using the plasmonic cavity with enhancement factor.

Single lanthanide emitter in a crystal matrix would be a good candidate as a single-photon source since they are non-blinking stable emission. As a result, much research has been carried out to detect single lanthanide ions (praseodymium [57, 58, 59, 60], cerium [61, 62, 63], and erbium [64, 15]).

Erbium is an interesting case since it has a transition at fiber's low loss communication band (1530 nm); however, the problem arises from the low transition probability of Er at 1530 nm due to the shielding of 4f electrons, which reduces interaction of light and 4f electrons (4f orbitals are shielded from the outside crystal by optically active 6s orbital [46, 23]). Plasmonics is a useful approach to increase the interaction of

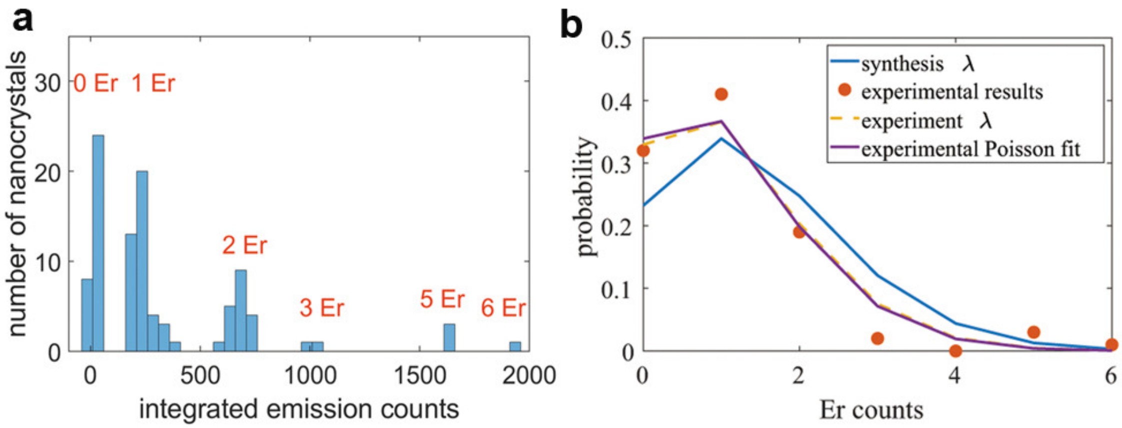

Figure 3.2: Poisson distribution of the number of active Er inside a UCNC. **(a)**, Schematic of optical trapping rectangular aperture with hexagonal UCNC placed at the highest intensity of the electric field. The hexagonal UCNC contains 0 to 3 Er ions. **(b)**, Probability of having 0 to 6 Er emitters based on upconversion emission for the experimental measurements (red dots). The dashed yellow line and blue line show the Poisson distribution using expected synthesis statistics having a mean Er count of 1.53 per particle and calculated experiment statistics with mean Er count of 1.11 per trapped particle. The purple line shows the fitting of experimental data using a Poisson distribution. The fitted mean value is 1.08 Er per UCNC.

light and 4f electrons of Er.

Another critical problem of these studies is that the distribution of emitters inside the cavity is random. To solve this problem, researchers recently reported on the ion-trap implantation method to implant as few as four ions at a single spot; however, about half of the implanted ions do not emit, which makes the emission yield 50% [65].

The plasmonics subwavelength aperture can solve both problems, low emission rate of Er and random distribution of ions' emitters. First, the plasmonic structure can be designed to enhance the Er emission at the desired wavelengths. Second, it traps and isolates the single Er UCNC, which can be translocated to desired location later [35].

To detect the emission of single Er ion, at first, we need to decrease the number of Er ions inside a UCNC. Adriaan L. Frencken under the supervision of Prof. Frank C. J. M. van Veggel synthesized three different batches of UCNCs with the mean values of 1.53, 0.07573 and 0.00609 Er per UCNC.

Figure 3.2 (a) shows a schematic of the rectangular subwavelength aperture with a UCNC trapped at the highest electric field intensity. It also indicates hexagonal UCNCs with 0-3 Er ion emitters. We used the already fabricated plasmonic cavity with 410 times enhancement for trapping single UCNC. Figure 3.2 (a) shows the probability of having 0-6 Er in the trapped UCNCs (red dots) based on the upconversion emission. It also shows the Poisson distribution of experimental data (dashed yellow line) by using the experimental result's mean value. It is clear that the experimental results follow a Poisson distribution, and it is in agreement with the Poisson distribution of synthesizing results. In addition, the experimental data are fitted using a Poisson distribution. The fitted mean value is 1.08 Er per trapped particle.

Results show discrete levels of emission from trapped UCNCs based on the number of active emitters. The experimental and synthesized mean values for this batch are 1.11 and 1.53 Er per UCNC. The mean value for the trapping experiment shows 0.73% of the synthesized value. We attribute this lower value to quenching of Er ions close to the surface which can reduce the emission by two orders of magnitudes [66, 67]. Results were published in Nano Letters [2].

3.3 Bright Upconverted Emission from Photon Induced Inelastic Tunneling (Appendix C)

Nonlinear optics in metallic nanostructures can produce upconverted lights in different processes including second harmonic generation [42, 43, 68], third harmonic generation [44, 45], two-photon photoluminescence [69, 70, 71, 72] and three-photon photoluminescence [69, 45]. These nonlinear effects are a very weak process even when using plasmonic resonators at desired wavelengths. The efficiency is usually less than a fraction of percent [73, 74, 75, 76, 77, 78], and researchers mostly use pulsed lasers to observe these effects. Since pulsed lasers can deliver a huge amount of power in a very short time (femtoseconds) when the average power of the laser is so small compared to the pulse power.

With this huge power of the pulsed laser, the electron can eject from metal surfaces [79, 80, 81, 82, 83]. Also, the metal junction under DC bias can emit light due to tunneling-induced light emission [84, 85, 86]. Recently, high efficiency of 2% with the possibility to increase the efficiency has been reported for this effect [87, 88].

In this study the emission properties of different samples using 5, 20 and 60 nm gold nanoparticles on an amino-alkane-thiol self-assembled monolayer with varying carbon length (C2 – 30070 Sigma-Aldrich, C3 – 739294, Sigma-Aldrich, C6 – 733679 Sigma-Aldrich C8 – 745774 Sigma-Aldrich) on an 30 nm thick ultra-flat gold (template stripped off silicon) under the illumination of 1550 nm femtosecond pulsed laser have been studied.

Under the 1550 nm pulsed laser illumination, second harmonic generation (SHG), third harmonic generation (THG), two-photon photoluminescence (TPPL), and a bright broadband upconverted emission are observed. This bright upconverted emission shows a cut-off wavelength, which is blue shifting by increasing of the incident pulse power; this is a signature of tunneling effects. We attribute this broadband upconverted emission to light-induced inelastic tunneling emission (LITE). The FDTD simulations show that the voltage across the junction due to the electric field of incident pulse is comparable to the voltage of an unconverted emission at cut-off wavelength. Finding the exact cutoff wavelengths of the experiments are limited by the quantum efficiency of the silicon spectrometer. Figure 3.3 (a) shows the gold nanoparticle on a thin sub-nanometer SAM layer on the gold film sample. The red and blue arrows show the incident pulsed laser and the upconverted emission. The electron inside the gold nanoparticle can tunnel through the sub-nanometer SAM dielectric (black arrow) and emit a photon. Figure 3.3 (a) shows the cut-off wavelength (blue dots) of the bright broadband upconverted emission for different incident pow-

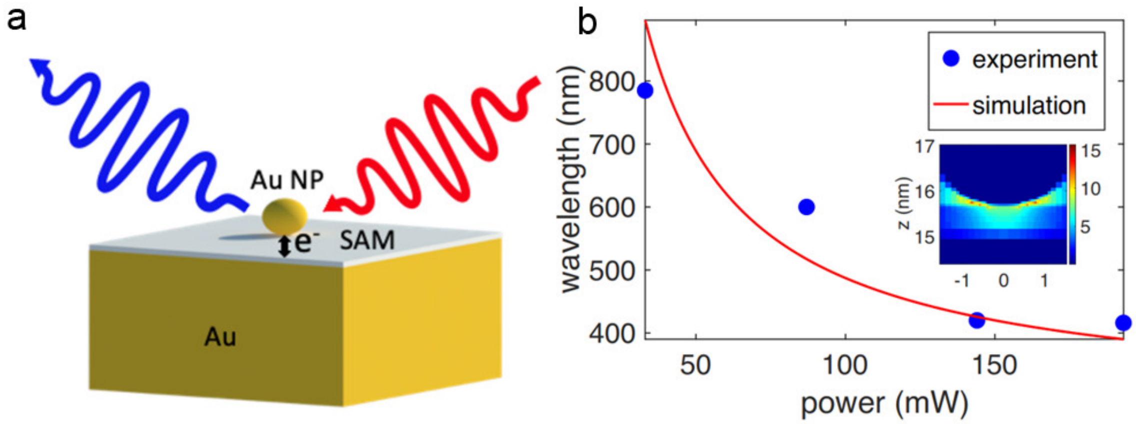

Figure 3.3: Light-induced inelastic tunneling emission. **(a)**, Schematic of the samples and incident (blue arrow) and emitted photon (red arrow). Sample contains gold nanoparticle on a SAM sub-nanometer layer on a gold film. **(b)**, The experimental and FDTD simulation cut-off wavelengths for different incident powers. The cut-off wavelength of simulation is calculated using the photon energy derived from the voltage across the junction.

ers. The red line shows the result of a simulation based on the electric field across the junction for different incident powers. As it is shown in the figure 3.3, the cut-off wavelength is blue shifting by increasing the incident power.

This LITE effect shows almost 10^5 greater magnitude comparing to SHG and THG. Besides, dark-field scattering of the samples is studied, and it shows plasmonics transverse resonance at around 550 nm, and longitudinal resonances depend on the thickness of the SAM layers.

3.4 Harvesting Dual-Wavelength Excitation with Plasmon-Enhanced Emission from Upconverting Nanoparticles (Appendix D)

Converting solar energy using photovoltaic cells is a promising way to substitute fossil fuels. Silicon-based solar cells are the dominant photovoltaic cells with above 26% efficiency [89, 90, 91]. The bandgap of silicon is 1.11 eV, which is equal to 1130 nm wavelength.

Figure 3.4 (a) shows the solar spectrum stretching from ultraviolet (300 nm) to infrared wavelength (2200 nm) with the peak of power in visible light (500 nm). Silicon is an appropriate material for solar technology because it absorbs the visible

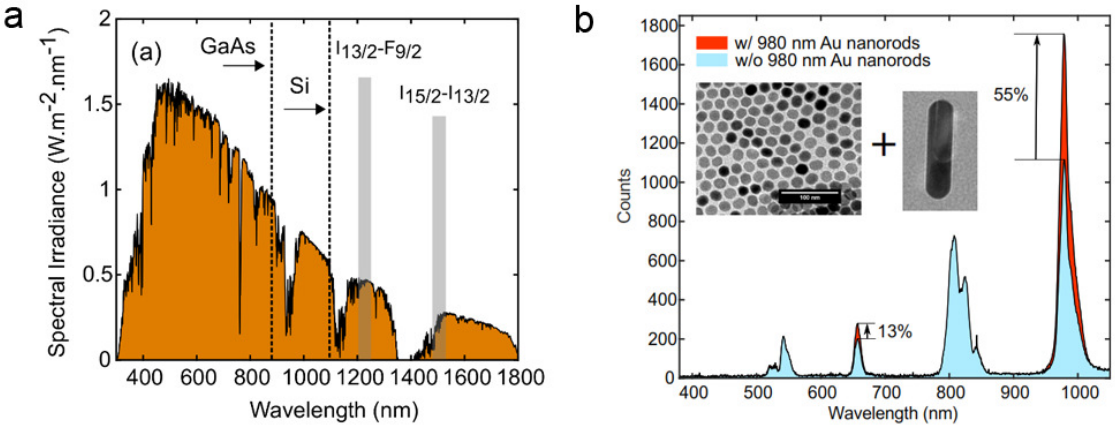

Figure 3.4: Dual wavelengths upconversion excitement. **(a)**, Solar spectrum power for different wavelengths. Gray lines show the Er transition at 1210 and 1520 nm. Silicon and Gallium Arsenide band gap cut-off wavelengths are shown by the dashed line (1130 nm, 870 nm). **(b)**, Upconversion emission of Er-doped UCNCs drop coated on gold film with (blue) and without gold nanorods (red) under the excitation of supercontinuum laser (wavelength > 1200 nm). TEM images of UCNC and gold nanorods. © Reprinted, with permission, from American Chemical Society, 2019 [3]

light. Still, since the silicon bandgap is 1.1 eV, it cannot absorb a photon with greater wavelengths than 1130 nm. As we can see in figure 3.4, there are two main peaks greater than 1130 nm (around 1200 nm and 1600 nm). By absorbing and converting these wavelengths, silicon solar efficiency can be increased further. Using lanthanides in the photovoltaic cell is a way to increase the solar cell efficiency by upconverting near IR wavelength to greater energy in the absorption spectrum of solar cell [14, 92, 93, 94, 95]. The problem arises from the low upconversion efficiency of lanthanides due to the shielding of 4f orbitals. One way to overcome this is by using a plasmonic resonator to enhance light and matter interaction.

Here, we show dual-wavelength (1210 nm and 1520 nm) excitation upconversion with plasmonic enhancement. We use Er-doped nanoparticles, which have bands at 1520, 1210, 980, 808, 650, and 550 nm wavelengths. The Er-doped UCNCs are drop-coated on the glass. Using both 1520 and 1210 nm wavelength, we observe upconversion emission at different wavelengths. Then, by drop coating UCNCs on gold film and by adding nanorods with plasmonic resonance at 808 and 980 nm, we observe selectively plasmonic enhanced upconversion emission.

Figure 3.4 (b) shows the upconversion plasmonic enhancement for the Er-doped UCNC under the excitation of the supercontinuum laser (wavelength $>$ 1200 nm). The blue peaks show dual-wavelength upconversion of Er-doped UCNCs when they are drop coated on the gold film, and the red peaks show the upconversion when the gold nanorods with resonance at 980 nm was added to the sample. Figure 3.4 (b) shows the transmission electron microscopy (TEM) image of UCNCs and gold nanorods.

Since 1210 and 1520 nm are in the solar spectrum, Er can be used to absorb and then upconvert these two bands to greater photon energy, which can be absorbed by silicon or other absorbing materials used in solar cells.

Chapter 4

Conclusions and Future Works

4.1 Conclusions

In this dissertation, plasmonic nanostructures have been used to enhance the interaction of light and matter, especially for enhancing the UCNCs. In the first project, rectangular apertures on a gold film are fabricated and used to trap and study single UCNCs. These apertures are finely tuned to find the highest UCNC emission enhancements. Results show a significant enhancement up to 400 × comparing to solution. The 550 nm and 650 nm upconversion wavelengths display polarization along the long and short axis perpendicularly. FDTD simulations show multiple plasmonics resonances at emission and absorption UCNCs wavelengths, which justify the emission enhancements.

In the second project, using the already designed plasmonic resonator in the first project, the UCNC emission of very low Erbium (Er) concentration is investigated. Results show discrete levels of emissions depending on the number of active Er inside the UCNC. This experiment displays that observing a single Er emitter is possible if the emission enhanced enough to overcome the spectroscopy noise. Moreover, using optical tweezers lets us isolate and translocate the trapped UCNC for a future application like single-photon sources.

In the third project, samples of gold NPs on SAMs on gold films are explored using the femtosecond pulse laser. The different upconverted lights are observed including second, third harmonic generations, two-photon photoluminescence, and bright broadband upconverted emission, which we believe is due to light-induced inelastic tunneling emission.

In the last project, dual-wavelength (1210 nm and 1520 nm) excitation has been used to observe upconversion in Er-doped UCNCs. The upconversion emissions are selectively enhanced using the nanorod plasmonic resonator at desired wavelengths.

To summarize, plasmonic subwavelength structures cause huge enhancement for the neighboring emitter, and it can increase the interaction of light and matter significantly if it is well designed.

4.2 Future Works

Single-photon sources and detectors are the major part of quantum technologies. Designing ideal or close to ideal single-photon sources operating at 1550 nm wavelengths is still challenging. Er-doped materials are one of the good candidates since they are non-blinking stable emitters that can emit at 1530 nm wavelength. The problem arises from the low emission rate of these emitters due to 4f orbital shielding. Many researchers try to solve this by using a photonic crystal or plasmonic cavity. Here, in this dissertation, we trapped single UCNCs with low Er doping inside a rectangular aperture with huge plasmonic enhancements. We designed these apertures for enhancing green and red light upconversion emission. However, it is possible to extend the size of the rectangular aperture to cover the desired wavelength (1530 nm). Now, by doing the same experiment (tuning the aperture size) and trapping with 980 nm laser, the downconversion emission from single UCNCs can be obtained at 1530 nm wavelength.

In the first experiment, we observe, the plasmonic aperture can alter the polarisation of emission. This could be very helpful in designing a single-photon source since one can obtain polarized single-photon sources. Also, changing the aperture size or using different apertures would be a great way to study this effect more.

We observe an interesting transmission signal on the APD, which was an oscillating signal changing from high to low frequency. This may happen due to the low viscosity of hexane and electromagnetic radiation pressure on the surface of the liquid. Exploring this effect would give us insight to the interaction of light, plasmonic resonators, nanoparticles, and low viscosity solutions.

Another interesting project would be measuring the time decay of a trapped UCNC when it is interacting with the subwavelength aperture. This also can be done by observing time decay for different emission polarization directions.

Bibliography

[1] Amirhossein Alizadehkhaledi, Adriaan L Frencken, Mohsen Kamandar Dezfouli, Stephen Hughes, F C J M van Veggel, and Reuven Gordon. Cascaded plasmon-enhanced emission from a single upconverting nanocrystal. *ACS Photonics*, 6(5):1125–1131, 2019.

[2] Amirhossein Alizadehkhaledi, Adriaan Frencken, Frank CJM van Veggel, and Reuven Gordon. Isolating nanocrystals with an individual erbium emitter: A route to a stable single-photon source at 1550 nm wavelength. *Nano Letters*, 2019.

[3] Mirali Seyed Shariatdoust, Adriaan L Frencken, Ali Khademi, Amirhossein Alizadehkhaledi, Frank CJM van Veggel, and Reuven Gordon. Harvesting dual-wavelength excitation with plasmon-enhanced emission from upconverting nanoparticles. *ACS Photonics*, 5(9):3507–3512, 2018.

[4] Steve Parker. *Color and vision : the evolution of eyes & perception.* Firefly Books, 1952.

[5] Shuming Nie and Steven R Emory. Probing single molecules and single nanoparticles by surface-enhanced raman scattering. *Science*, 275(5303):1102–1106, 1997.

[6] Katrin Kneipp, Yang Wang, Harald Kneipp, Lev T Perelman, Irving Itzkan, Ramachandra R Dasari, and Michael S Feld. Single molecule detection using surface-enhanced raman scattering (sers). *Phys. Rev. Lett.*, 78(9):1667, 1997.

[7] Alexandre G Brolo, Reuven Gordon, Brian Leathem, and Karen L Kavanagh. Surface plasmon sensor based on the enhanced light transmission through arrays of nanoholes in gold films. *Langmuir*, 20(12):4813–4815, 2004.

[8] Fatemeh Eftekhari, Carlos Escobedo, Jacqueline Ferreira, Xiaobo Duan, Emerson M Girotto, Alexandre G Brolo, Reuven Gordon, and David Sinton. Nanoholes as nanochannels: flow-through plasmonic sensing. *Analytical chemistry*, 81(11):4308–4311, 2009.

[9] Ragip A Pala, Justin White, Edward Barnard, John Liu, and Mark L Brongersma. Design of plasmonic thin-film solar cells with broadband absorption enhancements. *Advanced materials*, 21(34):3504–3509, 2009.

[10] Thang B Hoang, Gleb M Akselrod, and Maiken H Mikkelsen. Ultrafast room-temperature single photon emission from quantum dots coupled to plasmonic nanocavities. *Nano letters*, 16(1):270–275, 2015.

[11] Arthur Ashkin, James M Dziedzic, JE Bjorkholm, and Steven Chu. Observation of a single-beam gradient force optical trap for dielectric particles. *Optics letters*, 11(5):288–290, 1986.

[12] Bo Zhou, Bingyang Shi, Dayong Jin, and Xiaogang Liu. Controlling upconversion nanocrystals for emerging applications. *Nat. Nanotechnol.*, 10(11):924, 2015.

[13] Daniel J. Gargas, Emory M. Chan, Alexis D. Ostrowski, Shaul Aloni, M. Virginia P. Altoe, Edward S. Barnard, Babak Sanii, Jeffrey J. Urban, Delia J. Milliron, Bruce E. Cohen, and P. James Schuck. Engineering bright sub-10-nm upconverting nanocrystals for single-molecule imaging. *Nature Nanotechnology*, 9(4):300, 2014.

[14] Xiaoyong Huang, Sanyang Han, Wei Huang, and Xiaogang Liu. Enhancing solar cell efficiency: the search for luminescent materials as spectral converters. *Chemical Society Reviews*, 42(1):173–201, 2013.

[15] AM Dibos, M Raha, CM Phenicie, and Jeffrey Douglas Thompson. Atomic source of single photons in the telecom band. *Physical Review Letters*, 120(24):243601, 2018.

[16] Tian Zhong, Jonathan M Kindem, John G Bartholomew, Jake Rochman, Ioana Craiciu, Varun Verma, Sae Woo Nam, Francesco Marsili, Matthew D Shaw,

Andrew D Beyer, and Andrei Faraon. Optically addressing single rare-earth ions in a nanophotonic cavity. *Physical Review Letters*, 121(18):183603, 2018.

[17] Stefan Alexander Maier. *Plasmonics: fundamentals and applications*. Springer Science & Business Media, 2007.

[18] M Dragoman and D Dragoman. Plasmonics: Applications to nanoscale terahertz and optical devices. *Progress in Quantum Electronics*, 32(1):1–41, 2008.

[19] Ali Khademi, Timothy Dewolf, and Reuven Gordon. Quantum plasmonic epsilon near zero: field enhancement and cloaking. *Optics Express*, 26(12):15656–15664, 2018.

[20] Yangjun Cai, Yang Li, Peter Nordlander, and Paul S Cremer. Fabrication of elliptical nanorings with highly tunable and multiple plasmonic resonances. *Nano letters*, 12(9):4881–4888, 2012.

[21] D Rossouw, M Couillard, J Vickery, E Kumacheva, and GA Botton. Multipolar plasmonic resonances in silver nanowire antennas imaged with a subnanometer electron probe. *Nano Lett.*, 11(4):1499–1504, 2011.

[22] Peiyan Yuan, Yih Hong Lee, Muthu Kumara Gnanasammandhan, Zhenping Guan, Yong Zhang, and Qing-Hua Xu. Plasmon enhanced upconversion luminescence of $NaYF_4$: Yb, Er @ SiO_2 @ Ag core–shell nanocomposites for cell imaging. *Nanoscale*, 4(16):5132–5137, 2012.

[23] Di M Wu, Aitzol García-Etxarri, Alberto Salleo, and Jennifer A Dionne. Plasmon-enhanced upconversion. *The Journal of Physical Chemistry Letters*, 5(22):4020–4031, 2014.

[24] Matthew V DaCosta, Samer Doughan, Yi Han, and Ulrich J Krull. Lanthanide upconversion nanoparticles and applications in bioassays and bioimaging: A review. *Analytica chimica acta*, 832:1–33, 2014.

[25] JF Suyver, J Grimm, KW Krämer, and Hans-Ulrich Güdel. Highly efficient near-infrared to visible up-conversion process in $NaYF_4$: Er^{3+}, Yb^{3+}. *J. Lumin.*, 114(1):53–59, 2005.

[26] Pascal Anger, Palash Bharadwaj, and Lukas Novotny. Enhancement and quenching of single-molecule fluorescence. *Physical Review Letters*, 96(11):113002, 2006.

[27] Zhenhe Xu, Marta Quintanilla, Fiorenzo Vetrone, Alexander O Govorov, Mohamed Chaker, and Dongling Ma. Harvesting lost photons: plasmon and upconversion enhanced broadband photocatalytic activity in core@ shell microspheres based on lanthanide-doped $NaYF_4$, TiO_2, and Au. *Adv. Funct. Mater.*, 25(20):2950–2960, 2015.

[28] Feng Wang and Xiaogang Liu. Upconversion multicolor fine-tuning: visible to near-infrared emission from lanthanide-doped $NaYF_4$ nanoparticles. *Journal of the American Chemical Society*, 130(17):5642–5643, 2008.

[29] Nobel Media. The Nobel Prize in Physics 2018, year = 2019, url = https://www.nobelprize.org/prizes/physics/2018/summary/, urldate = 2019-07-17.

[30] Yuanjie Pang and Reuven Gordon. Optical trapping of a single protein. *Nano letters*, 12(1):402–406, 2011.

[31] Yasuhiro Harada and Toshimitsu Asakura. Radiation forces on a dielectric sphere in the rayleigh scattering regime. *Optics Communications*, 124(5-6):529–541, 1996.

[32] Reuven Gordon. Nanostructured metals for light-based technologies. *Nanotechnology*, 30(21):212001, 2019.

[33] Mathieu L Juan, Reuven Gordon, Yuanjie Pang, Fatima Eftekhari, and Romain Quidant. Self-induced back-action optical trapping of dielectric nanoparticles. *Nature Physics*, 5(12):915, 2009.

[34] Abhay Kotnala and Reuven Gordon. Quantification of high-efficiency trapping of nanoparticles in a double nanohole optical tweezer. *Nano letters*, 14(2):853–856, 2014.

[35] J Berthelot, SS Aćimović, ML Juan, MP Kreuzer, J Renger, and R Quidant. Three-dimensional manipulation with scanning near-field optical nanotweezers. *Nature Nanotechnology*, 9(4):295, 2014.

[36] Amirhossein Alizadehkhaledi, Adarsh Lalitha Ravindranath, Adriaan L Frencken, Ali Khademi, Mirali Seyed Shariatdoust, Frank CJM van Veggel, and Reuven Gordon. Trapping individual upconverters using rectangle nanoapertures. In *2018 IEEE 13th Nanotechnology Materials and Devices Conference (NMDC)*, pages 1–4. IEEE, 2018.

[37] Adarsh Lalitha Ravindranath, Amirhossein Alizadehkhaledi, Ali Khademi, Sara Ibrahim Omar, Jack Tuszynski, and Reuven Gordon. Characterizing mutant protein activators using single molecule optical trapping. In *2018 IEEE 13th Nanotechnology Materials and Devices Conference (NMDC)*, pages 1–4. IEEE, 2018.

[38] FJ García-Vidal, Luis Martín-Moreno, Esteban Moreno, LKS Kumar, and R Gordon. Transmission of light through a single rectangular hole in a real metal. *Physical Review B*, 74(15):153411, 2006.

[39] Hans Albrecht Bethe. Theory of diffraction by small holes. *Physical Review*, 66(7-8):163, 1944.

[40] Reuven Gordon and Alexandre G Brolo. Increased cut-off wavelength for a subwavelength hole in a real metal. *Optics Express*, 13(6):1933–1938, 2005.

[41] Hocheol Shin, Peter B Catrysse, and Shanhui Fan. Effect of the plasmonic dispersion relation on the transmission properties of subwavelength cylindrical

holes. *Physical Review B*, 72(8):085436, 2005.

[42] CK Chen, A Re B de Castro, and YR Shen. Surface-enhanced second-harmonic generation. *Physical Review Letters*, 46(2):145, 1981.

[43] HJ Simon, DE Mitchell, and JG Watson. Optical second-harmonic generation with surface plasmons in silver films. *Physical Review Letters*, 33(26):1531, 1974.

[44] Thomas YF Tsang. Surface-plasmon-enhanced third-harmonic generation in thin silver films. *Optics Letters*, 21(4):245–247, 1996.

[45] Markus Lippitz, Meindert A van Dijk, and Michel Orrit. Third-harmonic generation from single gold nanoparticles. *Nano Letters*, 5(4):799–802, 2005.

[46] Mark Fox. *Optical properties of solids*. American Association of Physics Teachers, 2002.

[47] Kane Yee. Numerical solution of initial boundary value problems involving maxwell's equations in isotropic media. *IEEE Transactions on antennas and propagation*, 14(3):302–307, 1966.

[48] Richard Courant, Kurt Friedrichs, and Hans Lewy. On the partial difference equations of mathematical physics. *IBM journal of Research and Development*, 11(2):215–234, 1967.

[49] Dawei Lu, Suehyun K Cho, Sungmo Ahn, Loic Brun, Christopher J Summers, and Wounjhang Park. Plasmon enhancement mechanism for the upconversion

processes in $NaYF_4$: Yb^{3+}, Er^{3+} nanoparticles: Maxwell versus forster. *ACS nano*, 8(8):7780–7792, 2014.

[50] Hari P Paudel, Lanlan Zhong, Khadijeh Bayat, Mahdi Farrokh Baroughi, Steve Smith, Cuikun Lin, Chaoyang Jiang, Mary T Berry, and P Stanley May. Enhancement of near-infrared-to-visible upconversion luminescence using engineered plasmonic gold surfaces. *The Journal of Physical Chemistry C*, 115(39):19028–19036, 2011.

[51] Takeho Aisaka, Minoru Fujii, and Shinji Hayashi. Enhancement of upconversion luminescence of er doped Al_2O_3 films by ag island films. *Applied Physics Letters*, 92(13):132105, 2008.

[52] Yi Wu, Xiang Shen, Shixun Dai, Yinsheng Xu, Feifei Chen, Changgui Lin, Tiefeng Xu, and Qiuhua Nie. Silver nanoparticles enhanced upconversion luminescence in Er^{3+}/Yb^{3+} codoped bismuth-germanate glasses. *The Journal of Physical Chemistry C*, 115(50):25040–25045, 2011.

[53] Marjan Saboktakin, Xingchen Ye, Uday K Chettiar, Nader Engheta, Christopher B Murray, and Cherie R Kagan. Plasmonic enhancement of nanophosphor upconversion luminescence in au nanohole arrays. *ACS Nano*, 7(8):7186–7192, 2013.

[54] Ewold Verhagen, L Kuipers, and Albert Polman. Field enhancement in metallic subwavelength aperture arrays probed by erbium upconversion luminescence. *Optics Express*, 17(17):14586–14598, 2009.

[55] Yingxian Xue, Chengjie Ding, Youying Rong, Qiang Ma, Chengda Pan, E Wu, Botao Wu, and Heping Zeng. Tuning plasmonic enhancement of single nanocrystal upconversion luminescence by varying gold nanorod diameter. *Small*, 13(36):1701155, 2017.

[56] Qiuqiang Zhan, Xin Zhang, Yuxiang Zhao, Jing Liu, and Sailing He. Tens of thousands-fold upconversion luminescence enhancement induced by a single gold nanorod. *Laser Photonics Rev.*, 9(5):479–487, 2015.

[57] R Kolesov, K Xia, R Reuter, R Stöhr, A Zappe, J Meijer, PR Hemmer, and J Wrachtrup. Optical detection of a single rare-earth ion in a crystal. *Nature Communications*, 3:1029, 2012.

[58] Tobias Utikal, Emanuel Eichhammer, Lutz Petersen, Alois Renn, Stephan Götzinger, and Vahid Sandoghdar. Spectroscopic detection and state preparation of a single praseodymium ion in a crystal. *Nature Communications*, 5:3627, 2014.

[59] Ippei Nakamura, Tatsuya Yoshihiro, Hironori Inagawa, Satoru Fujiyoshi, and Michio Matsushita. Spectroscopy of single Pr^{3+} ion in LaF_3 crystal at 1.5 k.

Scientific Reports, 4:7364, 2014.

[60] Emanuel Eichhammer, Tobias Utikal, Stephan Götzinger, and Vahid Sandoghdar. Spectroscopic detection of single Pr^{3+} ions on the $^3H_4 -^1 D_2$ transition. *New Journal of Physics*, 17(8):083018, 2015.

[61] Roman Kolesov, Kangwei Xia, Rolf Reuter, Mohammad Jamali, Rainer Stöhr, Tugrul Inal, Petr Siyushev, and Jörg Wrachtrup. Mapping spin coherence of a single rare-earth ion in a crystal onto a single photon polarization state. *Physical Review Letters*, 111(12):120502, 2013.

[62] P Siyushev, K Xia, R Reuter, M Jamali, N Zhao, N Yang, C Duan, N Kukharchyk, AD Wieck, R Kolesov, and J Wrachtrup. Coherent properties of single rare-earth spin qubits. *Nature Communications*, 5:3895, 2014.

[63] Kangwei Xia, Roman Kolesov, Ya Wang, Petr Siyushev, Rolf Reuter, Thomas Kornher, Nadezhda Kukharchyk, Andreas D Wieck, Bruno Villa, Sen Yang, and Jörg Wrachtrup. All-optical preparation of coherent dark states of a single rare earth ion spin in a crystal. *Physical Review Letters*, 115(9):093602, 2015.

[64] Chunming Yin, Milos Rancic, Gabriele G de Boo, Nikolas Stavrias, Jeffrey C McCallum, Matthew J Sellars, and Sven Rogge. Optical addressing of an individual erbium ion in silicon. *Nature*, 497(7447):91, 2013.

[65] Karin Groot-Berning, Thomas Kornher, Georg Jacob, Felix Stopp, Samuel T Dawkins, Roman Kolesov, Jörg Wrachtrup, Kilian Singer, and Ferdinand Schmidt-Kaler. Deterministic single ion implantation of rare-earth ions for nanometer resolution colour center generation. *Physical Review Letters*, 123:106802, 2019.

[66] Feng Wang, Juan Wang, and Xiaogang Liu. Direct evidence of a surface quenching effect on size-dependent luminescence of upconversion nanoparticles. *Angewandte Chemie International Edition*, 49(41):7456–7460, 2010.

[67] Yu Wang, Langping Tu, Junwei Zhao, Yajuan Sun, Xianggui Kong, and Hong Zhang. Upconversion luminescence of β-NaYF$_4$: Yb^{3+}, Er^{3+}@ β-NaYF$_4$ core/shell nanoparticles: excitation power density and surface dependence. *The Journal of Physical Chemistry C*, 113(17):7164–7169, 2009.

[68] Martti Kauranen and Anatoly V Zayats. Nonlinear plasmonics. *Nature Photonics*, 6(11):737, 2012.

[69] GT Boyd, ZH Yu, and YR Shen. Photoinduced luminescence from the noble metals and its enhancement on roughened surfaces. *Physical Review B*, 33(12):7923, 1986.

[70] Alexandre Bouhelier, Renaud Bachelot, Gilles Lerondel, Sergei Kostcheev, Pascal Royer, and GP Wiederrecht. Surface plasmon characteristics of tunable photo-

luminescence in single gold nanorods. *Physical Review Letters*, 95(26):267405, 2005.

[71] Peter Zijlstra, James WM Chon, and Min Gu. Five-dimensional optical recording mediated by surface plasmons in gold nanorods. *Nature*, 459(7245):410, 2009.

[72] Michael R Beversluis, Alexandre Bouhelier, and Lukas Novotny. Continuum generation from single gold nanostructures through near-field mediated intraband transitions. *Physical Review B*, 68(11):115433, 2003.

[73] Heykel Aouani, Mohsen Rahmani, Miguel Navarro-Cía, and Stefan A Maier. Third-harmonic-upconversion enhancement from a single semiconductor nanoparticle coupled to a plasmonic antenna. *Nature Nanotechnology*, 9(4):290, 2014.

[74] Marc Airola, Yongdong Liu, and Steve Blair. Second-harmonic generation from an array of sub-wavelength metal apertures. *Journal of Optics A: Pure and Applied Optics*, 7(2):S118, 2005.

[75] Ghazal Hajisalem, Mohammedreza S Nezami, and Reuven Gordon. Probing the quantum tunneling limit of plasmonic enhancement by third harmonic generation. *Nano Letters*, 14(11):6651–6654, 2014.

[76] Pavel N Melentiev, Anton E Afanasiev, Artur A Kuzin, Andrey S Baturin, and Victor I Balykin. Giant optical nonlinearity of a single plasmonic nanostructure. *Optics Express*, 21(12):13896–13905, 2013.

[77] JAH Van Nieuwstadt, M Sandtke, RH Harmsen, Franciscus B Segerink, JC Prangsma, Stefan Enoch, and L Kuipers. Strong modification of the nonlinear optical response of metallic subwavelength hole arrays. *Physical Review Letters*, 97(14):146102, 2006.

[78] Mohammadreza S Nezami, Daehan Yoo, Ghazal Hajisalem, Sang-Hyun Oh, and Reuven Gordon. Gap plasmon enhanced metasurface third-harmonic generation in transmission geometry. *ACS Photonics*, 3(8):1461–1467, 2016.

[79] Peter Hommelhoff, Yvan Sortais, Anoush Aghajani-Talesh, and Mark A Kasevich. Field emission tip as a nanometer source of free electron femtosecond pulses. *Physical Review Letters*, 96(7):077401, 2006.

[80] Peter Hommelhoff, Catherine Kealhofer, and Mark A Kasevich. Ultrafast electron pulses from a tungsten tip triggered by low-power femtosecond laser pulses. *Physical Review Letters*, 97(24):247402, 2006.

[81] G Herink, DR Solli, M Gulde, and C Ropers. Field-driven photoemission from nanostructures quenches the quiver motion. *Nature*, 483(7388):190, 2012.

[82] Peter Dombi, Anton Horl, Peter Racz, Istvan Marton, Andreas Trugler, Joachim R Krenn, and Ulrich Hohenester. Ultrafast strong-field photoemission from plasmonic nanoparticles. *Nano Letters*, 13(2):674–678, 2013.

[83] Michael Krüger, Markus Schenk, Michael Förster, and Peter Hommelhoff. Attosecond physics in photoemission from a metal nanotip. *Journal of Physics B: Atomic, Molecular and Optical Physics*, 45(7):074006, 2012.

[84] John Lambe and SL McCarthy. Light emission from inelastic electron tunneling. *Physical Review Letters*, 37(14):923, 1976.

[85] BNJ Persson and A Baratoff. Theory of photon emission in electron tunneling to metallic particles. *Physical Review Letters*, 68(21):3224, 1992.

[86] Peter Johansson, R Monreal, and Peter Apell. Theory for light emission from a scanning tunneling microscope. *Physical Review B*, 42(14):9210, 1990.

[87] Wei Du, Tao Wang, Hong-Son Chu, and Christian A Nijhuis. Highly efficient on-chip direct electronic–plasmonic transducers. *Nature Photonics*, 11(10):623, 2017.

[88] Haoliang Qian, Su-Wen Hsu, Kargal Gurunatha, Conor T Riley, Jie Zhao, Dylan Lu, Andrea R Tao, and Zhaowei Liu. Efficient light generation from enhanced inelastic electron tunnelling. *Nature Photonics*, 12:485–488, 2018.

[89] Kunta Yoshikawa, Hayato Kawasaki, Wataru Yoshida, Toru Irie, Katsunori Konishi, Kunihiro Nakano, Toshihiko Uto, Daisuke Adachi, Masanori Kanematsu, Hisashi Uzu, and Kenji Yamamoto. Silicon heterojunction solar cell with interdigitated back contacts for a photoconversion efficiency over 26%. *Nature Energy*, 2:17032, 2017.

[90] Daisuke Adachi, José Luis Hernández, and Kenji Yamamoto. Impact of carrier recombination on fill factor for large area heterojunction crystalline silicon solar cell with 25.1% efficiency. *Applied Physics Letters*, 107(23):233506, 2015.

[91] Martin A Green, Yoshihiro Hishikawa, Ewan D Dunlop, Dean H Levi, Jochen Hohl-Ebinger, and Anita WY Ho-Baillie. Solar cell efficiency tables (version 52). *Progress in Photovoltaics: Research and Applications*, 26(7):427–436, 2018.

[92] Anna L Hagstrom, Fan Deng, and Jae-Hong Kim. Enhanced triplet–triplet annihilation upconversion in dual-sensitizer systems: translating broadband light absorption to practical solid-state materials. *ACS Photonics*, 4(1):127–137, 2016.

[93] Laszlo Frazer, Joseph K Gallaher, and TW Schmidt. Optimizing the efficiency of solar photon upconversion. *ACS Energy Letters*, 2(6):1346–1354, 2017.

[94] François Auzel. Upconversion and anti-stokes processes with f and d ions in solids. *Chemical Reviews*, 104(1):139–174, 2004.

[95] Guan Sun, Ruolin Chen, Yujie J Ding, and Jacob B Khurgin. Upconversion due to optical-phonon-assisted anti-stokes photoluminescence in bulk gan. *ACS Photonics*, 2(5):628–632, 2015.

Appendix

A Cascaded Plasmon-Enhanced Emission from a Single Upconverting Nanocrystal

(2019, ACS Photonics, volume 6, pp 1125-1131)

Cascaded plasmon-enhanced emission from a single upconverting nanocrystal

Amirhossein Alizadehkhaledi,[†,‖] Adriaan L. Frencken,[‡,‖] Mohsen Kamandar Dezfouli,[¶] Stephen Hughes,[§] Frank C.J.M. van Veggel,[‡,‖] and Reuven Gordon[*,†,‖]

†*Department Electrical and Computer Engineering, University of Victoria, Victoria, British Columbia V8P 5C2, Canada*

‡*Department of Chemistry, University of Victoria, British Colombia V8W 3V6, Canada*

¶*Advanced Electronics and Photonics Research Centre, National Research Council Canada, 1200 Montreal Rd., Ottawa, ON K1A 0R6, Canada*

§*Department of Physics, Engineering Physics and Astronomy, Queen's University, Kingston, Ontario K7L 3N6, Canada*

‖*Centre for Advanced Materials & Related Technologies (CAMTEC), University of Victoria, Victoria, British Columbia V8W 2Y2, Canada*

E-mail: rgordon@uvic.ca

Phone: +1 250 472 5179 . Fax: +1 250 721 6052

Abstract

Plasmonics has been used to enhance light-matter interaction at the extreme subwavelength scale. Intriguingly, it is possible to achieve multiple plasmonic resonances from a single nanostructure and these can be used in combination to provide cascaded enhanced interactions. Here, we demonstrate three distinct plasmon resonances for enhanced up-conversion emission from a single up-converting nanocrystal trapped in a metal nanoaperture optical tweezer. For apertures where the plasmonic resonances occur at the emission wavelengths only, a moderate enhancement of a factor of 4 is seen. However, by tuning the aperture to enhance the excitation laser as well, an *additional* factor of 100 enhancement in the emission is achieved. Since lanthanide doped nanocrystals are stable emitters, this approach of using multiple subwavelength resonances can improve applications including photovoltaics, photocatalysis and imaging. The nanocrystals can also contain only single ions, allowing for studying quantum emitter properties and applications to single photon sources.

Keywords

upconverting nanoparticles; plasmon enhanced emission; lanthanides, optical tweezer, rectangular aperture, single particle luminescence

Nanostructured metals concentrate light to the nanometer scale and this has been exploited in many applications to enhance light-matter interaction, in the field widely referred to as plasmonics. Generally speaking, the enhancement can appear in two ways: for the incident light and the emitted light. The ultimate goal would be to benefit from both simultaneously.(A1) The greatest enhancements are expected for multi-photon processes where the plasmonic improvement occurs at an exponent greater than unity. Many applications require significantly different wavelengths for the incident and emitted photons, such that a single plasmonic resonance cannot enhance both simultaneously, even though they are broadband resonances. An obvious exception is for Raman scattering where the incident and emitted photons have almost the same wavelength and single molecule sensitivity has been achieved.(A2),(A3) Therefore, it is desirable in general to have plasmonic structures with multiple resonances at the different wavelengths of interest, and all at the extreme subwavelength scale.(A4),(A5)

A single UCNC contains many coupled lanthanide ions, which give rise to complicated kinetics within and between thousands of excited states. Plasmon resonances can influence UCNC efficiency in three different ways. First, by concentrating and increasing the incident field, which results in enhanced absorption. Second, by enhancing emission by increasing the radiative decay rate. Third, by increasing the non-radiative decay rate.(A6) Consequently, plasmon resonances can both enhance and hinder UCNC efficiency.(A7) If designed correctly, plasmonic enhancement in upconversion has potential for improving solar energy harvesting,(A8),(A9) photocatalysis,(A10) single photon sources(A11),(A12) and subwavelength luminescence imaging with IR excitation.(A9),(A13) While these emitters have excellent stability, their very weak conversion efficiency has been widely recognized as hindering any practical use.(A14),(A15) This is exactly a case where multiple plasmonic resonances are desired, which has been achieved for excitation and emission wavelengths for aperture arrays in metals;(A16),(A17) however, achieving all of these resonances at the subwavelength scale and for a single upconverting nanocrystal (UCNC) and a single aperture remains a significant challenge. There have been efforts to explore the plasmonic enhancement from single nanorods. In one study, the individual nanorod-UCNC interaction was achieved by atomic force manipulation of the particles.(A18) The nanorods used in that study only received a very small enhancement at the excitation wavelength, since the nanorods were not tuned to that wavelength. Others have explored nanorods with dual plasmonic resonances at the excitation and emission wavelengths; however, that work relied on the stochastic nature of the particles diffusing in solution and so there was a lot of variation in the emission reported .(A19) The nanoapertures used here are tuned in fine steps about the plasmonic resonance, allowing for matching the resonance exactly and obtaining the maximum enhancement. The trapping used also allows for systematic study of a single UCNC interacting with a single aperture.

Here we present a nanoaperture optical tweezer platform(A20) as a means to obtaining three separate resonances in a single subwavelength structure. By using this platform, we obtain bright emission from individual 26 nm UCNCs (The UCNCs are made of $NaYF_4$ doped with 18% Yb and 2% Er. No passivating shell has been used which allows for the closest spacing of the emitters to the gold) 400 times greater than the same measurements performed on a collection of these particles. While two of the plasmonic resonances are largely unaltered by changing the aperture dimensions, tuning the long axis of the aperture results in an additional 100 times increase in the already-enhanced emission. We also present a simple theoretical model to better understand these features, which exploits full 3D finite-difference time-domain (FDTD) simulations.

We synthesised 26 nm upconverting nanocrystals (UCNCs) and trapped them using a laser tweezer setup. The laser tweezer setup uses a rectangular aperture in a 100 nm thick gold film to allow for trapping single nanoparticles. The trapping is measured by an abrupt jump in the transmission of light through the aperture, as shown in Fig. A1 (a,b). Trapping occurred consistently within 0.01 s of turning on the laser, as expected from diffusion considerations for the concentration of $3 \times 10^{10}/\mathrm{cm}^3$ (see Supporting information, SI, Section C). In addition, we could image the luminescence from the UCNC at the time of trapping, as shown in Figs.A1(c)-(e). The transmission through the aperture consistently showed interesting dynamics over multiple timescales that we suspect are related to the interesting nanofluidics of this system. We do not investigate this behavior in the present work; however, multiple events are presented in the SI to show that this behaviour is highly reproducible.

To tune the plasmonic resonance, a variety of rectangular apertures of different dimensions were fabricated. One side-length of the apertures was varied from 100 nm to 226 nm. A test pattern containing all of the aperture sizes fabricated is shown in Fig. A2(a); however, it should be emphasized that trapping was done on one aperture at a time and they were separated by 40 microns. In addition, Fig. A2(a) shows a schematic of trapping UCNCs and their emission. The 980 nm laser traps the UCNC near a long axis of rectangle aperture. The 980 nm also act as an excitation source for UCNC, which emits at 550 nm and 650 nm. Figure A2(b) displays energy-transfer upconversion diagram for the Yb^{3+} and Er^{3+} codoped upconversion materials. Three phenomena in the emission process of UCNCs play roles: the light absorption by Yb^{3+} (980 nm), the energy transfer from Yb^{3+} to Er^{3+} and the emission of ER^{3+}(550 nm and 650 nm), which are all subject to plasmonic enhancement in this work. Figure A2(c) shows the upconversion emission collected by a spectrometer for an acquisition time of 10 seconds. To be sure that the collected emission was from a single trapped particle, several measurements were taken. When a single particle was trapped, the intensity was consistently lower by a factor of two (at least) (see SI, Section D). The normalized standard deviation over different measurements of a single particle for each aperture was 5.1 % and 5.6 % for the 550 nm and 650 nm emission.

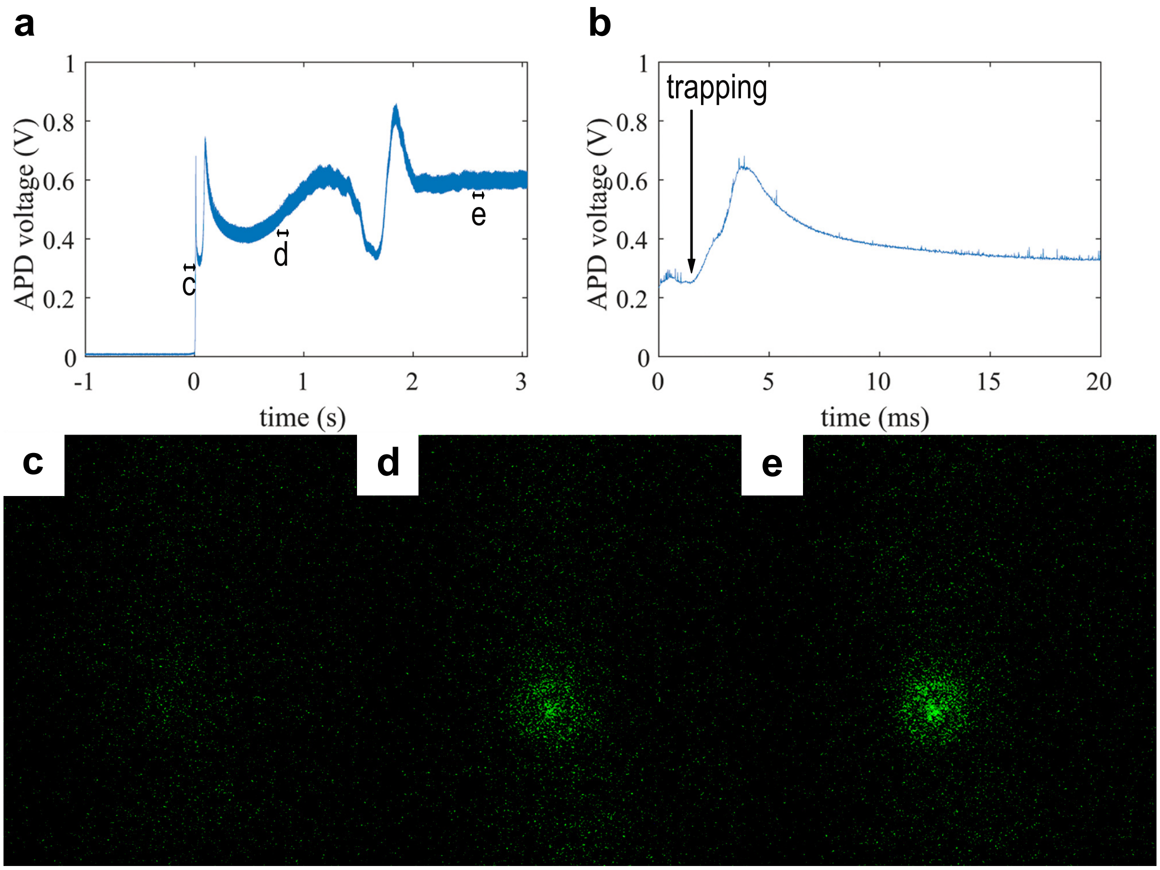

Figure A1: **Optical trapping and imaging of individual UCNCs**. **a**, Optical transmission through a 100 nm × 100 nm aperture in a metal film. Laser is turned on at 0 s. **b**, Magnified region showing the jump at trapping shortly after laser is turned on.2- Trapping time is approximately 2 ms. **c,d,e**, luminescence images at different times shown in part (a). (c) shows when the laser is first turned on, (d) is when the UCNC is trapped, and (e) is after a few seconds when luminescence is brighter and more stable.

For the free solution, the concentration is 1000 times higher than the sample used for trapping. This gives us 30 particles per μm^3 (beam width of laser is approximately 1 μm) which is a conservative linear estimate. Since the excitation is a nonlinear process, the actual count would be even smaller. To ensure consistency for comparison, the measurements were all carried out using solution based samples (trapping and free solution). The laser power is maintained at 30 mW for the trapping and the control (free solution) measurements. The nanoaperture increases the local intensity, so a direct comparison based on intensity cannot be made (and indeed, the plasmonic enhancement in the excitation is part of the enhancement obtained in this experiment). Figure A2(d) shows the enhancement factor (using the free-solution as a reference) of the upconversion at 550 nm and 650 nm as a function of aperture size, showing a 100 times increase in the enhancement factor when going from a 100 × 100 nm aperture to a 212 × 100 nm aperture. The overall enhancement factor is 400.

To help understanding the observed enhancement, we have performed electromagnetic analysis of the nanoapertures. Figure A3(a) shows the near-field (absolute value of electric field) distribution in the aperture for 980 nm wavelength as calculated by FDTD simulations. The units are normalized to the incident plane wave. We analyze the enhancement seen for a UCNC at the position shown in this plot (hexagonal outline), which is assumed to be the trapping location because it has the highest intensity.(A20) Figure A3(b,c) show the Purcell enhancement factors (i.e., the enhanced emission rates) for a dipole at the position of trapping for polarization along the short axis, y, and long axis, x. This figure shows three spectral bands with enhanced emission coupling. The band at 530 nm does not show significant tuning with changes in aperture length. This band is expected from the surface plasmon resonance that arises simply from being near a metal surface.(A21) This plasmonic resonance enhances the emission at 550 nm, seen for both polarizations. The band at 660 nm, seen for short axis polarization, shows a small amount of tuning with aperture size. This plasmonic

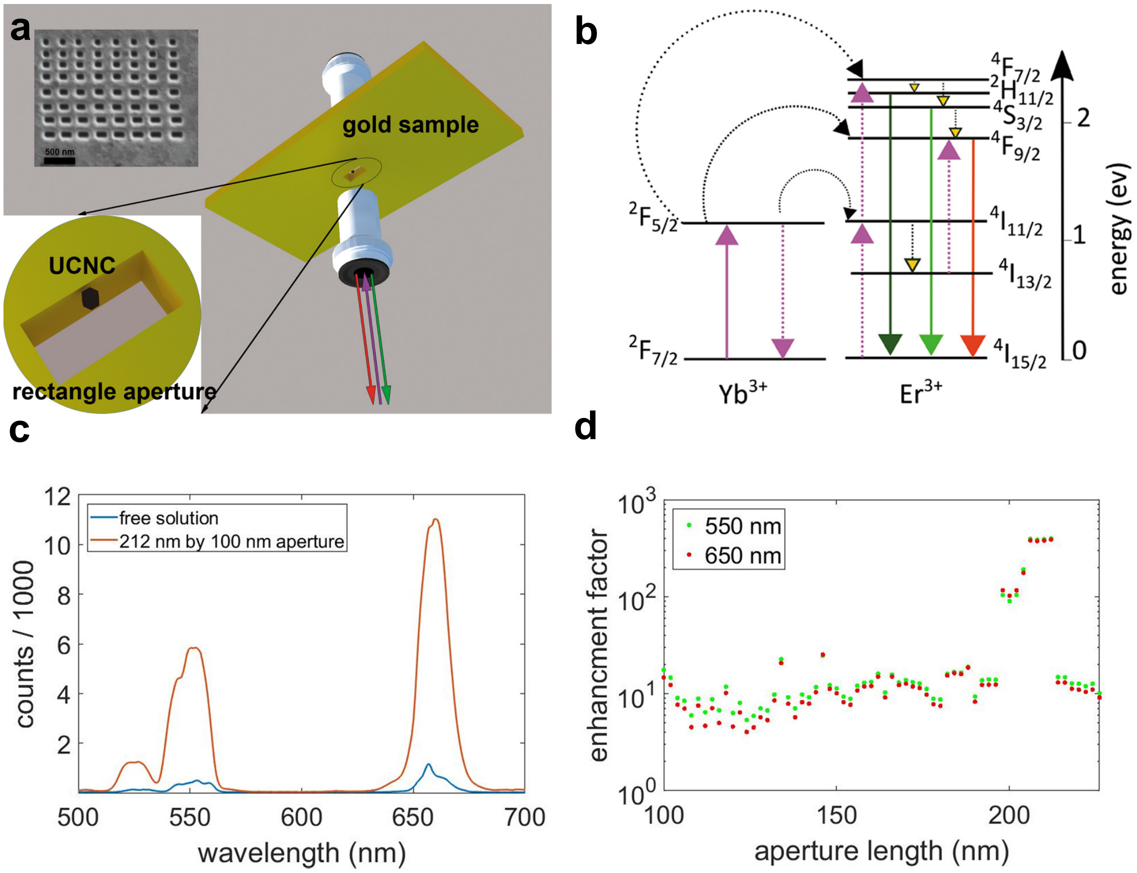

Figure A2: **Tuning the plasmonic upconversion emission enhancement**. **a**, Schematics of trapped UCNC in rectangle aperture on gold sample, and focused ion beam image of test pattern of all 64 fabricated rectangular aperture dimensions (although they were separated from one another in the actually trapping experiment). One of the dimensions of the aperture is fixed at 100 nm. The other dimension is varied from 100 nm to 226 nm in 2 nm steps. **b**, Energy transfer schematic of upconversion mechanism for the Er^{3+}, Yb^{3+}. Upconversion absorption (solid purple arrow), energy transfer (dashed purple arrows), nonradiative relaxation (dotted yellow arrows), and 520 nm, 550 nm, 650 nm emissions (dark green, light green and red arrows) are illustrated. **c**, Upconversion emission spectra for UCNCs in free solution (blue) at 1000 times higher concentration than UCNC emission of single particle in 212 nm × 100 nm aperture (red). The incident power is 30 mW. **d**,Upconversion enhancement of 550 nm and 650 nm emission when varying the aperture length for the same excitation conditions.

resonance enhances the emission at 650 nm. The long wavelength band, which comes from the cut-off plasmonic resonance of the aperture as shown in Fig. A3(a), is seen to tune substantially with aperture size. This resonance overlaps with the excitation wavelength for lengths around 185 nm.

The observed geometry of enhancement is consistent with the increase in emission observed for apertures in this range in Fig. A2(c). To be more quantitative, we formulate an enhancement factor as the Purcell enhancement at the excitation wavelength squared (since it is a two photon process) times the enhancement at the emission wavelength, as shown in Fig. A3(d). The magnitude of enhancement is in reasonable agreement with the actual observed enhancement, especially considering that there are no free parameters in our model, there are clearly fabrication tolerances, and the UCNC will experience Brownian motion so that it will not be perfectly confined to the highest intensity region. We use the non-local Purcell factor, which removes the quenched part and only looks at the radiated part. The quenched part still exists and is accounted for by the theory, but we do not include in the calculation of the emission .

Several works have attempted to understand the detailed kinetics of upconversion. Here we focus only on the plasmonic enhancement. That said, it appears that the experiments are in the first order kinetics regime we are focusing high intensity onto a single UCNC. Certainly, the linear regime of power dependence seems to confirm this observation (see SI, Section E). We expect that future dynamic experimental studies will support a more comprehensive dynamic model, as has been done in the past.(A22),(A23) We have also investigated the power dependence of the upconversion to explore the interaction between the 550 nm and 650 nm transitions. This “nonlinear” behavior goes beyond the simple modeling presented above and will likely require more complicated rate equation analysis (as well as benefit from time-domain studies not presently within our capability).(A24)–(A26) As the pumping power at 980 nm increases,

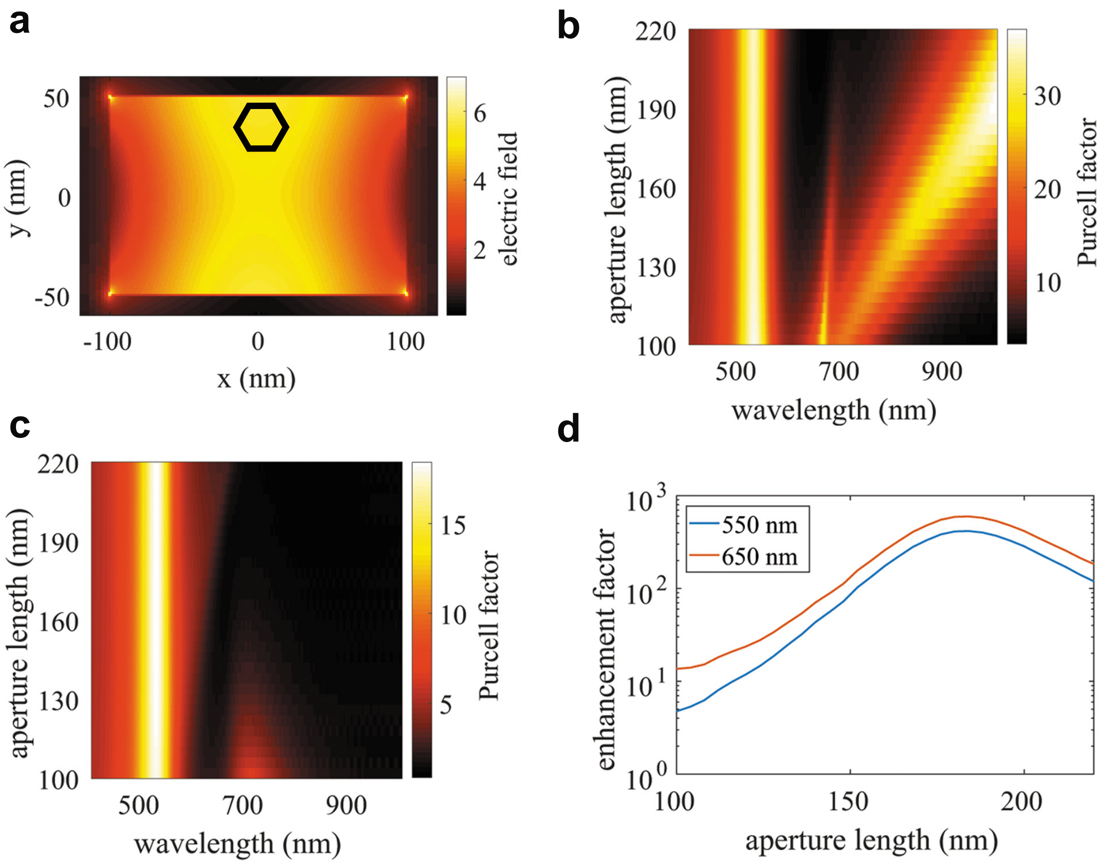

Figure A3: **Simulations of multiple plasmonic enhancement for UCNC trapped in a rectangular metal aperture.** **a** Simulation of electric field amplitude of 980 nm wavelength (normalized to incident field amplitude) in aperture for cross section at $z = 0$. Expected trapping location of UCNC is shown as hexagonal black line. (b,c) Purcell factor F_{P} at the position trapping (defined as the centre of UCNC in (a)) for polarization along the short axis (b) and long axis (c). **d** Enhancement factor, η expected by multiplying the Purcell factor at the excitation wavelength squared by the Purcell at the emission wavelength accounting for outcoupling efficiency as described in Methods.

the 650 nm emission increases with respect to the 550 nm (see SI, Figure S11). When the emission enhancement increases, the ratio between the 650 nm and 550 nm emission also increases (see SI, Figure S10). UCNCs generally exhibit increasing red to green emission ratio with increasing incident power, which can be understood in terms of several past studies.(A27),(A28) The various relaxation processes that govern this ratio have been studied in detail elsewhere. Related to the interaction between the different transitions is the polarization of the output emission. We observe that the emission at 650 nm is polarized along the short axis of the aperture (the same polarization as the incident pump and the plasmon resonances), and the 550 nm emission is orthogonally polarized (see SI, Figure S12). This may be because the 650 nm transition is dominating the competition for the short-axis polarization, but the 550 nm dominates for the orthogonal polarization where there is no plasmonic mode for 650 nm (see Fig. A3(d)).

Other works have reported on the polarization for upconverters coupled to nanorods(A29) which show orthogonal polarization. When we apply similar analysis to their work in our case, the emission would be polarized along the common short axis, so we believe that the competition between the transitions is necessary to fully understand this behavior. In the future, we hope to complete polarization resolved time-domain measurements to try to build a model to potentially explain these results.(A30) However, we do not rule out anisotropy of the particle in the trapping potentially playing some role in the polarization.(A31) We note that others have probed single and few UCNCs in optical tweezer systems in the past (without plasmonic enhancement); those works did not report on any polarization dependence.(A32),(A33) The data reported here motivates investigation of using a 1550 nm plasmonic resonance by increasing the long axes of the rectangular aperture. This is of interest enhanced rates of emission at this interesting fiber optic communication wavelength. To achieve this goal, we will need to use a modified optical setup, which can detect up to 1550 nm wavelength.

Conclusions

In conclusion, we have demonstrated cascaded plasmonic resonances in a subwavelength aperture in a metal film can be used to enhance the upconversion of a single trapped UCNC. The use of multiple plasmonic resonances is a promising path to enhancing the emission of UCNCs for applications including photovoltaics, photocatalysis, single photon sources and biomedical imaging. While ultimately the aperture geometry we have chosen may not be used in those applications (it is definitely useful here for optical trapping), the principle of using multiple subwavelength plasmonic resonances, especially at the pump wavelength, has clear benefits. The main features are supported with full 3D FDTD simulations for the metallic apertures.

Methods

UCNC ($NaYF_4$:18% Yb, 2% Er UCNCs (102AF18)) synthesis and characterization

Chemicals

Yttrium(III) chloride hexahydrate (99.99%), ytterbium(III) chloride (99.998%), erbium(III) chloride hexahydrate (99.995%), ammonium fluoride (99.99%), tech grade oleic acid (90%), tech grade 1-octadecene (90%), and hexanes were purchased from Sigma-Aldrich. Anhydrous ethanol from Commercial Alcohols, methanol from Caledon, and sodium hydroxide from Bio Basic Canada inc. were used. All chemicals were used as received.

Synthesis

A synthesis was adapted from a previously reported procedure.(A34) To a 3-neck roundbottom flask, 240.3 mg $YCl_3 \cdot (H_2O)_6$, 77.8 mg $YbCl_3(H_2O)_6$ and 8.7 mg $ErCl_3 \cdot (H_2O)_6$ were added together with 15 mL octadecene and 5 mL oleic acid. The mixture was heated to 160 °C under vacuum and kept at that temperature for 30 minutes before cooling to room temperature. Once cooled, a solution of 107 mg NaOH and 152 mg NH_4F in 10 mL MeOH was added dropwise while stirring. The mixture was heated to 65 °C 120 minutes to evaporate the MeOH. The temperature was then raised to 298°C over 20 minutes (11.75°C/min.) Temperature was kept between 305 and 307°C for 90 minutes. The mixture was then cooled, washed with 20 mL EtOH, centrifuged at 1800 g for 10 min, and washed with excess EtOH again before redispersion in 20 mL hexane.

UCNCs Characterization

Transmission electron microscopy images were obtained using a JEOL JEM-1400 microscope operating at 80 kV. Hexane dispersions of the UCNCs were drop-cast on a Formvar carbon- oated grid (300 mesh Cu) and air-dried before imaging. Size analysis of NCs from the images was performed by measuring the surface area of at least 300 particles. X-ray diffractograms with a resolution of 0.0263 °2ϑwere collected using a PANalytical Empyrean X-ray System with a Cu source (Kαradiation, λ= 1.54060 Å) operating at 45 kV and 40 mA. See SI (Section A) for additional data.

Fabrication of rectangular aperture

The rectangular apertures were fabricated by focused ion beam milling (Hitachi FB-2100) of a commercially available slide with a 100 nm gold layer on a glass substrate (EMF Corp.) and a 5 nm Ti adhesion layer.

Optical trapping

A continuous wave 980 nm single-beam laser was collimated, expanded, and focused onto the sample using a 100× oil immersion microscope objective (1.25 numerical aperture). This beam serves both as trapping beam and the excitation source for UCNCs. A 10× condenser microscopic objective (0.25 numerical aperture) was used to collect the transmitted signal through the rectangle aperture and was measured by a silicon-based avalanche photodetector (Thorlabs APD110A). A piezoelectric controlled 3-axis sample stage was used to aligned the beam through the rectangle apertures with 20 nm positioning precision. A half-wave plate (HWP) and linear polarizer (LP) were used to orient the polarization of the pump beam. Measurements were obtained after altering the HWP and LP orientation for obtaining the highest transmission of laser beam through the aperture (the incident laser is made to be always linearly polarized along the short axes of the aperture). A 750 nm short pass filter (Thorlabs FES0750) was used on CCD camera and spectrometer to minimize the trapping beam intensity. Additionally, a 850 nm short pass filter (Thorlabs FES0850) was used to completely eliminate the 980 nm laser on CCD camera to view the particle coming into the aperture. The luminescence spectrum was measured using a QE65000 Ocean Optics spectrometer. In order to investigate the polarization of the upconverted emission a linear polarizer was placed before the spectrometer.

Numerical simulations

All numerical simulations were carried out using the 3D FDTD from the commercial package of Lumerical. Independent dipole excitations oriented along both the long axis (x) and the short axis (y) of the aperture were used at position $\mathbf{r} = (0, 33, 0)$ nm where the origin was placed in the middle of the aperture. A computational domain size of $6 \times 6 \times 2$ μm^3 was terminated with perfectly matched layers and a mesh of 2 nm was used over the aperture. Within each dipole simulation, both the generalized

Purcell factor (enhanced emission factor, projected onto the direction of interest) and the farfield emission was evaluated. The farfield emission in particular was measured over a z-normal plane above the aperture at the height of $z = 1\,\mu m$. Data gathered from both x-dipole and y-dipole calculations was used to arrive at the enhancement factor, η presented in the main text, as we define below:

$$\eta = F_{\mathrm{P}}^2(\lambda_i) \times \xi(\lambda_e), \tag{A1}$$

where $\lambda_i = 980$ nm is the incident wavelength, F_{P} is the Purcell factor for the x oriented dipole, λ_e is the emitted wavelength (either 550 nm or 650 nm), ξ is the outcoupling efficiency (including the local field enhancement); ξ is calculated using y-dipole for the 650 nm detection, or x-dipole for the 550 nm detection, to account for the emission anisotropy observed in experiment (see main text for discussion). To arrive at the field distribution inside the aperture, also shown in the main text, total-field scatter-field studies were performed on a smaller domain size of $2 \times 2 \times 2\ \mu m^3$ using a y-polarized dipole source.

Associated content

Supporting information

Characterization of the UCNCs, description of the optical trapping setup with 9 additional trapping events, calculation for diffusion time to trap, the emission at 650 nm and 550 nm as a function of pump power, the ratio between 650 nm and 550 nm emission as function of aperture size and of pump power for a single aperture, and the polarization dependence of upconverted emission

Author information

Corresponding author

*E-mail (R. Gordon): rgordon@uvic.ca

ORCID

Reuven Gordon: 0000-0002-1485-6067

Author contributions

AA performed the trapping experiments. ALF and FCJMvV were responsible for nanocrystal synthesis and characterization. MKD and SH provided theory to interpret the experimental findings. RG conceived of the experiment. All authors assisted in writing the manuscript.

Competing interests

The authors declare no competing interests.

Acknowledgments

The authors acknowledge funding support from the NSERC CREATE program Materials for Enhanced Energy Technologies (MEET) and the NSERC Discovery Grants program.

References

[A1] Schuller, J. A.; Barnard, E. S.; Cai, W.; Jun, Y. C.; White, J. S.; Brongersma, M. L. Plasmonics for extreme light concentration and manipulation. *Nat. Mater.* **2010**, *9*, 193.

[A2] Nie, S.; Emory, S. R. Probing single molecules and single nanoparticles by surface-enhanced Raman scattering. *Science* **1997**, *275*, 1102–1106.

[A3] Kneipp, K.; Wang, Y.; Kneipp, H.; Perelman, L. T.; Itzkan, I.; Dasari, R. R.; Feld, M. S. Single molecule detection using surface-enhanced Raman scattering (SERS). *Phys. Rev. Lett.* **1997**, *78*, 1667.

[A4] Rossouw, D.; Couillard, M.; Vickery, J.; Kumacheva, E.; Botton, G. Multipolar plasmonic resonances in silver nanowire antennas imaged with a subnanometer electron probe. *Nano Lett.* **2011**, *11*, 1499–1504.

[A5] Thyagarajan, K.; Rivier, S.; Lovera, A.; Martin, O. J. Enhanced second-harmonic generation from double resonant plasmonic antennae. *Opt. Express* **2012**, *20*, 12860–12865.

[A6] Wu, D. M.; García-Etxarri, A.; Salleo, A.; Dionne, J. A. Plasmon-enhanced upconversion. *J. Phys. Chem. Lett.* **2014**, *5*, 4020–4031.

[A7] Yuan, P.; Lee, Y. H.; Gnanasammandhan, M. K.; Guan, Z.; Zhang, Y.; Xu, Q.-H. Plasmon enhanced upconversion luminescence of $NaYF_4$: Yb, Er @ SiO_2 @ Ag core–shell nanocomposites for cell imaging. *Nanoscale* **2012**, *4*, 5132–5137.

[A8] Huang, X.; Han, S.; Huang, W.; Liu, X. Enhancing solar cell efficiency: the search for luminescent materials as spectral converters. *Chem. Soc. Rev.* **2013**, *42*, 173–201.

[A9] Zhou, B.; Shi, B.; Jin, D.; Liu, X. Controlling upconversion nanocrystals for emerging applications. *Nat. Nanotechnol.* **2015**, *10*, 924.

[A10] Xu, Z.; Quintanilla, M.; Vetrone, F.; Govorov, A. O.; Chaker, M.; Ma, D. Harvesting lost photons: plasmon and upconversion enhanced broadband photocatalytic activity in core@ shell microspheres based on lanthanide-doped $NaYF_4$, TiO_2, and Au. *Adv. Funct. Mater.* **2015**, *25*, 2950–2960.

[A11] Dibos, A.; Raha, M.; Phenicie, C.; Thompson, J. Atomic Source of Single Photons in the Telecom Band. *Phys. Rev. Lett.* **2018**, *120*, 243601.

[A12] Zhong, T.; Kindem, J. M.; Bartholomew, J. G.; Rochman, J.; Craiciu, I.; Verma, V.; Nam, S. W.; Marsili, F.; Shaw, M. D.; Beyer, A. D.; Faraon, A. Optically addressing single rare-earth ions in a nanophotonic cavity. *Phys. Rev. Lett.* **2018**, *121*, 183603.

[A13] Gargas, D. J.; Chan, E. M.; Ostrowski, A. D.; Aloni, S.; Altoe, M. V. P.; Barnard, E. S.; Sanii, B.; Urban, J. J.; Milliron, D. J.; Cohen, B. E.; Schuck, P. J. Engineering bright sub-10-nm upconverting nanocrystals for single-molecule imaging. *Nat. Nanotechnol.* **2014**, *9*, 300.

[A14] Rabouw, F. T.; Prins, P. T.; Villanueva-Delgado, P.; Castelijns, M.; Geitenbeek, R. G.; Meijerink, A. Quenching Pathways in $NaYF_4$: Er^{3+}, Yb^{3+} Upconversion Nanocrystals. *ACS Nano* **2018**, *12*, 4812–4823.

[A15] Wisser, M. D.; Fischer, S.; Siefe, C.; Alivisatos, A. P.; Salleo, A.; Dionne, J. A. Improving Quantum Yield of Upconverting Nanoparticles in Aqueous Media via Emission Sensitization. *Nano Lett.* **2018**, *18*, 2689–2695.

[A16] Saboktakin, M.; Ye, X.; Chettiar, U. K.; Engheta, N.; Murray, C. B.; Kagan, C. R. Plasmonic enhancement of nanophosphor upconversion luminescence in Au nanohole arrays. *ACS Nano* **2013**, *7*, 7186–7192.

[A17] Verhagen, E.; Kuipers, L.; Polman, A. Field enhancement in metallic subwavelength aperture arrays probed by erbium upconversion luminescence. *Opt. Express* **2009**, *17*, 14586–14598.

[A18] Xue, Y.; Ding, C.; Rong, Y.; Ma, Q.; Pan, C.; Wu, E.; Wu, B.; Zeng, H. Tuning plasmonic enhancement of single nanocrystal upconversion luminescence by varying gold nanorod diameter. *small* **2017**, *13*, 1701155.

[A19] Zhan, Q.; Zhang, X.; Zhao, Y.; Liu, J.; He, S. Tens of thousands-fold upconversion luminescence enhancement induced by a single gold nanorod. *Laser Photonics Rev.* **2015**, *9*, 479–487.

[A20] Juan, M. L.; Gordon, R.; Pang, Y.; Eftekhari, F.; Quidant, R. Self-induced back-action optical trapping of dielectric nanoparticles. *Nat. Phys.* **2009**, *5*, 915.

[A21] Ritchie, R. Plasma losses by fast electrons in thin films. *Phys. Rev.* **1957**, *106*, 874.

[A22] Piper, R. B.; Yoshida, M.; Farrell, D. J.; Khoury, T.; Crossley, M. J.; Schmidt, T. W.; Haque, S. A.; Ekins-Daukes, N. Kinetic insight into bimolecular upconversion: experiment and simulation. *Rsc Advances* **2014**, *4*, 8059–8063.

[A23] Lu, D.; Cho, S. K.; Ahn, S.; Brun, L.; Summers, C. J.; Park, W. Plasmon enhancement mechanism for the upconversion processes in $NaYF_4$: Yb^{3+}, Er^{3+} nanoparticles: Maxwell versus Forster. *ACS nano* **2014**, *8*, 7780–7792.

[A24] Zhang, J.; Hao, Z.; Li, J.; Zhang, X.; Luo, Y.; Pan, G. Observation of efficient population of the red-emitting state from the green state by non-multiphonon relaxation in the Er^{3+}–Yb^{3+} system. *Light Sci. Appl.* **2015**, *4*, e239.

[A25] Solis, D.; De la Rosa, E.; Meza, O.; Diaz-Torres, L.; Salas, P.; Angeles-Chavez, C. Role of Yb^{3+} and Er^{3+} concentration on the tunability of green-yellow-red upconversion emission of codoped ZrO_2: Yb^{3+}–Er^{3+} nanocrystals. *J. Appl. Phys.* **2010**, *108*, 023103.

[A26] Berry, M. T.; May, P. S. Disputed mechanism for NIR-to-red upconversion luminescence in $NaYF_4$: Yb^{3+}, Er^{3+}. *J. Phys. Chem. A* **2015**, *119*, 9805–9811.

[A27] Suyver, J.; Grimm, J.; Krämer, K.; Güdel, H.-U. Highly efficient near-infrared to visible up-conversion process in $NaYF_4$: Er^{3+}, Yb^{3+}. *J. Lumin.* **2005**, *114*, 53–59.

[A28] Chan, E. M.; Han, G.; Goldberg, J. D.; Gargas, D. J.; Ostrowski, A. D.; Schuck, P. J.; Cohen, B. E.; Milliron, D. J. Combinatorial discovery of lanthanide-doped nanocrystals with spectrally pure upconverted emission. *Nano Lett.* **2012**, *12*, 3839–3845.

[A29] He, J.; Zheng, W.; Ligmajer, F.; Chan, C.-F.; Bao, Z.; Wong, K.-L.; Chen, X.; Hao, J.; Dai, J.; Yu, S.-F.; Lei, D. Y. Plasmonic enhancement and polarization dependence of nonlinear upconversion emissions from single gold nanorod@ SiO_2 @ CaF_2: Yb^{3+}, Er^{3+} hybrid core–shell–satellite nanostructures. *Light Sci. Appl.* **2017**, *6*, e16217.

[A30] Bovero, E.; Van Veggel, F. C. Conformational Characterization of Eu^{3+}-Doped LaF_3 Core- Shell Nanoparticles through Luminescence Anisotropy Studies. *J. Phys. Chem. C* **2007**, *111*, 4529–4534.

[A31] Zhou, J.; Chen, G.; Wu, E.; Bi, G.; Wu, B.; Teng, Y.; Zhou, S.; Qiu, J. Ultrasensitive polarized up-conversion of Tm^{3+}–Yb^{3+} doped β-$NaYF_4$ single nanorod. *Nano Lett.* **2013**, *13*, 2241–2246.

[A32] Haro-Gonzalez, P.; Del Rosal, B.; Maestro, L.; Rodriguez, E. M.; Naccache, R.; Capobianco, J.; Dholakia, K.; Sole, J. G.; Jaque, D. Optical trapping of $NaYF_4$: Er^{3+}, Yb^{3+} upconverting fluorescent nanoparticles. *Nanoscale* **2013**, *5*, 12192–12199.

[A33] Rodríguez-Sevilla, P.; Rodríguez-Rodríguez, H.; Pedroni, M.; Speghini, A.; Bettinelli, M.; Solé, J. G.; Jaque, D.; Haro-González, P. Assessing single upconverting nanoparticle luminescence by optical tweezers. *Nano Lett.* **2015**, *15*, 5068–5074.

[A34] Li, Z.; Zhang, Y. An efficient and user-friendly method for the synthesis of hexagonal-phase $NaYF_4$: Yb, Er/Tm nanocrystals with controllable shape and upconversion fluorescence. *Nanotechnology* **2008**, *19*, 345606.

Graphical TOC Entry

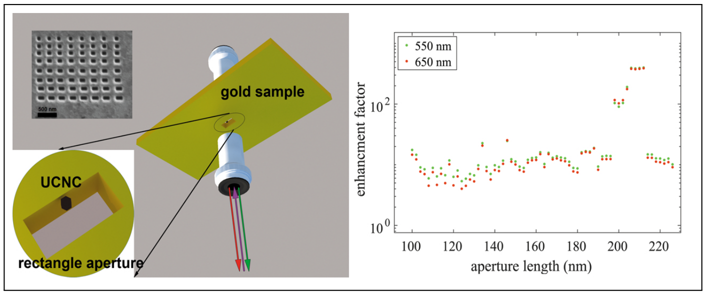

Title: Cascaded plasmon-enhanced emission from a single upconverting nanocrystal

Authors: Amirhossein Alizadehkhaledi, Adriaan L. Frencken, Mohsen Kamandar Dezfouli, Stephen Hughes, Frank C.J.M. van Veggel,and Reuven Gordon

Various rectangular apertures in gold film used for trapping a single UCNC. The upconversion emission is tuned by varying the rectangular aperture dimensions to obtain up to 400 times enhancement.

Supporting information for: Cascaded plasmon-enhanced emission from a single upconverting nanocrystal

Amirhossein Alizadehkhaledi,[†,‖] Adriaan L. Frencken,[‡,‖] Mohsen Kamandar Dezfouli,[¶] Stephen Hughes,[§] Frank C.J.M. van Veggel,[‡,‖] and Reuven Gordon[*,†,‖]

†*Department Electrical and Computer Engineering, University of Victoria, Victoria, British Columbia V8P 5C2, Canada*

‡*Department of Chemistry, University of Victoria, British Colombia V8W 3V6, Canada*

¶*Advanced Electronics and Photonics Research Centre, National Research Council Canada, 1200 Montreal Rd., Ottawa, ON K1A 0R6, Canada*

§*Department of Physics, Engineering Physics and Astronomy, Queen's University, Kingston, Ontario K7L 3N6, Canada*

‖*Centre for Advanced Materials & Related Technologies (CAMTEC), University of Victoria, Victoria, British Columbia V8W 2Y2, Canada*

E-mail: rgordon@uvic.ca

Phone: +1 250 472 5179 . Fax: +1 250 721 6052

Table of contents

Author Information

Corresponding Author

*E-mail (R. Gordon): rgordon@uvic.ca

ORCID

Reuven Gordon: 0000-0002-1485-6067

A-S1. Upconverting nanocrystals (UCNCs)

Transmission electron microscopy (TEM) was used to characterize the morphological and structural properties of the UCNCs. Figure A-S1(a),(b) show TEM images of UCNCs with 50 k and 250 k magnification respectively.

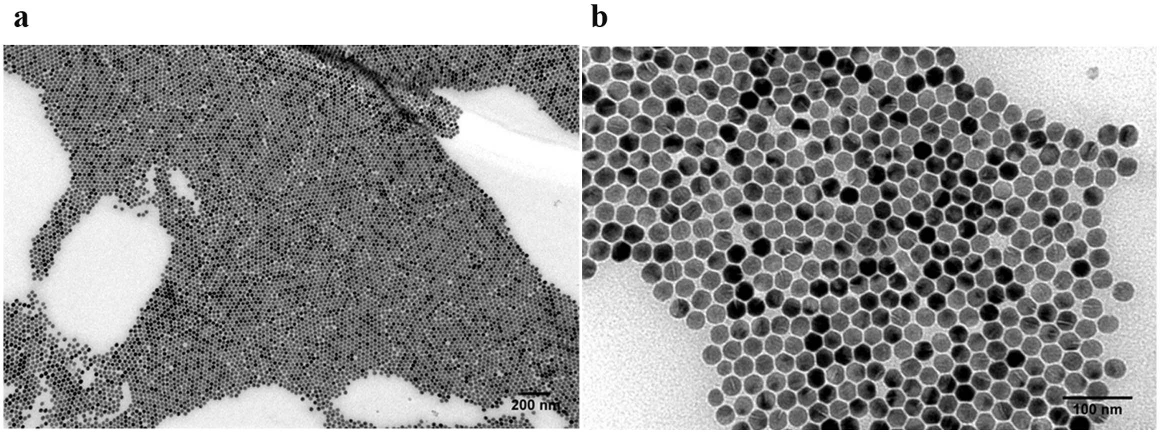

Figure A-S1: TEM images of $NaYF_4$: 2% Er nanoparticles magnified 50k times (a) and 250k times (b).

Figure A-S2 shows size analysis of UCNCs from the TEM images by measuring the surface area of at least 300 particles. The UCNCs mean diameter is 26.17 nm with standard deviation 2.65 nm.

Figure A-S3 shows an x-ray diffractogram of $NaYF_4$: 18 % Yb, 2% Er UCNCs comparing to a reference pattern of hexagonal $NaYF_4$.(A-S1)

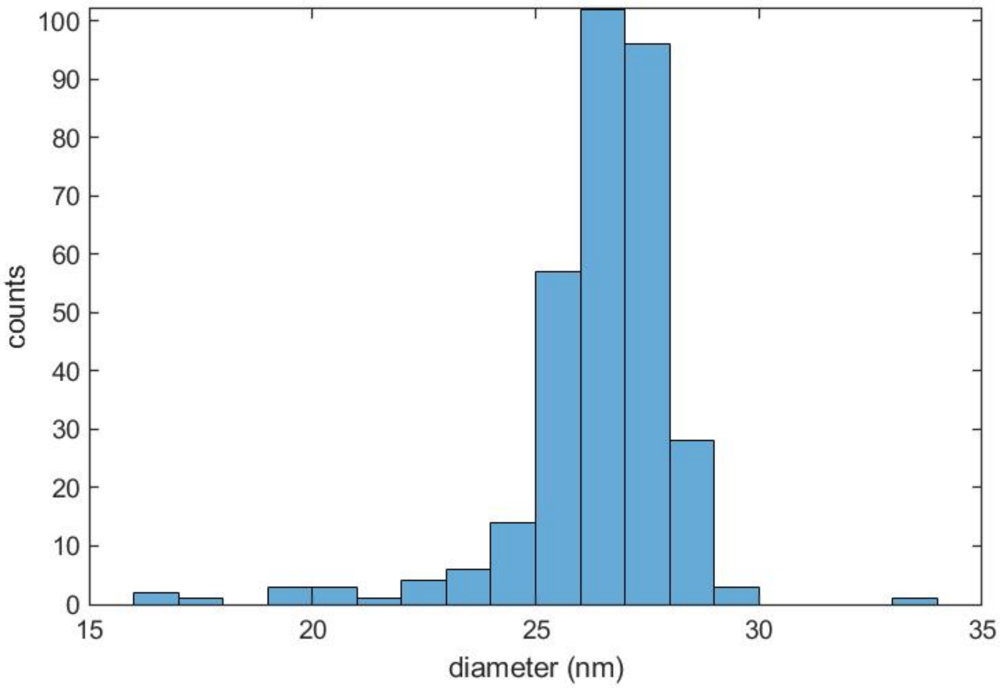

Figure A-S2: Size distribution of measured UCNCs.

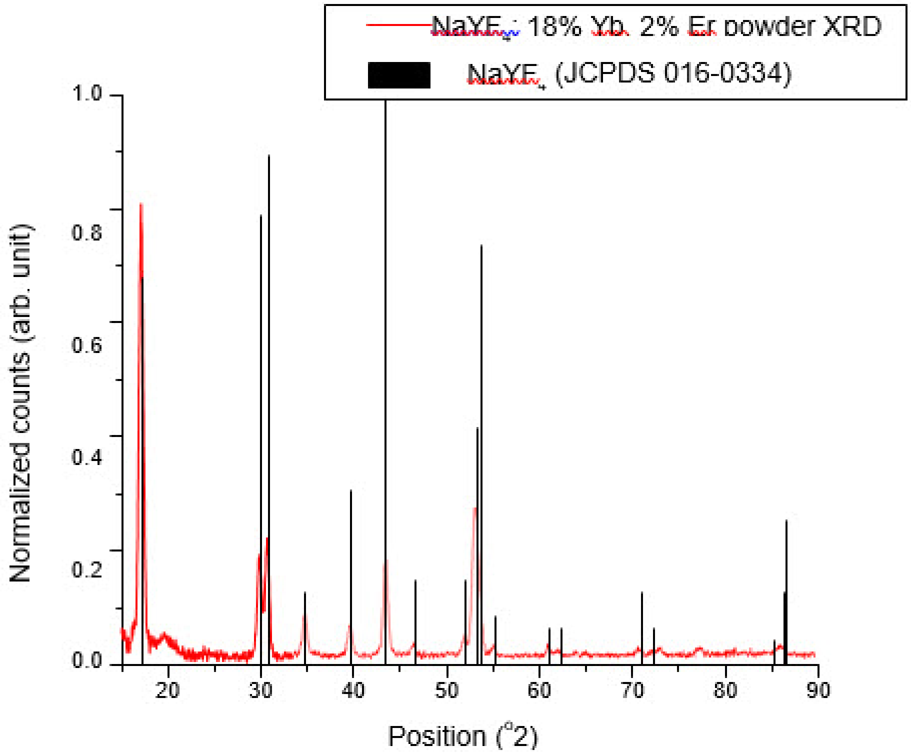

Figure A-S3: Experimental x-ray diffractogram of UCNCs and a reference pattern of hexagonal $NaYF_4$ (A-S1)

A-S2. Optical trapping setup

Figure A-S4 shows the schematic of optical trapping setup used for trapping UCNCs and detecting emission.

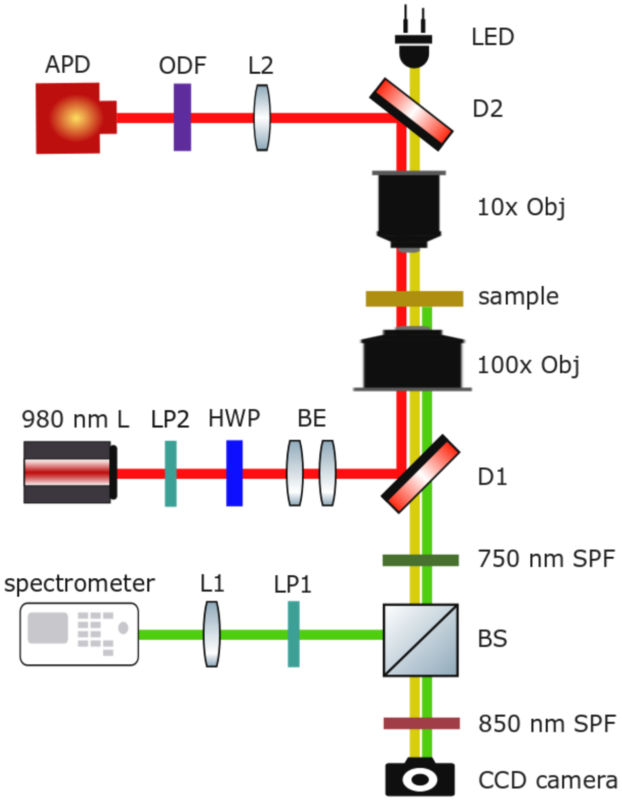

Figure A-S4: Schematic of the optical trapping setup. Abbreviations used: CCD camera = charge coupled device camera, SPF = short pass filter, BS= beam splitter, LP = linear polarizer, L=lens, D=dichroic mirror, HWP = half wave plate, BE = beam expander, 980 nm L=980 nm laser, Obj= objective lens ODF = optical density filter and APD = avalanche photodetector.

A-S3. Particle diffusion

Using the Stokes-Einstein equation, we estimate that the time for a 26 nm particle to diffuse to the trapping site in hexane for $3 \times 10^{10}/\text{cm}^3$ concentration is 140 ms. Figure A-S5 shows optical transmission through a 100 nm × 100 nm aperture for several trapping events in one second. Laser is turned on at time t = 0 s. Trapping occurred consistently within 0.01 s of turning on the laser. Figure A-S6 depicts the avalanche photodetector (APD) signal for the the first 0.1 s of the trapping event shown in Fig. A-S5.

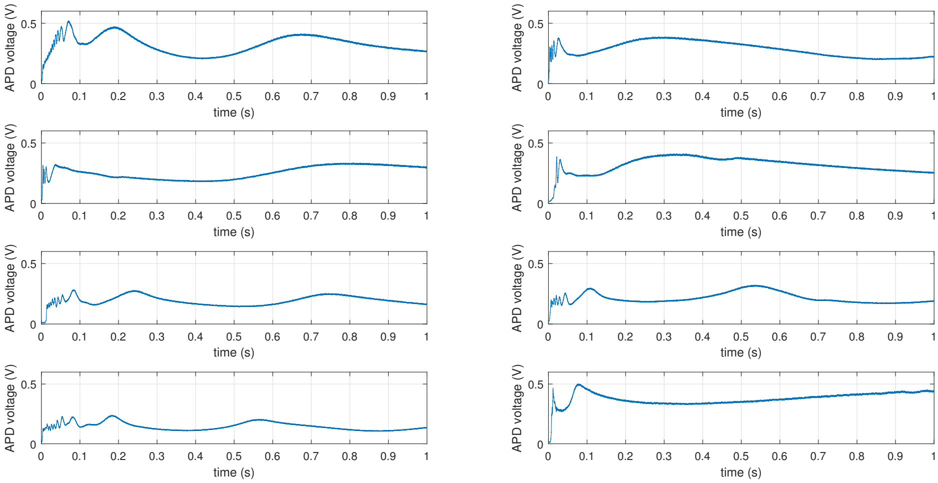

Figure A-S5: Optical transmission for several trapping events with one second interval (laser turned on at time zero).

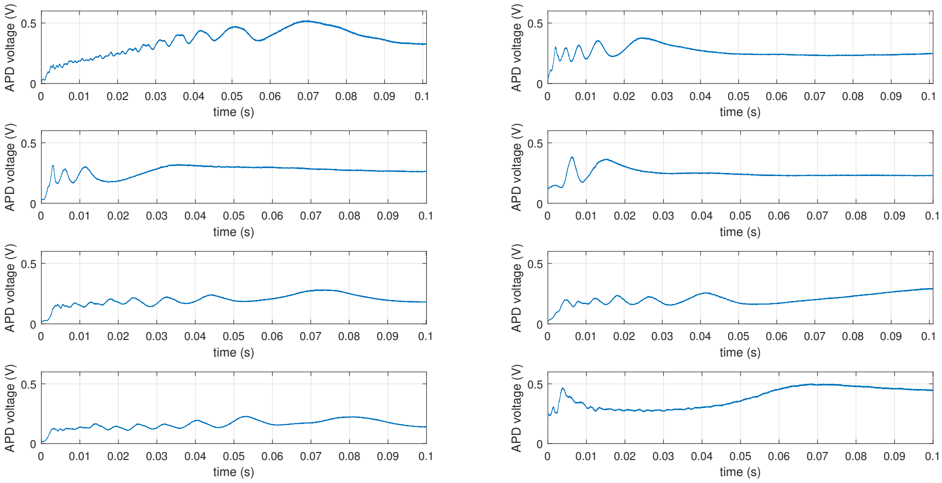

Figure A-S6: Optical transmission for several trapping events with 100 ms span (laser turned on at time zero).

A-S4. Single particle emission

Figure A-S7 shows upconversion emission for three different cases of single particle trapping, multiple particle trapping and no trapping, for the same aperture. When trapping multiple particles, the emission spectrum increases. To be sure that we measured a stable single particle emission, five separate emission spectrums were recorded from the sample from five separate trapping events. As we can see from Figure A-S8, all the measurements were approximately the same. The standard deviation of this measurement for 550 nm and 650 nm is 3.3 and 7.1 photons (3.1 % and 3.3 % normalized standard deviation).

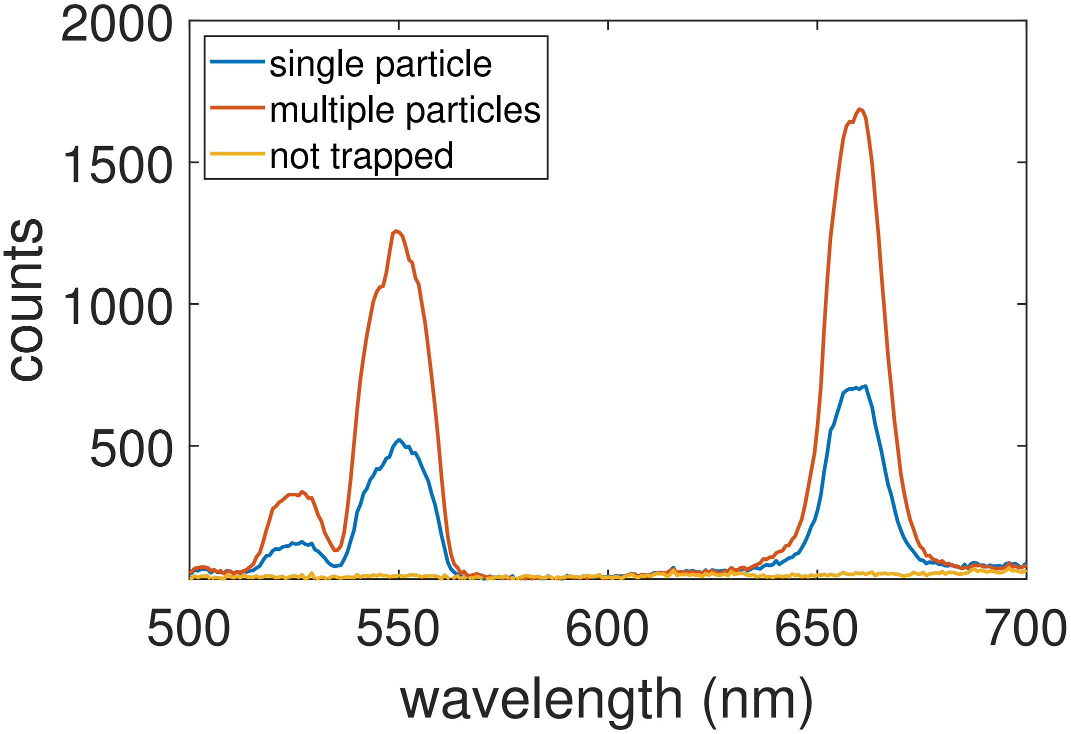

Figure A-S7: Luminescence emission spectrum from a single aperture for (blue) single particle trapping, (red) multiple particle trapping and (yellow) no particle trapping.

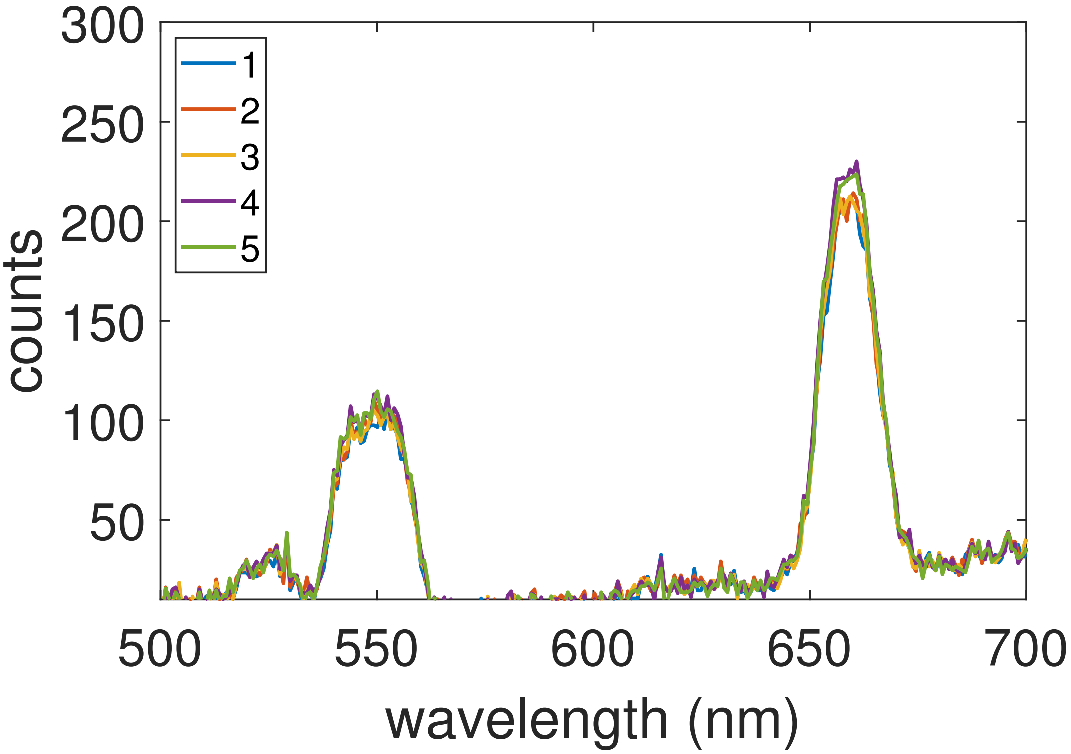

Figure A-S8: Luminescence emission spectrum from a single aperture for five different trapping events of single UCNCs.

A-S5. Power dependence

Figure A-S9 shows the 650 nm and 550 nm emission counts with varying the incident power. With high pumping power at 980 nm, the 650 nm and 550 nm increase linearly with the incident power. Since the incident power in this paper for all measurements is 30 mW, where we are in the linear regime.(A-S2)

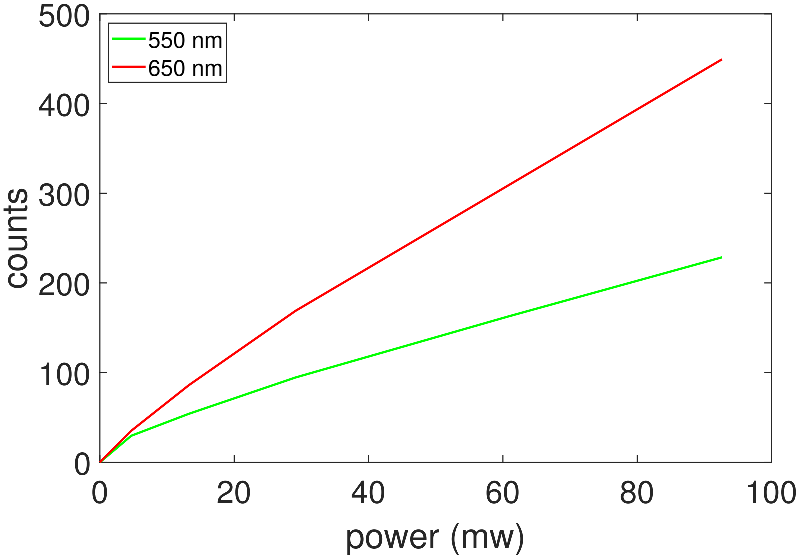

Figure A-S9: Upconversion emission of 650 nm and 550 nm when varying the incident power for 100 nm × 100 nm aperture.

A-S6. Emission ratio

Figure A-S10 shows the 650 nm to 550 nm emission ratio when varying the length of rectangular aperture from 100 nm to 226 nm in steps of 2 nm. The ratio between the 650 nm and 550 nm emission increases as the plasmonic enhancement increases. Figure A-S11 shows the 650 nm to 550 nm emission ratio with varying incident power.

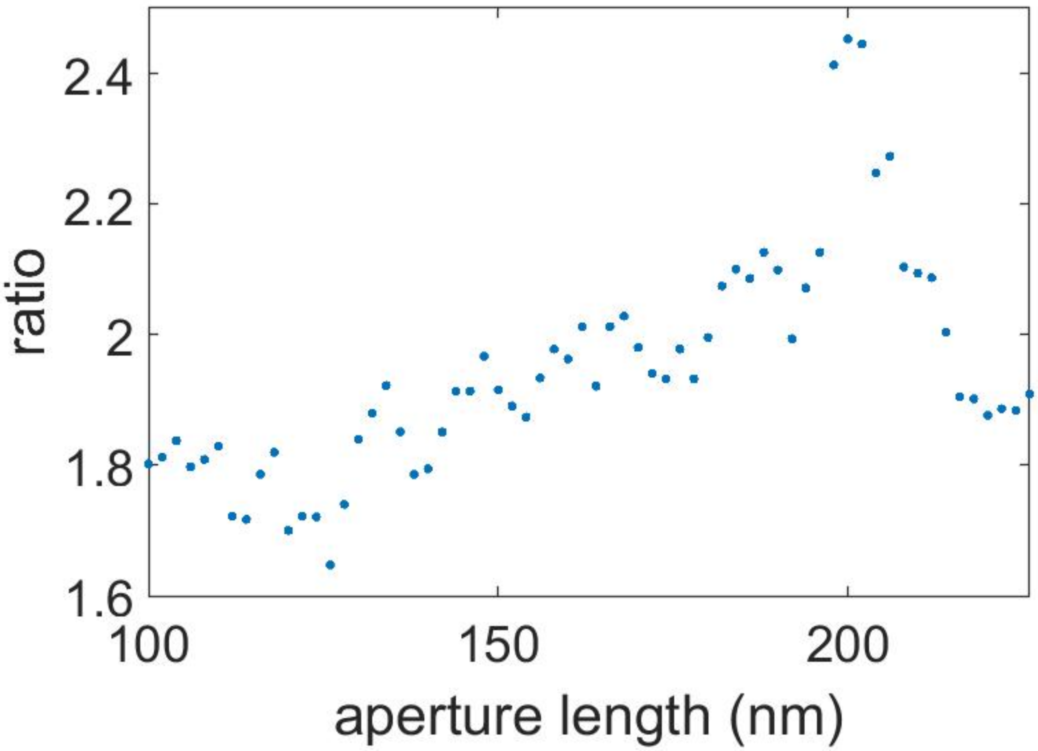

Figure A-S10: Upconversion ratio of 650 nm to 550 nm emission when varying the length of rectangular aperture from 100 nm to 226 nm.

As the pumping power at 980 nm increases, the 650 nm emission increases with respect to the 550 nm.

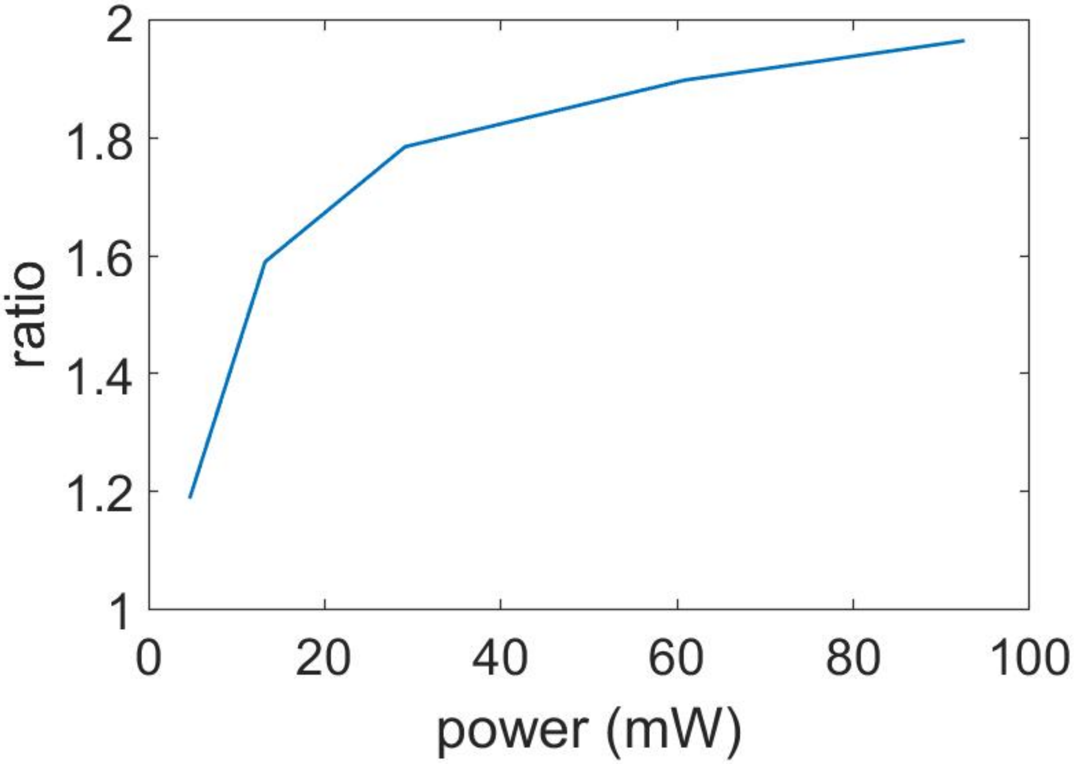

Figure A-S11: Upconversion ratio of 650 nm to 550 nm emission when varying the incident power for 100 nm × 100 nm aperture.

A-S7. Polarization dependence

Fig. 3 shows the polarization dependence of upconversion emission of a trapped UCNC for 550 nm and 650 nm. Data obtained is for the 210 nm by 100 nm aperture, integrated over a period of 20 s with an incident power of 30 mW. The emission at 650 nm is polarized along the short axis of the aperture (the same polarization as the incident pump), and the 550 nm emission is along the short axis. The fit shows a degree of polarization of 0.72 for 550 nm and 0.7 for 650 nm.

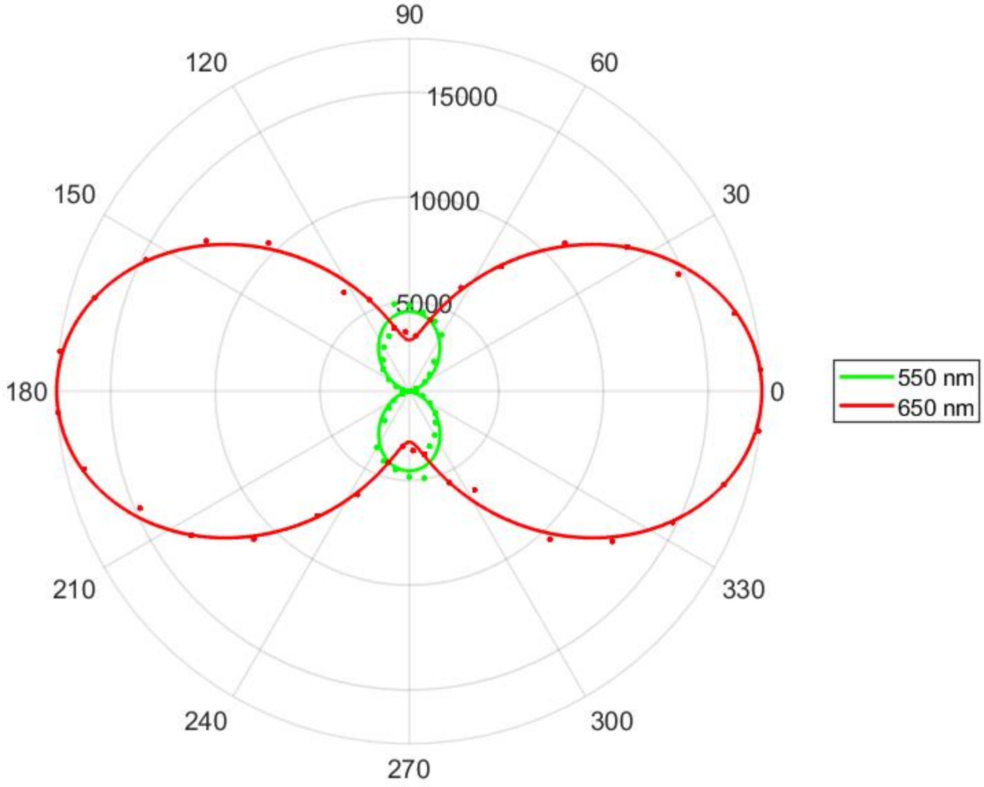

Figure A-S12: Polarization dependence of upconversion emission at 550 nm and 650 nm (counts). This data is for a single upconverting nanocrystal (26 nm diameter) trapped in a rectangular aperture.

References

[A-S1] Sobolev, B. P.; Mineev, D.; Pashutin, V. Low-temperature hexagonal modification of $NaYF_4$ having the gagarinite structure. Doklady Akademii Nauk. 1963; pp 791–794.

[A-S2] Piper, R. B.; Yoshida, M.; Farrell, D. J.; Khoury, T.; Crossley, M. J.; Schmidt, T. W.; Haque, S. A.; Ekins-Daukes, N. Kinetic insight into bimolecular upconversion: experiment and simulation. *Rsc Advances* **2014**, *4*, 8059–8063.

B Isolating Nanocrystals with an Individual Erbium Emitter: A Route to a Stable Single-Photon Source at 1550 nm Wavelength

(2019, Nano Letters)

Isolating Nanocrystals with an Individual Erbium Emitter: A Route to a Stable Single-Photon Source at 1550 nm Wavelength

Amirhossein Alizadehkhaledi,[†,¶] Adriaan L. Frencken,[‡,¶] Frank C.J.M. van Veggel,[‡,¶] and Reuven Gordon[*,†,¶]

†*Department Electrical and Computer Engineering, University of Victoria, Victoria, British Columbia V8W 2Y2, Canada*

‡*Department of Chemistry, University of Victoria, British Colombia V8W 2Y2, Canada*

¶*Centre for Advanced Materials & Related Technologies (CAMTEC), University of Victoria, Victoria, British Columbia V8W 2Y2, Canada*

E-mail: rgordon@uvic.ca

Phone: +1 250 472 5179 . Fax: +1 250 721 6052

Abstract

Single photon emitters based on individual atoms or individual atomic-like defects are highly sought-after components for future quantum technologies. A key challenge in this field is how to isolate just one such emitter; the best approaches still have an active emitter yield of only 50% so that deterministic integration of single active emitters is not yet possible. Here we demonstrate the ability to isolate individual erbium emitters embedded in 20 nm nanocrystals of $NaYF_4$ using plasmonic aperture optical tweezers. The optical tweezers capture

> the nanocrystal, while the plasmonic aperture enhances the emission of the Er and allow the measurement of discrete emission rate values corresponding to different numbers of erbium ions. Three separate synthesis runs show near-Poissonian distribution in the discrete levels of emission yield that correspond to the expected ion concentrations, indicating that the yield of active emitters is approximately 80%. Fortunately, the trap allows for selecting the nanocrystals with only a single emitter, and so this gives a route to isolating and integrating single emitters in a deterministic way. This demonstration is a promising step towards single photon quantum information technologies that utilize single ions in a solid-state medium, particularly because Er emits in the low-loss fiber-optic 1550 nm telecom band.

Intrigued by the promise of single-photon quantum technologies, there has been a concerted effort to make use of single atoms or atom-like defects as discrete emitters. Several works have investigated single lanthanide emitters in a crystal matrix (praseodymium,(B1)–(B4) cerium,(B5)–(B7) and erbium(B8),(B9)). The lanthanides provide stable emission that is protected from decoherence by shielding of the 4f electrons.(B10),(B11) They also have spin degrees of freedom that may be harnessed for additional control of the quantum state.(B7)

A major challenge remains of how to isolate only a single lanthanide emitter in a reliable way(B12),(B13) and to use these emitters in an approach that is potentially scalable. Past works relied on randomly searching among nanocrystals,(B2) or using low concentrations of implanted emitters.(B1) A further challenge, particularly for erbium which emits in the desired low-loss fiber optic C-band, is to enhance the emission rates so that single emitters can be isolated. One strategy to do this has been to surround the emitters with an optical cavity.(B9),(B14) A major drawback of all these approaches is that they rely on random distributions of emitters within the cavity, and several emitters are usually addressed in a single device by magnetic splitting.(B9)

Recognizing this drawback, researchers have very recently developed ion-trap implantation methods that can implant as few as 4 ions at a single spot in a crystal with 50 nm precision.(B15) The single spots show the signature of discrete emission levels; however, the emission yield is only 50%. About half of the implanted ions do not emit photons, so the overall yield is low. This is a particular drawback for photonic networks where several isolated ion emitters are desired on a single chip. Also, it is desirable to replace praseodymium with erbium for emission low loss optical fiber wavelengths.

Here we use plasmonic aperture optical tweezers as an alternative way to reliably isolate and effectively measure single erbium ion emitters in $NaYF_4$ nanocrystals. The plasmonic aperture solves two major problems: (1) it enhances the radiative rate so that single ions can be detected reliably in a short time at room temperature, and (2) it isolates the single Er containing nanocrystal from the other nanocrystals in solution. It should be noted that other works have seen enhanced single photon emission from nanoapertures in metals.(B16)

In a previous work that allowed us to make this step forward, we reported on the rectangular aperture optical tweezer to enhance the upconversion emission of Yb-Er doped $NaYF_4$ upconversion nanocrystals (UCNCs).(B17) In the aperture, the plasmonic enhancement was about 400× and the nanocrystals each contained approximately 2000 Erbium ions. Considering that we could detect emission for even the case of no plasmonic enhancement, that experiment opened the door for the important next step of detecting single Er ion emitters, as will be described in this work for the first time.

Figure B1 (a) shows a schematic of the plasmonic tweezer optical setup used and (b) shows a representative trapping event for a rectangular aperture of 208 nm by 100 nm in a 100 nm thick gold film. This aperture was chosen because it provided an enhancement of 410 for the 660 nm emission (see Supporting Information, SI).

The trapping event is detected by a jump in the avalanche photodiode voltage for the 980 nm trapping laser photons transmitted through the aperture. There are oscillations after the initial jump that we do not fully understand (it is suspected that they are the result of convective instabilities driven by the trapping event). Consistent with the diffusion time for the concentration of nanocrystals in hexane solution, the mean time to trap a nanocrystal was 50 ms.

It is important to emphasize the particular advantage of the plasmonic aperture tweezer: it allows for detecting a trapped nanocrystal even without emission. Thereby, even particles containing no emitters can be detected and their statistics recorded. This allows for conveniently rejecting those particles with zero active emitters, as well as those with more than one emitter, as will be described below. Also, trapping predominantly occurs for only a single particle at a time since the particles repel each other to allow for solution without aggregation; multiple particle trapping is extremely rare (less than 1%) and can be readily dismissed based on the trapping laser characteristic.(B17) Trapping of single upconverting nanoparticles can also be achieved by a single beam laser without the aperture.(B18) In that work, multiple nanocrystals could enter the trap because the trapping diameter was relatively large compared to the particle size (even considering particle repulsion). We do not see increases in intensity over time as they did in that work and therefore the number of emitters in the trap is not increasing (see Supporting Information).

We prepared $NaYF_4$ nanocrystals with trace doping of Er to probe the emission of zero, single and few emitters (see Methods section). Three separate solutions were synthesized, where the mean value of Er particles per nanocrystal was 0.006, 0.076 and 1.53 (referred to as λ for a Poisson distribution). Trapping was conducted on these separate solutions with 200 trapping events for each of the first two batches, and 100 trapping events for the third (since there were significantly more events with emitters in that third batch).

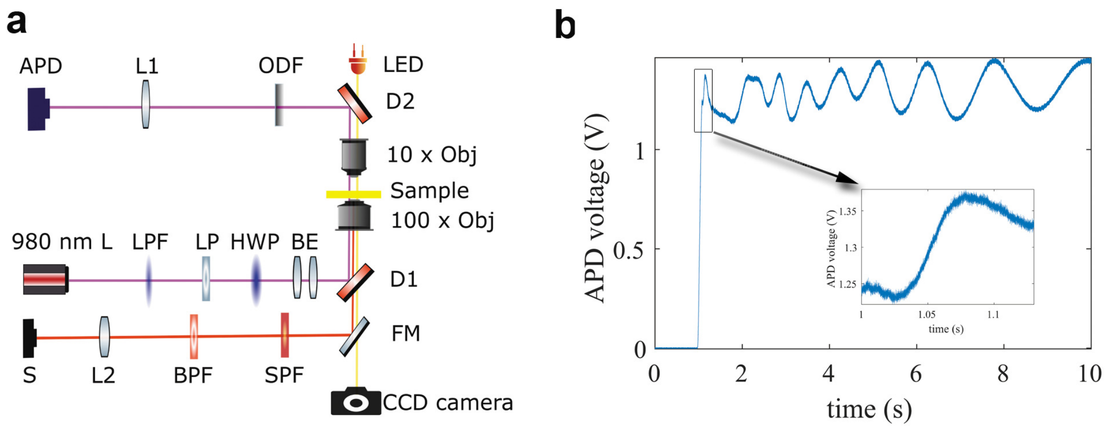

Figure B1: Optical trapping of nanocrystals containing trace Erbium concentration. (a) Schematic of optical trapping setup to allow for detection of Er containing nanocrystals down to a single Er emitter. Abbreviations used: CCD camera = charge coupled device camera, FM = flip mirror, SPF = short pass filter, BPF = band pass filter, LPF = long pass filter, LP = linear polarizer, L = lens, D = dichroic mirror, HWP = half wave plate, BE = beam expander, 980 nm L = 980 nm laser, Obj = objective lens, ODF = optical density filter and APD = avalanche photodetector. (b) Observed trapping event detected by a jump and oscillations in the transmitted 980 nm laser through the rectangular aperture.

Figure B2 (a) shows a schematic of the nanocrystals with zero to three emitters and their placement in the rectangular aperture, based on the location of the highest field intensity.(B17) Figure B2 (b) shows the upconverted emission around 660 nm from the $^4F_{9/2}$ to $^4I_{15/2}$ transition for individual trapping events of the 1.53 mean Er per nanocrystal batch (see SI for Er transitions). For a single trapping event (i.e., for one nanocrystal) the spectrum reliably gave the same number of counts with repeated measurement (see SI).

It is clear from this figure that the emission intensity falls within discrete levels, which we attribute to zero, one, two three, five and six Er emitters. The 0.006 mean Erbium batch showed 199 events without any emission, and just a single event with emission (see SI). The 0.076 mean Er batch showed 190 events without any emission and 9 with a single Erbium emitter (see SI). As expected, emission was also observed for the $^4S_{3/2}$ to $^4I_{15/2}$ transition at 550 nm (see SI).

Figure B3 shows the counts for the 1.53 mean Erbium count per particle sample for

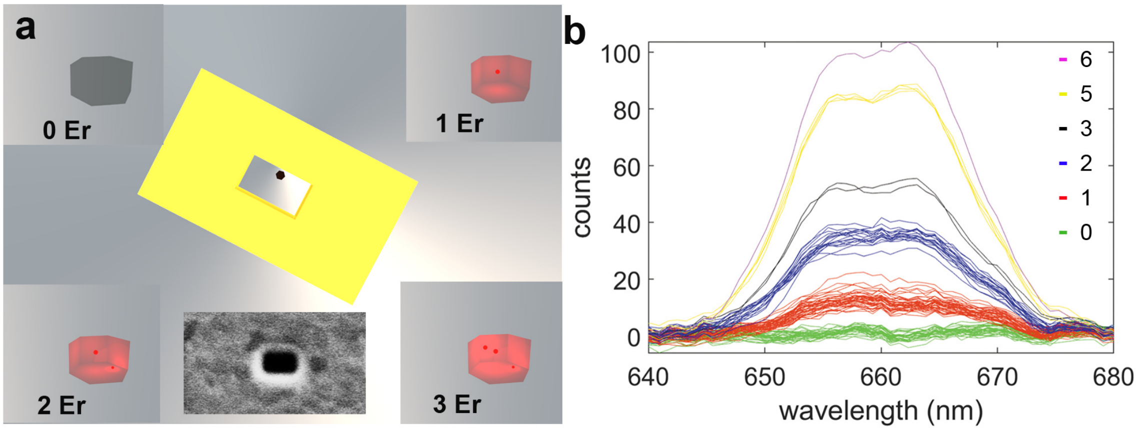

Figure B2: Discrete emitters in trapped $NaYF_4$ nanocrystals with trace Er defects. (a) Schematic of various nanocrystals with 0-3 Er ions present. Also depicted is the placement of the nanocrystal in the rectangular aperture plasmonic tweezer. 208 nm×100 nm rectangular aperture focused ion beam image. (b) Observed emission spectra for sample containing a mean number of 1.53 Er ions per nanocrystal particle. Discrete levels in the upconverted emission are observed corresponding to 0, 1, 2, 3, 5, 6 Er emitters.

100 trapping events. Also shown is the expected Poisson distribution of the number of Er ions in each particle assuming that each Er can emit.The Er^{3+} ions can be expected to be statistically distributed due to their chemical similarity to $Y3+$and the near identical effective radii of the ions (90 pm for Y^{3+} and 89 pm for Er^{3+} (B19)). While the observed distribution and the expected distribution are similar, the mean number of Er emitters was 1.11 per particle in the experiment whereas 1.53 was expected if all of the Er ions could emit. Similar results are found for the other batches, as presented in Table 1.

A possible explanation for the experiments yielding lower than expected Er emitters is that some of the emitters within the particle are quenched by being close to the surface which can reduce the emission by two orders of magnitude.(B20),(B21) A simple analysis based on the volume of the particle and the volume of surface quenching layer (thickness of 1 nm) suggests that 25 % of the Er emitters are quenched. This is very close to the observed values considering statistical uncertainty, and so it appears to be a plausible explanation (see Table 1). We believe that it is possible then

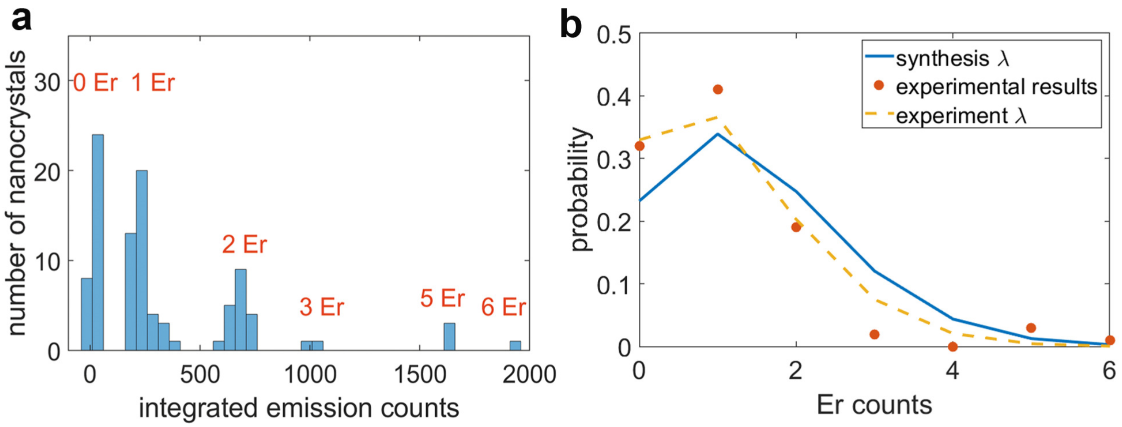

Figure B3: Statistics of emitters observed in experiment. (a) Histogram of integrated emission counts for 100 trapping events. (b) Probability of having 0 to 6 Er emitters based on experimental measurements (part (a)) and using a Poisson distribution using expected synthesis statistics having a mean Er count of 1.53 per particle and calculated experiment statics with mean Er count of 1.11 (see SI)

avoid quenching by creating core-shell nanocrystals, where the shell has no Erbium content.(B22)

A simple calculation shows that the average distance between two, three, four and five Er ions are 14, 12, 11 and 10 nm (see SI). In this range of average distances, we expect negligible energy transfer and so this process is unlikely.(B23),(B24)

Even though the yield of active emitters in the nanoparticles is less than 100%, the plasmonic tweezer allows for isolating individual particles and determining which ones have a single active (not-quenched) emitter. Therefore, if we use the optical tweezer to separate these particles (perhaps by fixing them to the surface with an attaching ligand or translating them with a fiber-based tweezer,(B25) or separating them through a nanopore(B26)) we can reliably and scalably obtain single emitters. Another intriguing possibility presented by this work is to obtain a nanoscrystal with only two emitters, for studying possible quantum interactions.

In summary, we have demonstrated the isolation of $NaYF_4$ nanocrystals with single active Er emitters, as well as those with a few emitters and zero emitters. The number of active Er emitters is determined by discrete levels in the upconversion

Table 1: Distribution of synthesis and experiment λ values for three separate batches. Standard error is presented for experiment.

Er/Y Molar Ratio	Synthesis λ	Experiment λ	Experiment λ / Synthesis λ
0.98 μ%	0.00609	0.005±0.0003	0.82±0.06
19.59 μ%	0.07573	0.065±0.005	0.86±0.06
195.90 μ%	1.53	1.11±0.11	0.73±0.07

emission counts. The plasmonic aperture serves the dual purpose of isolating the individual nanocrystals and enhancing the emission such that even single emitters can be easily detected within the experimental sensitivity. In the future, it will be interesting to probe the single photon statistics of this system, possibly by coupling directly to an optical fiber to achieve single telecom-wavelength photons in fiber.(B25),(B27) We did some preliminary measurements showing telecom-wavelength emission from the ensemble of these emitters, however our present setup does not have the required sensitivity in this range (see SI). It would also be of interest to use this setup for purification and translocation of single or two-emitter particles. For quantum applications such as quantum computing using linear optics, the indistinguishably of the emitters should also be probed.(B28)–(B30)

Methods

UCNCs synthesis and characterization

Chemicals

Yttrium(III) chloride hexahydrate (99.99%), ytterbium(III) chloride (99.998%), erbium(III) chloride hexahydrate (99.995%), ammonium fluoride (99.99%), tech grade oleic acid (90%), tech grade 1-octadecene (90%), and hexanes were purchased from Sigma-Aldrich. Anhydrous ethanol from Commercial Alcohols, methanol from Caledon, and sodium hydroxide from Bio Basic Canada inc. were used. All chemicals were used as received.

Synthesis

Erbium oleate was prepared by adding 1 mmol $ErCl_3{\cdot}(H_2O)_6$) to a mixture of 15 mL 1-octadecene and 6 mL oleic acid. The mixture was heated to 160°C under vacuum (estimated to be 0.0 inch Hg) and kept at that temperature for 30 minutes before cooling to room temperature. For $NaYF_4$ doped with 0.98 μ% Er molar ratio, in a 100 mL three-neck round-bottom flask, 1 mmol $YCl_3{\cdot}(H_2O)_6$ and 1 mL $0.1{\times}10^{-6}$ mM $ErCl_3{\cdot}(H_2O)_6$ in 1-octadecene are added to 14 mL 1-octadecene and 6 mL oleic acid. For $NaYF_4$ doped with 19.59 μ% Er molar ratio, in a 100 mL three-neck round-bottom flask, 1 mmol $YCl_3{\cdot}(H_2O)_6$ and 20 μL $0.1{\times}10^{-3}$ mM $ErCl_3{\cdot}(H_2O)_6$ in 1-octadecene are added to 15 mL 1-octadecene and 6 mL oleic acid. For $NaYF_4$ doped with 195.90 μ% Er molar ratio, in a 100 mL three-neck round-bottom flask, 1 mmol $YCl_3{\cdot}(H_2O)_6$ and 200 μL $0.1{\times}10^{-3}$ mM $ErCl_3{\cdot}(H_2O)_6$ in 1-octadecene are added to 15 mL 1-octadecene and 6 mL oleic acid. The mixture was heated to 150°C under vacuum and kept at that temperature for 30 minutes before cooling to room temperature. Once cooled, a solution of 100 mg sodium hydroxide and 148 mg ammonium fluoride in 10 mL methanol is added dropwise while stirring. The mixture was heated to 70°C for 60 minutes to evaporate the methanol. The mixture was put under a blanket of argon and the temperature was raised to 300°C over 15 minutes. The temperature was kept at 300°C for 60 minutes, briefly spiking to 319°C. The reaction mixture was then cooled, washed with 20 mL ethanol, centrifuged at 1800 G for 10 min, and washed with 20 mL ethanol again before dispersing the particles in 20 mL hexane. Er-Yb co-doped $NaYF_4$ synthesized as reported before.(B17)

UCNCs Characterization

Transmission electron microscopy images were obtained using a JEOL JEM-1400 microscope operating at 80 kV. Hexane dispersions of the UCNCs were drop-cast on a Formvar carbon-coated grid (300 mesh Cu) and air-dried before imaging. Size analysis of UCNCs from the images was performed by measuring the surface area of at least 1000 particles and calculating the corresponding diameter using ImageJ 1.51. X-ray diffractograms with a resolution of 0.0263° 2θ were collected using a PANalytical Empyrean X-ray System with a Cu source (Kα radiation, λ= 1.54060 Å) operating at 45 kV and 40 mA. See SI for additional data.

Fabrication of rectangular aperture

The rectangular apertures were fabricated by focused ion beam milling (Hitachi FB-2100) of a commercially available slide with a 100 nm gold layer on a glass substrate (EMF Corp.) and a 5 nm Ti adhesion layer.

Optical trapping

A continuous wave 980 nm single-beam laser was filtered (780 nm long pass filter), collimated, expanded, and focused onto the sample using a 100× oil immersion microscope objective (1.25 numerical aperture). This beam serves both as trapping beam and the excitation source for UCNCs. A 10× condenser microscopic objective (0.25 numerical aperture) was used to collect the transmitted signal through the rectangle aperture and was measured by a silicon-based avalanche photodetector (Thorlabs APD110A). A piezoelectric controlled 3-axis sample stage was used to aligned the beam through the rectangle apertures with 20 nm positioning precision. A half-wave plate (HWP) and linear polarizer (LP) were used to orient the polarization of the pump beam. Measurements were obtained after altering the HWP and LP orientation for obtaining the highest transmission of laser beam through the aperture (the incident laser is made to be always linearly polarized along the short axes of the aperture). A 750 nm short pass filter (Thorlabs FES0750) and a 500-700 nm band pass filter were used on spectrometer to minimize the trapping beam intensity. The luminescence spectrum was measured using a QE65000 Ocean Optics spectrometer for 30 S integration time. All 500 upconversion measurements for three different batches were conducted using 39 mW focused on approximately 1μm^2. The rectangular aperture gold sample were attached to a cover slips with a free spacer contain 10μL UCNCs with concentration of $2 \times 10^{10} particles/cm^3$ in hexane.

Acknowledgement

The authors acknowledge funding support from the NSERC CREATE program Materials for Enhanced Energy Technologies (MEET) and the NSERC Discovery Grants program.

Supporting Information Available

UCNCs TEM images, UCNCs size distribution, UCNCs x-ray diffraction, Emission enhancement factor of rectangle aperture, emission statistics for different concentrations, emission stability, multiple trapping, emission at 550 nm, emission at 1550 nm and Er-Er distance calculation

Competing interests

The authors declare that there are no competing interests.

Corresponding Author

Reuven Gordon is the corresponding author. (rgordon@uvic.ca)

References

[B1] Kolesov, R.; Xia, K.; Reuter, R.; Stöhr, R.; Zappe, A.; Meijer, J.; Hemmer, P.; Wrachtrup, J. Optical detection of a single rare-earth ion in a crystal. *Nat. Commun.* **2012**, *3*.

[B2] Utikal, T.; Eichhammer, E.; Petersen, L.; Renn, A.; Götzinger, S.; Sandoghdar, V. Spectroscopic detection and state preparation of a single praseodymium ion in a crystal. *Nat. Commun.* **2014**, *5*, 3627.

[B3] Nakamura, I.; Yoshihiro, T.; Inagawa, H.; Fujiyoshi, S.; Matsushita, M. Spectroscopy of single Pr^{3+} ion in LaF_3 crystal at 1.5 K. *Sci. Rep.* **2014**, *4*, 7364.

[B4] Eichhammer, E.; Utikal, T.; Götzinger, S.; Sandoghdar, V. Spectroscopic detection of single Pr^{3+} ions on the $^3H_4 -^1 D_2$ transition. *New J. Phys.* **2015**, *17*, 083018.

[B5] Kolesov, R.; Xia, K.; Reuter, R.; Jamali, M.; Stöhr, R.; Inal, T.; Siyushev, P.; Wrachtrup, J. Mapping spin coherence of a single rare-earth ion in a crystal onto a single photon polarization state. *Phys. Rev. Lett.* **2013**, *111*, 120502.

[B6] Siyushev, P.; Xia, K.; Reuter, R.; Jamali, M.; Zhao, N.; Yang, N.; Duan, C.; Kukharchyk, N.; Wieck, A.; Kolesov, R.; Wrachtrup, J. Coherent properties of single rare-earth spin qubits. *Nat. Commun.* **2014**, *5*, 3895.

[B7] Xia, K.; Kolesov, R.; Wang, Y.; Siyushev, P.; Reuter, R.; Kornher, T.; Kukharchyk, N.; Wieck, A. D.; Villa, B.; Yang, S.; Wrachtrup, J. All-optical preparation of coherent dark states of a single rare earth ion spin in a crystal. *Phys. Rev. Lett.* **2015**, *115*, 093602.

[B8] Yin, C.; Rancic, M.; de Boo, G. G.; Stavrias, N.; McCallum, J. C.; Sellars, M. J.; Rogge, S. Optical addressing of an individual erbium ion in silicon. *Nature* **2013**, *497*, 91.

[B9] Dibos, A.; Raha, M.; Phenicie, C.; Thompson, J. D. Atomic source of single photons in the telecom band. *Phys. Rev. Lett.* **2018**, *120*, 243601.

[B10] Bünzli, J.-C. G.; Piguet, C. Taking advantage of luminescent lanthanide ions. *Chem. Soc. Rev.* **2005**, *34*, 1048-1077.

[B11] Hughes, I.; Däne, M.; Ernst, A.; Hergert, W.; Lüders, M.; Poulter, J.; Staunton, J.; Svane, A.; Szotek, Z.; Temmerman, W. Lanthanide contraction and magnetism in the heavy rare earth elements. *Nature* **2007**, *446*, 650.

[B12] O'Brien, C.; Zhong, T.; Faraon, A.; Simon, C. Nondestructive photon detection using a single rare-earth ion coupled to a photonic cavity. *Phys. Rev. A* **2016**, *94*, 043807.

[B13] Lopez, C.; Trimeche, A.; Comparat, D.; Picard, Y. Real-Time Trajectory Control of Deterministically Produced Ions. *Phys. Rev. Appl.* **2019**, *11*, 064049.

[B14] Zhong, T.; Kindem, J. M.; Bartholomew, J. G.; Rochman, J.; Craiciu, I.; Verma, V.; Nam, S. W.; Marsili, F.; Shaw, M. D.; Beyer, A. D.; Faraon, A. Optically addressing single rare-earth ions in a nanophotonic cavity. *Phys. Rev. Lett.* **2018**, *121*, 183603.

[B15] Groot-Berning, K.; Kornher, T.; Jacob, G.; Stopp, F.; Dawkins, S. T.; Kolesov, R.; Wrachtrup, J.; Singer, K.; Schmidt-Kaler, F. Deterministic single ion implantation of rare-earth ions for nanometer resolution colour center generation. *Phys. Rev. Lett.* **2019**, *123*, 106802.

[B16] Choy, J. T.; Hausmann, B. J.; Babinec, T. M.; Bulu, I.; Khan, M.; Maletinsky, P.; Yacoby, A.; Lončar, M. Enhanced single-photon emission from a diamondsilver aperture. *Nat. Photonics* **2011**, *5*, 738.

[B17] Alizadehkhaledi, A.; Frencken, A. L.; Dezfouli, M. K.; Hughes, S.; van Veggel, F. C. J. M.; Gordon, R. Cascaded plasmon-enhanced emission from a single upconverting nanocrystal. *ACS Photonics* **2019**, *6*, 1125-1131.

[B18] Rodríguez-Sevilla, P.; Rodríguez-Rodríguez, H.; Pedroni, M.; Speghini, A.; Bettinelli, M.; Solé, J. G.; Jaque, D.; Haro-González, P. Assessing single upconverting nanoparticle luminescence by optical tweezers. *Nano Lett.* **2015**, *15*, 5068-5074.

[B19] Shannon, R. D. Revised effective ionic radii and systematic studies of interatomic distances in halides and chalcogenides. *Acta Crystallogr. A* **1976**, *32*, 751-767.

[B20] Wang, F.; Wang, J.; Liu, X. Direct evidence of a surface quenching effect on size-dependent luminescence of upconversion nanoparticles. *Angew. Chem.* **2010**, *49*, 7456-7460.

[B21] Wang, Y.; Tu, L.; Zhao, J.; Sun, Y.; Kong, X.; Zhang, H. Upconversion luminescence of β-NaYF$_4$: Yb^{3+}, Er^{3+}@ β-NaYF$_4$ core/shell nanoparticles: excitation power density and surface dependence. *J. Phys. Chem. C* **2009**, *113*, 7164-7169.

[B22] Yi, G.-S.; Chow, G.-M. Water-soluble NaYF$_4$: Yb, Er (Tm)/NaYF$_4$/polymer core/shell/shell nanoparticles with significant enhancement of upconversion fluorescence. *Chem. Mater.* **2007**, *19*, 341-343.

[B23] Fischer, S.; Johnson, N. J.; Pichaandi, J.; Goldschmidt, J. C.; van Veggel, F. C. J. M. Upconverting core-shell nanocrystals with high quantum yield under low irradiance: On the role of isotropic and thick shells. *J. Appl. Phys.* **2015**, *118*, 193105.

[B24] Okamoto, E.; Sekita, M.; Masui, H. Energy transfer between Er^{3+} ions in LaF_3. *Phys. Rev. B* **1975**, *11*, 5103.

[B25] Berthelot, J.; Aćimović, S.; Juan, M.; Kreuzer, M.; Renger, J.; Quidant, R. Three-dimensional manipulation with scanning near-field optical nanotweezers. *Nat. Nanotechnol.* **2014**, *9*, 295.

[B26] Verschueren, D.; Shi, X.; Dekker, C. Nano-Optical Tweezing of Single Proteins in Plasmonic Nanopores. *Small Methods* **2019**, *3*, 1800465.

[B27] Covey, J. P.; Sipahigil, A.; Szoke, S.; Sinclair, N.; Endres, M.; Painter, O. Telecom-band quantum optics with ytterbium atoms and silicon nanophotonics. *Phys. Rev. Appl.* **2019**, *11*, 034044.

[B28] Knill, E.; Laflamme, R.; Milburn, G. J. A scheme for efficient quantum computation with linear optics. *Nature* **2001**, *409*, 46.

[B29] Asadi, F. K.; Lauk, N.; Wein, S.; Sinclair, N.; O'Brien, C.; Simon, C. Quantum repeaters with individual rare-earth ions at telecommunication wavelengths. *Quantum* **2018**, *2*, 93.

[B30] Duan, L.-M.; Lukin, M.; Cirac, J. I.; Zoller, P. Long-distance quantum communication with atomic ensembles and linear optics. *Nature* **2001**, *414*, 413.

Graphical TOC Entry

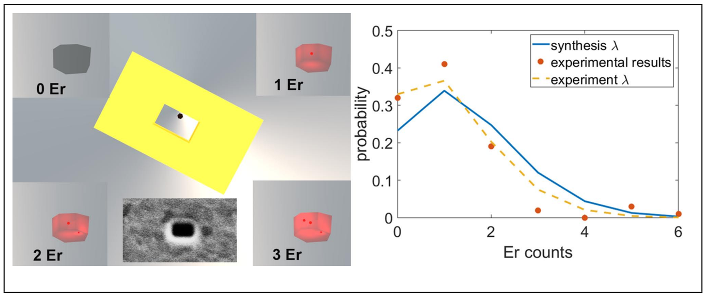

Title: Isolating Nanocrystals with an Individual Erbium Emitter: A Route to a Stable Single-Photon Source at 1550 nm Wavelength

Authors: Amirhossein Alizadehkhaledi, Adriaan L. Frencken, Frank C.J.M. van Veggel,and Reuven Gordon

Trapped upconversion nanocrystal in the rectangular aperture plasmonic tweezer containing 0-3 Er ions . Probability of having 0 to 6 Er emitters based on experimental measurements and using a Poisson distribution with expected synthesis statistics and calculated experiment statics.

Supporting Information for
Isolating Nanocrystals with an Individual Erbium Emitter: A Route to a Stable Single-Photon Source at 1550 nm Wavelength

Amirhossein Alizadehkhaledi,[†,¶] Adriaan L. Frencken,[‡,¶] Frank C.J.M. van Veggel,[‡,¶] and Reuven Gordon[*,†,¶]

†*Department Electrical and Computer Engineering, University of Victoria, Victoria, British Columbia V8W 2Y2, Canada*

‡*Department of Chemistry, University of Victoria, British Colombia V8W 2Y2, Canada*

¶*Centre for Advanced Materials & Related Technologies (CAMTEC), University of Victoria, Victoria, British Columbia V8W 2Y2, Canada*

E-mail: rgordon@uvic.ca

Phone: +1 250 472 5179 . Fax: +1 250 721 6052

Author Information

Corresponding Author

*E-mail (R. Gordon): rgordon@uvic.ca

ORCID

Reuven Gordon: 0000-0002-1485-6067

A. Upconverting nanocrystals (UCNCs)

Transmission electron microscopy (TEM) was used to characterize the morphological and structural properties of the UCNCs. Figures B-S1, B-S2 and B-S3 show TEM and size distribution of different UCNCs sample with 1.53, 0.076, 0.006 Er per particle. Figure B-S4 shows experimental x-ray diffractogram of UCNCs and a reference pattern of hexagonal $NaYF_4$.

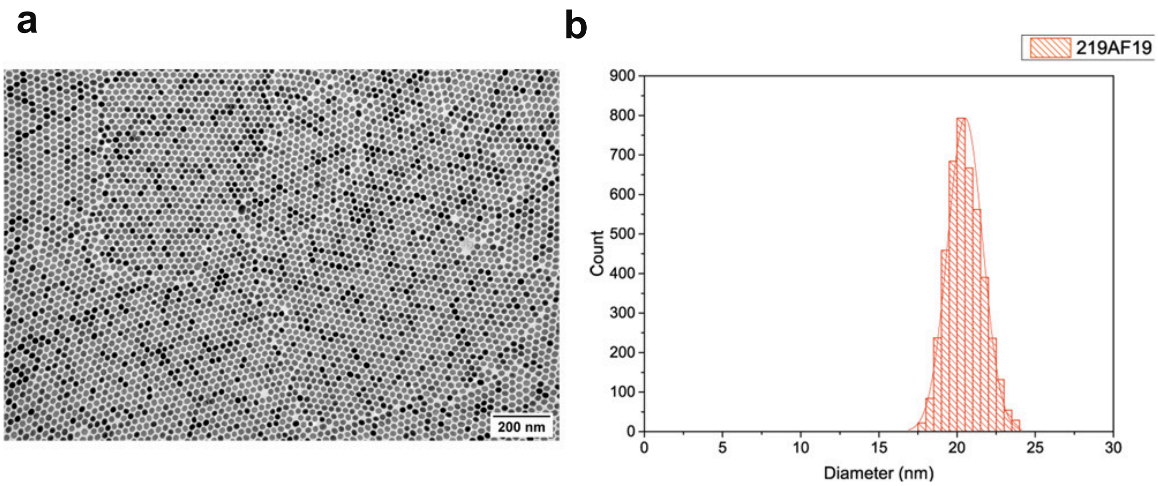

Figure B-S1: Size distribution of measured $NaYF_4$: Er UCNCs (~0.006 Er / NP) with a mean diameter of 20.52 nm and standard deviation 1.12 nm.

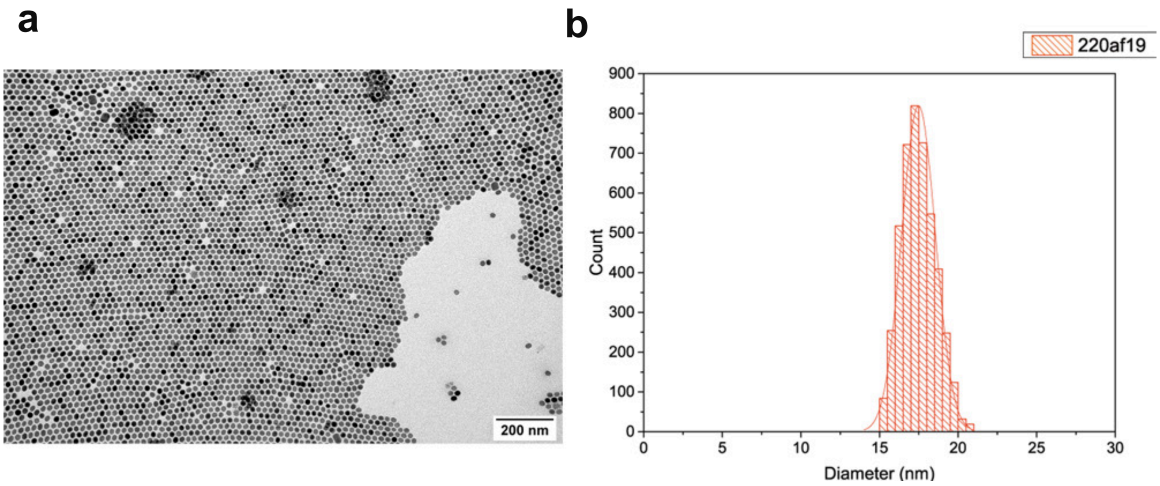

Figure B-S2: Size distribution of measured $NaYF_4$: Er UCNCs (~0.076 Er / NP) with a mean diameter of 17.49 nm and standard deviation 1.08 nm

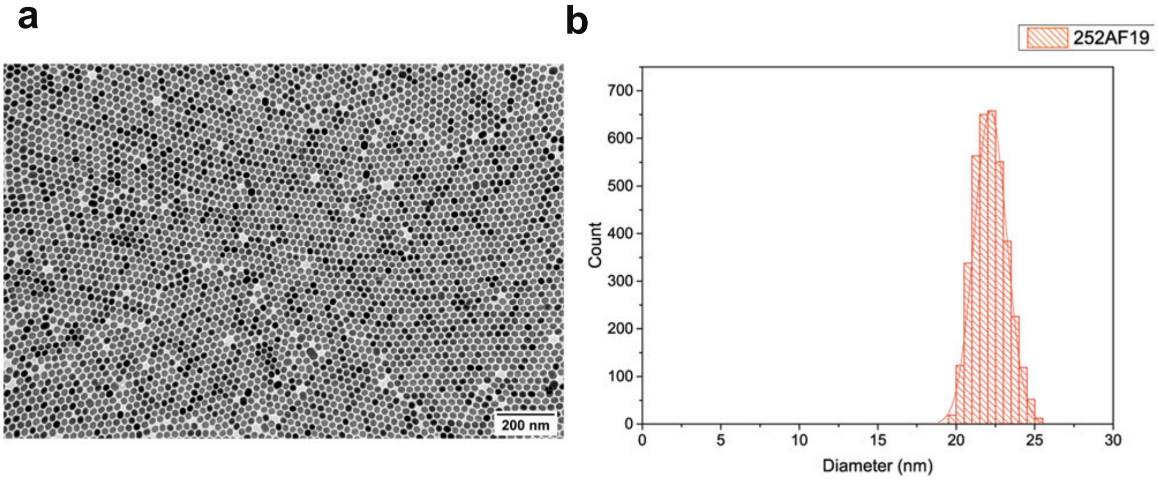

Figure B-S3: : Size distribution of measured NaYF$_4$: Er UCNCs (∼1.5 Er / NP) with a mean diameter of 22.17 nm and standard deviation 1.03 nm.

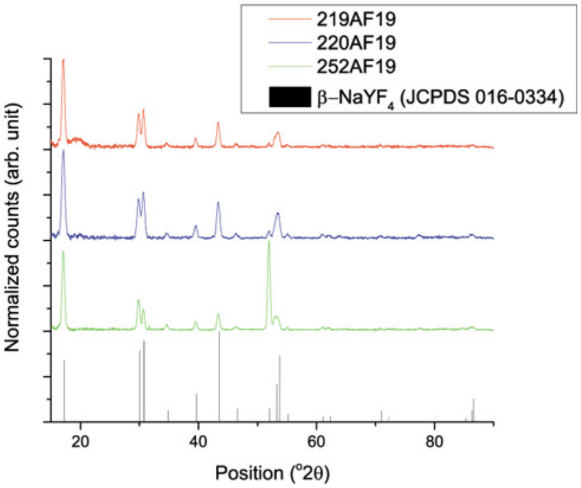

Figure B-S4: Experimental x-ray diffractogram of UCNCs and a reference pattern of hexagonal NaYF$_4$$^{\text{(B-S1)}}$

B. Erbium energy diagram

Figure B-S5 shows Erbium energy diagram. 980 nm, 660 nm, 550 nm, 520 nm transitions depicted by purple, red, light green and dark green solid arrows. Dashed lines show non-radiative transitions.

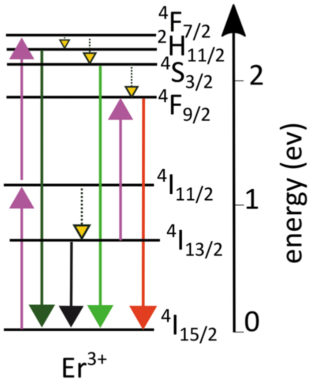

Figure B-S5: Erbium energy diagram

C. Enhancement factor

To calculate the enhancement factor, we used the same measurement as reported before.(B-S2) A single 18% Yb and 2% Er codoped NayF$_4$ UCNC was trapped, and compared to free solution with 1000 higher concentration. The enhancement factor was 410 for 650 nm transitions for the aperture used.

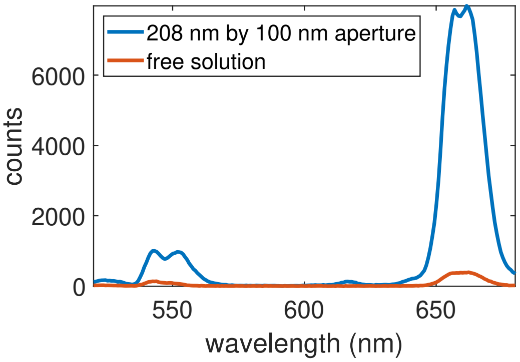

Figure B-S6: Upconversion emission spectra for UCNCs in free solution (red) at 1000 times higher concentration than UCNC emission of single particle in 208 nm × 100 nm aperture (blue).

D. Stability

To be sure that we measured a stable single particle emission, five emission spectra were recorded in a row from the sample. As we can see from Figure B-S7, all the measurements show approximately the same emission level. Figure B-S8 shows the trapping of two particles. The first trapping happens instantly at 2 s when the laser is switched on, and after some oscillation, the level of voltage becomes stable around 0.33 V. The second trapping happens at 11.9 s, when APD voltage starts to oscillate, and the level of voltage increases to 0.39 V, indicating trapping the other particle. This a rare occurrence in these measurements (less than 1%) and such double trapping events are discarded.

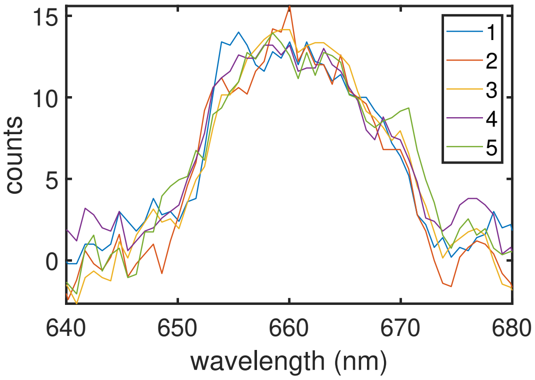

Figure B-S7: Luminescence emission spectrum from a single aperture for five measurements in a row of single UCNCs.

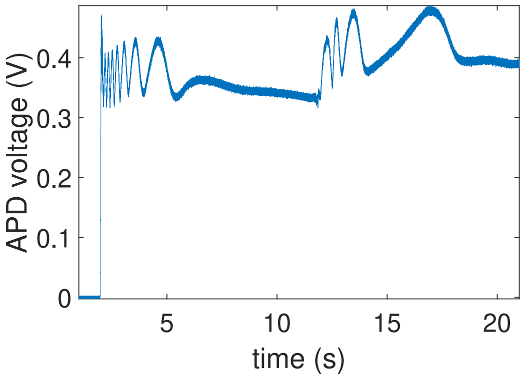

Figure B-S8: Trapping two particles. The second trapping event is seen with oscillations and an increase in voltage starting at 11.9 s.

E. Discrete emission

Figs. B-S9 and B-S10 show discreet emission levels for 200 measurements of UCNCs samples with 0.006 Er and 0.076 Er per UCNC. The concentration of UCNC is 2×10^{10} particles/cm^3 with 39 mW incident power of 980 nm laser and 30 s emission integration time. The sample with 0.006 Er per particle show 199 trapping signal without any emission (0 Er) and one trapping event with emission spectrum. Sample with 0.076 Er per UCNC shows 190 trapping event without emission, nine events with single Er emission, and an event with multiple Er ions. Experimental results are fitted with Poisson distribution. The mean value calculated with equation B-S1 based on the emission counts. P(n) is the trapping probability for n number of Er.

$$\lambda = \sum_{n=0}^{\infty} P(n) \times n \tag{B-S1}$$

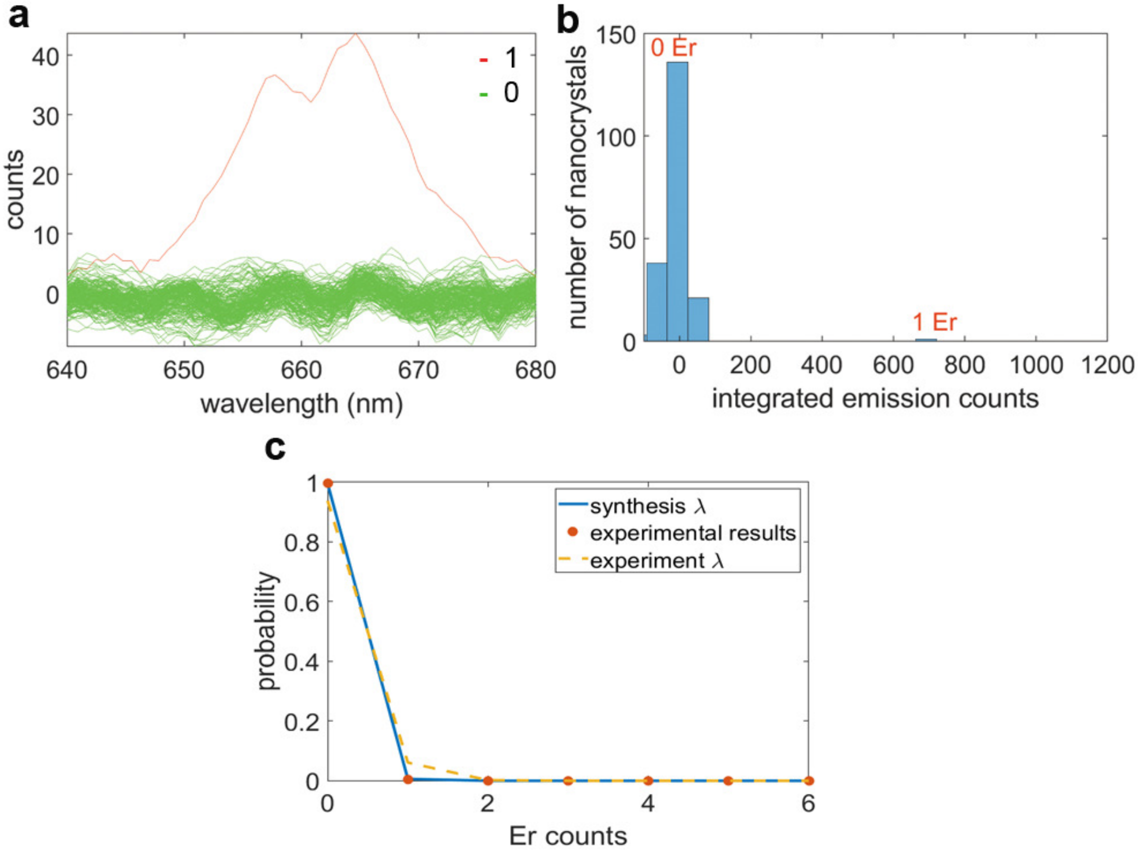

Figure B-S9: Statistics of emitters observed in experiment.(a) Observed emission spectra for sample containing a mean number of 0.006 Er ions per nanocrystal particle. (b) Histogram of integrated emission counts for 200 trapping events. (b) Probability of having 0 to 6 Er emitters based on experimental measurements (part (b)) and using Poisson distributions using expected synthesis statistics having a mean Er count of 0.006 per particle and calculated experimental mean value of 0.005.

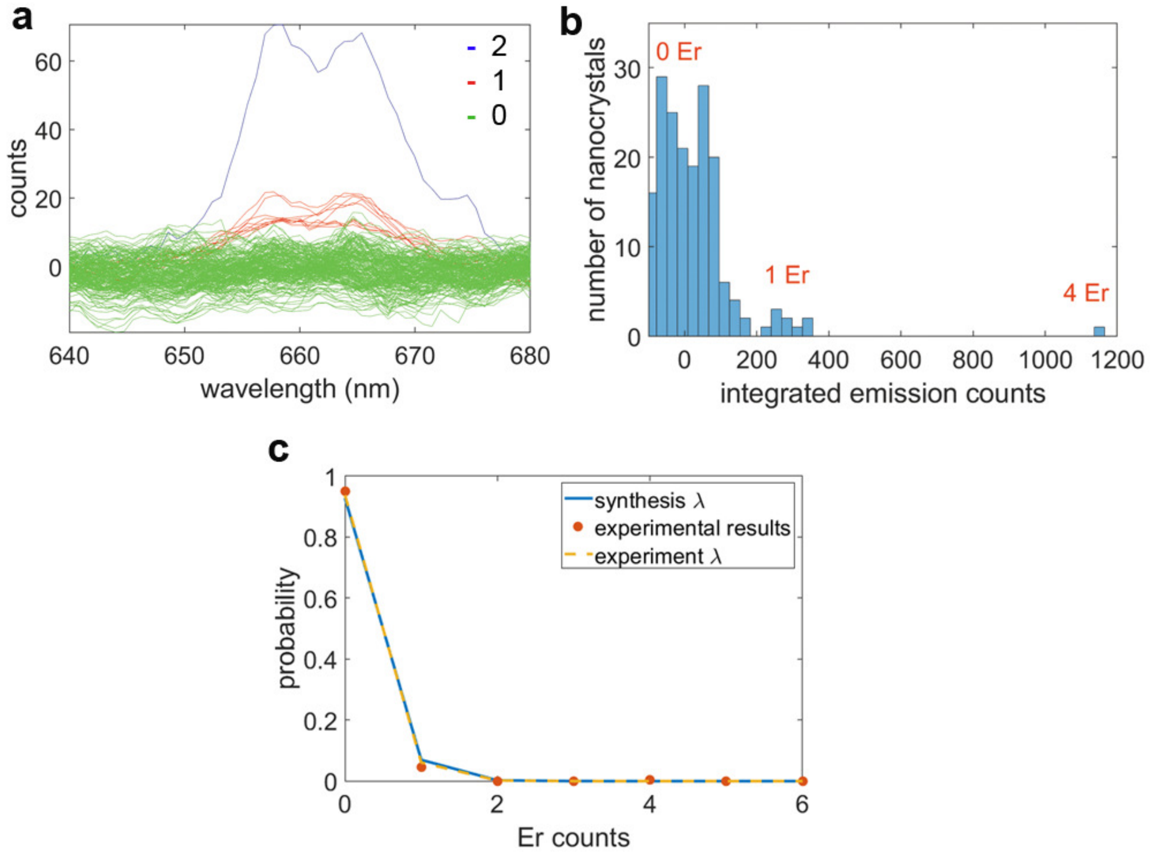

Figure B-S10: Statistics of emitters observed in experiment.(a) Observed emission spectra for sample containing a mean number of 0.076 Er ions per nanocrystal particle. (b) Histogram of integrated emission counts for 200 trapping events. (b) Probability of having 0 to 6 Er emitters based on experimental measurements (part (b)) and using Poisson distributions using expected synthesis statistics having a mean Er count of 0.076 per particle and calculated experimental mean value of 0.065.

F. 550 nm emission

Figure B-S11 shows discrete level of upconversion emission at 550 nm for 100 trapping events for sample with 1.53 Er per UCNC.

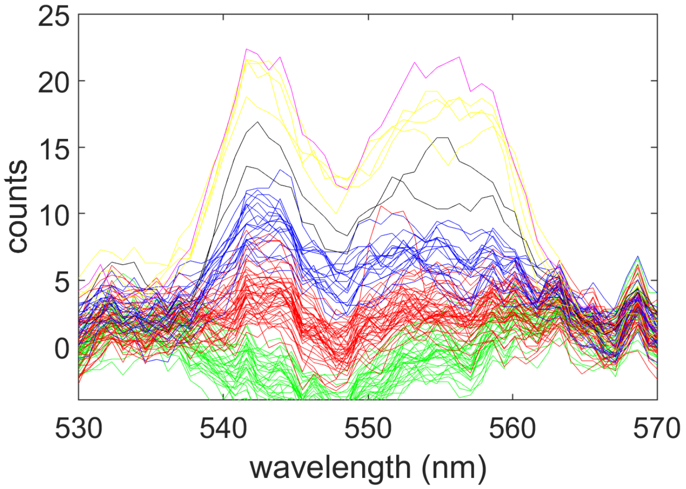

Figure B-S11: Upconversion emission at 550 nm

G. 1550 nm emission

Infrared emission spectroscopy was performed using a JDS uniphase 980 nm pump laser diode operating at 1.6 W with 1.53 Er/UCNC in a 1 × 1 × 3.5 cm quartz cuvette. The diode was coupled to an optical fiber and emission of the fiber tip collimated to 1 mm^2 using a Newport F-91-C1-T multimode fiber coupler. The emission was measured and corrected for instrument response using a liquid-nitrogen cooled Hamamatsu R5509 NIR PMT between 1450 nm and 1650 nm. The step size was 0.5 nm and each point was integrated for 0.5 seconds for 40 subsequent scans, for a total measuring time of 8000 seconds. The experiment was repeated for hexane under the same conditions.

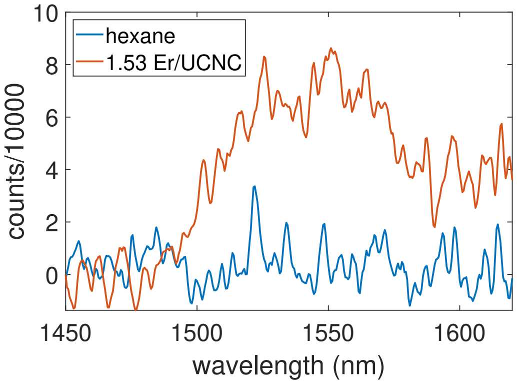

Figure B-S12: Emission at 1530 nm. Emission spectra of hexane and 1.5 Er/UCNCs.

H. Er average distances

Er average distances (d) calculated using hexagonal lattice parameters a and c with Er doping level of x.(B-S3)

$$d = (\frac{a^2 \times c \times \sqrt{3}/2}{1.5\ x})^{1/3} \qquad \text{(B-S2)}$$

Table S1: Average distance of Er ions inside UCNCs

Er/UCNC	Er-Er distance (nm)
2	14.05
3	12.27
4	11.16
5	10.35

References

[B-S1] Sobolev, B. P.; Mineev, D.; Pashutin, V. Low-temperature hexagonal modification of $NaYF_4$ having the gagarinite structure. Doklady Akademii Nauk. 1963; pp 791-794.

[B-S2] Alizadehkhaledi, A.; Frencken, A. L.; Dezfouli, M. K.; Hughes, S.; van Veggel, F. C. J. M.; Gordon, R. Cascaded plasmon-enhanced emission from a single upconverting nanocrystal. *ACS Photonics* **2019**, *6*, 1125-1131.

[B-S3] Fischer, S.; Johnson, N. J.; Pichaandi, J.; Goldschmidt, J. C.; van Veggel, F. C. J. M. Upconverting core-shell nanocrystals with high quantum yield under low irradiance: On the role of isotropic and thick shells. *J. Appl. Phys.* **2015**, *118*, 193105.

C Bright Upconverted Emission from Light-Induced Inelastic Tunneling

Bright Upconverted Emission from Light-Induced Inelastic Tunneling

Eradzh Rakhmatov,[†,‡] Amirhossein Alizadehkhaledi,[†,‡] Ghazal Hajisalem,[†,‡] and Reuven Gordon[*,†,‡]

†*Department Electrical and Computer Engineering, University of Victoria, Victoria, British Columbia V8P 5C2, Canada*

‡*Centre for Advanced Materials & Related Technologies (CAMTEC), University of Victoria, Victoria, British Columbia V8W 2Y2, Canada*

E-mail: rgordon@uvic.ca

Abstract

Upconverted light from nanostructured metal surfaces can be produced by harmonic generation and multi-photon luminescence; however, these are very weak processes and require extremely high field intensities to produce a measurable signal. Here we report on bright emission, 5 orders of magnitude greater than harmonic generation, that can be seen from metal tunnel junctions due to light-induced inelastic tunneling. Like inelastic tunneling light emission, which was recently reported to have 2% conversion efficiency per tunneling event, the emission wavelength recorded varies with the local electric field applied; however, here the field is from a 1560 nm femtosecond pulsed laser source. Finite-difference time-domain simulations of the experimental conditions show the local field is sufficient to generate tunneling-based inelastic light emission in the visible regime. This phenomenon is promising for producing ultrafast upconverted light emission with higher efficiency than conventional nonlinear processes.

Keywords

upconversion, plasmonics, ultrafast, tunneling

Several effects are recognized to produce light using metal nanostructures in the field of nanoplasmonics. When applying a pulsed laser to a metal surface or nanostructure, light can be generated by nonlinear processes including second harmonic generation,(C1)–(C3) third harmonic generation,(C4),(C5) two-photon photoluminescence(C6)–(C9) and three-photon photoluminescence.(C5),(C6) In each of these effects, the photon energy of the emitted photons is greater than the incident energy. Notably, these nonlinear effects have extremely low conversion efficiency even for resonant metal structures including an additional nonlinear material. The conversion efficiency is typically less than a fraction of a percent.(C10)–(C15)

Another well-known effect in nanoplasmonics is inelastic tunneling-induced light emission. Metal tunnel junctions under DC bias can produce light if the tunneling electron scatters inelastically.(C16)–(C18) The signature of this effect is that the photon energy produced has a cut-off equal to the bias for the electron across the tunnel junction. Recently, a high efficiency of 2% has been reported for this effect(C19),(C20) and it was suggested that even higher efficiency values are possible with improved design.(C21)

It has also been noted that optical pulses can be used to create tunneling based ejection of electrons from metal surfaces.(C22)–(C26) The electric field within the femtosecond laser pulse lowers the barrier for tunneling based electron ejection. Many other works have explored the properties of electron ejection via tunneling out of a metal with an applied field and an ultrafast laser.(C27)–(C36) THz pulses have been used to produce ultrafast scanning tunneling microscopy,(C37) which followed from ultrafast scanning tunneling measurements.(C38) Within these works, the possibility of a tunneling electron inelastically scattering to produce a photon has not been explored.

Here we report bright upconverted light emission at a metal tunnel junction by the effect of inelastic tunneling: light-induced inelastic tunneling emission (LITE). We demonstrate that for sub-nanometer tunnel junctions excited by short infrared laser pulses, bright broad-spectrum visible light is emitted. The critical feature is that the emission shows the tunneling signature: the spectrum has a cut-off wavelength that blue-shifts with increasing electric field of the incident pulse. The observed emission wavelength range is consistent with finite-difference time-domain (FDTD) simulations that show that the magnitude of the voltage across the junction is comparable to cut-off voltage (energy divided by electric charge) of the emitted photon energy for the peak pulse intensities used.

The samples were gold nanoparticles (5 nm – 741949 Sigma-Aldrich) over an 30 nm thick ultra-flat gold (template stripped off silicon) with an amino-alkane-thiol self-assembled monolayer with varying carbon length (C2 – 30070 Sigma-Aldrich, C3 – 739294, Sigma-Aldrich, C6 – 733679 Sigma-Aldrich C8 – 745774 Sigma-Aldrich).(C39),(C40) (Samples were also fabricated with 20 nm and 60 nm, showing similar results, but these are not reported here – see Supporting Information for details of the fabrication and scanning electron microscope images). Dark-field scattering of the sample showed plasmon resonances. The transverse resonance was around 550 nm and the longitudinal resonances red-shifted with decreasing gap size produced by the self-assembled monolayer (around 680 nm for the C3 junction). The dark field measurement setup and results are shown in the Supporting Information.

The schematic of femtosecond excitation with emission and the experimental setup for LITE is shown schematically in Figures C1 (a) and (b). 100 fs pulses at 1560 nm centre wavelength were incident on the sample at 58° angle. A band-pass filter (Ed-

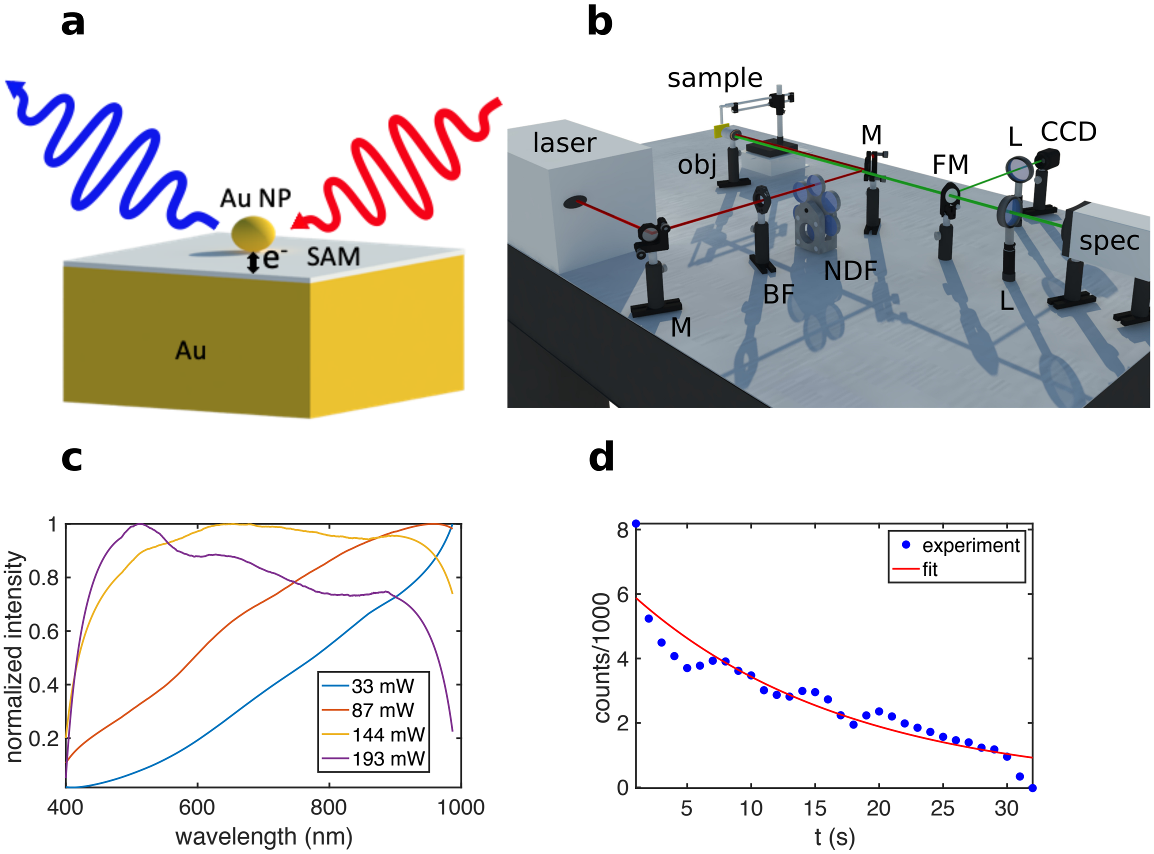

Figure C1: Light-induced Inelastic Tunneling Emission. (a) Schematic of metal nanoparticle over ultraflat gold with a self-assembled monolayer junction. An incident light pulse drives electron tunneling which emits a higher energy photon due to inelastic scattering. (b) Schematic of experimental setup for observing LITE emission: M - mirror, BF - band-pass filter, NDF - neutral dentsity filter, obj - 50× objective, FM - flip mirror, L - lens, CCD - CCD camera, spec - spectromteter. (c) Emission spectra for four different average powers, showing characteristic spectral shift of LITE. The sample was a 5 nm gold nanoparticle and a 0.69 nm junction. (d) Decay of LITE observed for a 0.51 nm junction at lower power excitation. The decay was much faster at high intensities (see Supporting Information).

mund Optics TECHSPEC Bandpass Filter 1575/50 nm 87871) was used to remove any spurious signal from the source's pump laser or harmonic generation at the source.

Figure C1(c) shows the recorded bright spectra of LITE recorded on a fiber-coupled photon-counting spectrometer (QE65000, Ocean Optics) with one second integration time. The extremely bright emission from LITE can be observed by the naked eye. The total intensity over the spectrum from 400 nm to 1000 nm is 33000 times brighter than third harmonic generation and 140000 times brighter than second harmonic generation (see Table 1).

Table 1: Comparison of LITE with harmonic generation by integrated counts for the same acquisition time and maximized collection efficiency for each effect.

Effect	**Integrated counts (400-1000 nm)**
SHG	239
THG	1006
LITE	3.3×10^7

It is important to note that the signal was optimized in each case: maximizing the second harmonic signal and third harmonic signal each time (since the alignment is slightly different due to chromatic effects).

We also observed two photon photoluminescence (TPPL) for longer integration times, producing a broad spectrum. TPPL is easily distinguished from LITE because the TPPL spectra did not shift with varying excitation intensity. The characterization of the harmonic generation and TPPL is given in the Supporting Information (power and spectral dependence).

LITE was observed for two-carbon and three-carbon self-assembled monolayer junctions, with widths of 0.51 nm and 0.69 nm (see Supporting Information). The six-carbon and eight-carbon junctions did not produce LITE, which is consistent with these large junctions having negligible probability of tunneling, with widths of 0.94 nm and 1.16 nm. By contrast, the larger junctions still produced TPPL and harmonic generation (see Supporting Information).

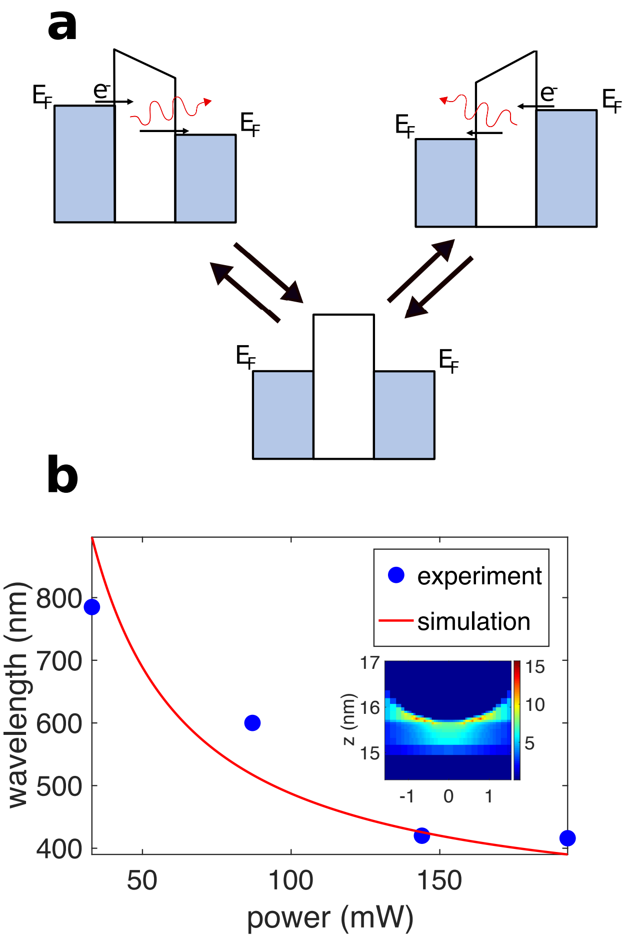

Figure C2: Comparison of calculated fields with observed cut-off wavelength. (a) Schematic of LITE effect resulting from the AC field of a femtosecond laser oscillating the bias applied to the tunnel junction. When the field induces tunneling, an upconverted photon can be emitted by inelastic scattering. (b) Finite-difference time-domain simulations provide the field strength as a function of the incident power in the experiment, which is translated to the cut-off wavelength for the LITE effect. The cut-off wavelength observed in the experiment (at half the maximum intensity) is shown for comparison with the calculations. The inset shows the local field intensity distribution in the junction region, normalized to the incident field intensity.

LITE is short lived, which is suspected to be the result of tunneling induced breakdown of the junction. Pulsed laser field-induced breakdown in dielectrics has been studied extensively, and typically occurs at V/nm laser fields used here.(C41) Even after LITE died out, the nonlinear effects of TPPL, SHG and THG persisted, although they were reduced.

Figure C1(d) shows the decay of the LITE for an incident average power of 45 mW with an exponential fit. The time-constant was twenty seconds. For higher intensities the decay was much faster; for example for 144 mW the decay was faster than the 100 ms integration of the spectrometer (see Supporting Information).

Other works have shown that the deformation of the shape of the metal nanoparticle can result in a blue shift, but this effect is permanent (melting),(C7) which distinguishes it from the results presented here. Other works have also shown flickering of multi-photon fluorescence, but LITE differs from that flickering because it does not turn back on once it dies out.(C5)

The physical picture of LITE is that the AC field of the femtosecond pulse source produces enough voltage in the junction to induce electron tunneling. The tunneling electron has a finite probability of inelastic scattering, which produces photon emission from the tunneling event. The emitted photon has energy which is less than the applied voltage divided by the electron charge (the potential energy available to the tunneling electron). (Thermal effects can give slightly higher energy photons). Figure C2(a) shows a schematic of this effect where the energy gap of the self-assembled monolayer presents a tunneling barrier and the energy bias across the barrier oscillates with the applied field from the femtosecond pulse.

To check the plausibility of this picture, we simulated the field amplitude at the 1560 nm pulse wavelength in the junction for the conditions of the experiment. We used FDTD simulations (FDTD - Lumerical v. 8.20.1731) with a mesh size of 0.05 nm, a total-field scattered field source, perfectly matched layer boundaries, and Johnson and Christy gold.(C42) The inset to Figure C2(b) shows the cross section of the field enhancement in the gap. We related the field amplitude to the cut-off wavelength for LITE:

$$\lambda_{\mathrm{c}} = \frac{hc}{Edq} \tag{C1}$$

where λ_c is cut-off wavelength, h is Planck's constant, c is speed of light, E is field amplitude, d is gap size, q is electron charge.

Figure C2(b) shows simulated the cut-off wavelength as a function of the average power of the laser. The laser repetition rate was 80 MHz and peak intensity of the 33 mW laser was $1.6 \times 10^{14}\ \frac{W}{m^2}$. The cut-off is in the visible regime for the conditions of this experiment, showing a blue-shift as the peak intensity increases. Since the spectra were also influenced by the local plasmon resonances (see dark-field spectra in Supporting Information), we do not attempt to quantitatively fit the observed spectra although this may be attempted with techniques used elsewhere.(C21),(C43),(C44) We do show the experimentally measured cut-off (defined as the wavelength were the counts goes to half of the peak value), to compare with the simulated results. Reasonable agreement is seen between the simulated and the experimental cut-off.

We recognize potential for significant improvement to the LITE effect. First, we are not exploiting the plasmonic resonance in the present investigation: the incident photon energy is well-away from the plasmon resonance and so the field enhancement is only a factor of 6 with respect to the incident field (see Supporting Information). Better overall conversion efficiency is expected by fully exploiting resonances at the incident and emission wavelengths.

Second, we expect that the light emission is extremely short in duration, although we have not time-resolved the emission in this work. This is expected since the tunneling can operate at optical frequencies due to the small capacitance of the junction.(C45) In particular, here we have a junction area of approximately 1-10 nm^2 with a gap of just under a nanometer; so the overall capacitance is below the aF range. In a well-designed case, the radiation resistance is less than a kOhm, so that the response time should be in the femtosecond regime. Therefore, this effect may be intriguing for ultra-fast nearfield excitation.

Third, LITE may be more efficient than conventional inelastic tunneling light emission because the light emission is limited in time to a cycle of the applied pulsed source. This means that the spectral bandwidth available is substantially narrower than DC-based emission and so less energy is expected to be lost to low energy photons that are typically not measured.(C46)

Finally, we note that the junctions here are extremely short-lived due to the self-assembled monolayer chosen. Others have investigated van der Waals hexagonal-BN as a stable junction for inelastic tunneling based emission.(C45),(C46) That material is crystalline and has a large band-gap, so it is expected that LITE lifetimes will be extended substantially, as was observed in DC measurements.

In summary, here we report bright upconverted emission from light induced inelastic tunneling between metals when they are incident with a pulsed laser source. Since this effect depends on tunneling based inelastic emission, it is limited by the efficiency of that effect, which is on the order of 2% per tunneling event and orders of magnitude more efficient than other nonlinear effects that operate in the near-field. By exploiting plasmonic resonances, the reduced tunneling bandwidth and more stable junction materials, it is expected that LITE will become a highly efficient ultrafast source of upconverted photons.

Acknowledgement

Support for this work is provided by an NSERC Discovery Grant.

Supporting Information Available

Scanning electron microscope images, dark field setup, dark field scattering results, third harmonic generation results, power dependence, two photon photoluminescence, LITE of C2, brief LITE observed for C3, simulation details.

Competing interests

The authors declare that there are no competing interests.

Corresponding Author

Reuven Gordon is the corresponding author. (rgordon@uvic.ca)

References

[C1] Chen, C.; de Castro, A. R. B.; Shen, Y. *Physical Review Letters* **1981**, *46*, 145.

[C2] Simon, H.; Mitchell, D.; Watson, J. *Physical Review Letters* **1974**, *33*, 1531.

[C3] Kauranen, M.; Zayats, A. V. *Nature Photonics* **2012**, *6*, 737.

[C4] Tsang, T. Y. *Optics Letters* **1996**, *21*, 245–247.

[C5] Lippitz, M.; van Dijk, M. A.; Orrit, M. *Nano Letters* **2005**, *5*, 799–802.

[C6] Boyd, G.; Yu, Z.; Shen, Y. *Physical Review B* **1986**, *33*, 7923.

[C7] Bouhelier, A.; Bachelot, R.; Lerondel, G.; Kostcheev, S.; Royer, P.; Wiederrecht, G. *Physical Review Letters* **2005**, *95*, 267405.

[C8] Zijlstra, P.; Chon, J. W.; Gu, M. *Nature* **2009**, *459*, 410.

[C9] Beversluis, M. R.; Bouhelier, A.; Novotny, L. *Physical Review B* **2003**, *68*, 115433.

[C10] Aouani, H.; Rahmani, M.; Navarro-Cía, M.; Maier, S. A. *Nature Nanotechnology* **2014**, *9*, 290.

[C11] Airola, M.; Liu, Y.; Blair, S. *Journal of Optics A: Pure and Applied Optics* **2005**, *7*, S118.

[C12] Hajisalem, G.; Nezami, M. S.; Gordon, R. *Nano Letters* **2014**, *14*, 6651–6654.

[C13] Melentiev, P. N.; Afanasiev, A. E.; Kuzin, A. A.; Baturin, A. S.; Balykin, V. I. *Optics Express* **2013**, *21*, 13896–13905.

[C14] Van Nieuwstadt, J.; Sandtke, M.; Harmsen, R.; Segerink, F. B.; Prangsma, J.; Enoch, S.; Kuipers, L. *Physical Review Letters* **2006**, *97*, 146102.

[C15] Nezami, M. S.; Yoo, D.; Hajisalem, G.; Oh, S.-H.; Gordon, R. *ACS Photonics* **2016**, *3*, 1461–1467.

[C16] Lambe, J.; McCarthy, S. *Physical Review Letters* **1976**, *37*, 923.

[C17] Persson, B.; Baratoff, A. *Physical Review Letters* **1992**, *68*, 3224.

[C18] Johansson, P.; Monreal, R.; Apell, P. *Physical Review B* **1990**, *42*, 9210.

[C19] Du, W.; Wang, T.; Chu, H.-S.; Nijhuis, C. A. *Nature Photonics* **2017**, *11*, 623.

[C20] Qian, H.; Hsu, S.-W.; Gurunatha, K.; Riley, C. T.; Zhao, J.; Lu, D.; Tao, A. R.; Liu, Z. *Nature Photonics* **2018**, *12*, 485–488.

[C21] Parzefall, M.; Novotny, L. *ACS Photonics* **2018**, *5*, 4195–4202.

[C22] Hommelhoff, P.; Sortais, Y.; Aghajani-Talesh, A.; Kasevich, M. A. *Physical Review Letters* **2006**, *96*, 077401.

[C23] Hommelhoff, P.; Kealhofer, C.; Kasevich, M. A. *Physical Review Letters* **2006**, *97*, 247402.

[C24] Herink, G.; Solli, D.; Gulde, M.; Ropers, C. *Nature* **2012**, *483*, 190.

[C25] Dombi, P.; Horl, A.; Racz, P.; Marton, I.; Trugler, A.; Krenn, J. R.; Hohenester, U. *Nano Letters* **2013**, *13*, 674–678.

[C26] Krüger, M.; Schenk, M.; Förster, M.; Hommelhoff, P. *Journal of Physics B: Atomic, Molecular and Optical Physics* **2012**, *45*, 074006.

[C27] Yanagisawa, H.; Hengsberger, M.; Leuenberger, D.; Klöckner, M.; Hafner, C.; Greber, T.; Osterwalder, J. *Physical Review Letters* **2011**, *107*, 087601.

[C28] Yanagisawa, H.; Hafner, C.; Doná, P.; Klöckner, M.; Leuenberger, D.; Greber, T.; Hengsberger, M.; Osterwalder, J. *Physical Review Letters* **2009**, *103*, 257603.

[C29] Ropers, C.; Solli, D.; Schulz, C.; Lienau, C.; Elsaesser, T. *Physical Review Letters* **2007**, *98*, 043907.

[C30] Bormann, R.; Gulde, M.; Weismann, A.; Yalunin, S.; Ropers, C. *Physical Review Letters* **2010**, *105*, 147601.

[C31] Schenk, M.; Krüger, M.; Hommelhoff, P. *Physical Review Letters* **2010**, *105*, 257601.

[C32] Irvine, S.; Dechant, A.; Elezzabi, A. *Physical Review Letters* **2004**, *93*, 184801.

[C33] Piglosiewicz, B.; Schmidt, S.; Park, D. J.; Vogelsang, J.; Groß, P.; Manzoni, C.; Farinello, P.; Cerullo, G.; Lienau, C. *Nature Photonics* **2014**, *8*, 37.

[C34] Park, D. J.; Piglosiewicz, B.; Schmidt, S.; Kollmann, H.; Mascheck, M.; Lienau, C. *Physical Review Letters* **2012**, *109*, 244803.

[C35] Vogelsang, J.; Robin, J.; Nagy, B. J.; Dombi, P.; Rosenkranz, D.; Schiek, M.; Groß, P.; Lienau, C. *Nano Letters* **2015**, *15*, 4685–4691.

[C36] Irvine, S.; Elezzabi, A. *Physical Review A* **2006**, *73*, 013815.

[C37] Cocker, T. L.; Jelic, V.; Gupta, M.; Molesky, S. J.; Burgess, J. A.; De Los Reyes, G.; Titova, L. V.; Tsui, Y. Y.; Freeman, M. R.; Hegmann, F. A. *Nature Photonics* **2013**, *7*, 620.

[C38] Weiss, S.; Botkin, D.; Ogletree, D.; Salmeron, M.; Chemla, D. *Physica Status Solidi (b)* **1995**, *188*, 343–359.

[C39] Ciracì, C.; Hill, R.; Mock, J.; Urzhumov, Y.; Fernández-Domínguez, A.; Maier, S.; Pendry, J.; Chilkoti, A.; Smith, D. *Science* **2012**, *337*, 1072–1074.

[C40] Hill, R. T.; Mock, J. J.; Hucknall, A.; Wolter, S. D.; Jokerst, N. M.; Smith, D. R.; Chilkoti, A. *ACS Nano* **2012**, *6*, 9237–9246.

[C41] Bloembergen, N. *IEEE Journal of Quantum Electronics* **1974**, *10*, 375–386.

[C42] Johnson, P. B.; Christy, R.-W. *Physical Review B* **1972**, *6*, 4370.

[C43] Wang, F.; Shen, Y. R. *Physical Review Letters* **2006**, *97*, 206806.

[C44] Novotny, L.; Hecht, B. *Principles of nano-optics*; Cambridge university press, 2012.

[C45] Parzefall, M.; Bharadwaj, P.; Jain, A.; Taniguchi, T.; Watanabe, K.; Novotny, L. *Nature Nanotechnology* **2015**, *10*, 1058.

[C46] Parzefall, M.; Szabó, Á.; Taniguchi, T.; Watanabe, K.; Luisier, M.; Novotny, L. *Nature Communications* **2019**, *10*, 292.

Supporting Information for "Bright Upconverted Emission from Light-Induced Inelastic Tunneling"

Eradzh Rakhmatov,[†,‡] Amirhossein Alizadehkhaledi,[†,‡] Ghazal Hajisalem,[†,‡] and Reuven Gordon[*,†,‡]

†*Department Electrical and Computer Engineering, University of Victoria, Victoria, British Columbia V8P 5C2, Canada*

‡*Centre for Advanced Materials & Related Technologies (CAMTEC), University of Victoria, Victoria, British Columbia V8W 2Y2, Canada*

E-mail: rgordon@uvic.ca

Fabrication procedure

30 nm of Au was sputtered using a Mantis QUBE sputter deposition system on polished side of a silicon sample without any adhesion layer to allow for stripping. Silicon was used because of its crystalline properties that allows ultraflat gold after stripping. For stripping, UV cured epoxy was sandwiched between the gold on silicon and a glass slide. After exposing the epoxy to UV light, it hardened attaching the gold to glass and thus revealing the ultraflat gold surface. Samples were immersed in 3 mM ethanol solution of different self assembled monolayers (SAM) for 18 h. This procedure was followed by rinsing with ethanol 3-4 times to remove unattached SAMs

and drying with nitrogen. The final step was to deposit nanoparticles (5 nm – 741949 Sigma-Aldrich 5.5×10^{13} particles/mL, 20 nm – 741965 Sigma-Aldrich 6.54×10^{11} particles/mL, 60 nm – 742015 Sigma-Aldrich 1.9×10^{10} particles/mL) by drop coating 500 μl of NPs in solution on sample and leaving it for 30 min, followed by rinsing samples 3-4 times with deionized water to remove unattached NPs and drying with nitrogen.

Figure C-S1 shows scanninng electron microscope (SEM) images. The sample with 20 nm NPs is substantially more dense as compared to the sample with 60 nm NPs because its initial solution used for deposition is 10 times more concentrated.

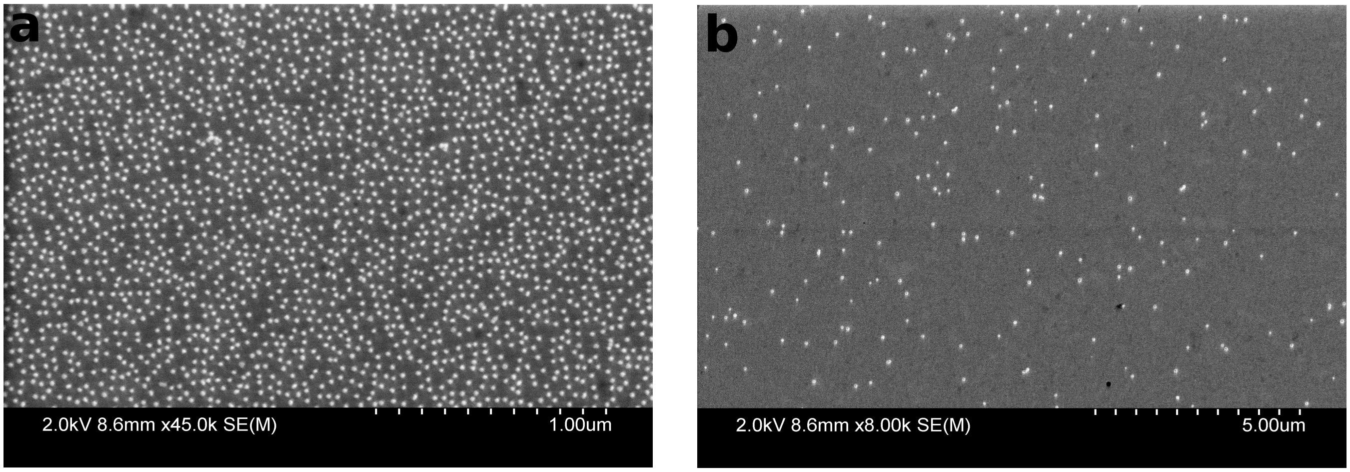

Figure C-S1: SEM images of samples with a) 20 nm NPs and b) 60 nm NPs.

Dark field measurement

The dark field setup is shown in Figure C-S2. The sample was positioned in a way to make a 65° angle between normal of the sample and incident light. This was necessary to ensure that only the scattered light was collected. Scratches and agglomerations were avoided by looking at the dark field image before taking a measurement. An Ocean Optics LS-1 Tungsten Halogen Light Source was used as white light source. A 20× 0.28 NA Mitutoyo objective was used for incident light and 10× 0.28 NA

Mitutoyo objective was used to collect scattered light. A QE65000 Ocean Optics spectrometer was used for signal collection.

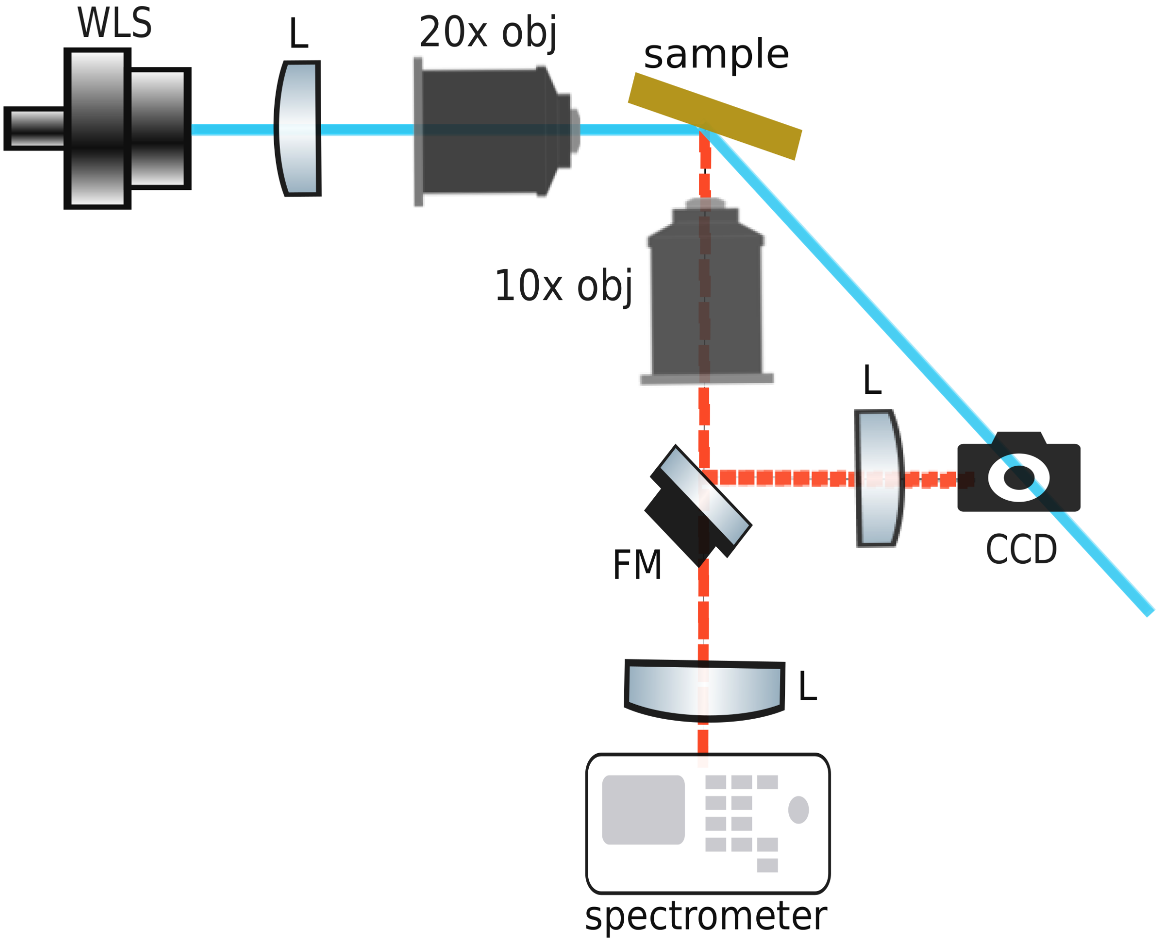

Figure C-S2: Dark-field measurement setup. WLS - white light source, L - lens, 20x objective, 10x objective, FM - flip mirror, CCD camera. In b) Incident and reflected light are represented with blue line and scattered light is represented with dashed red line.

Dark-field measurement results are presented in Figure C-S3. All the spectra show a red shift as the SAM thickness is reduced, as expected. The transverse mode can also be seen as a shoulder around 550 nm.

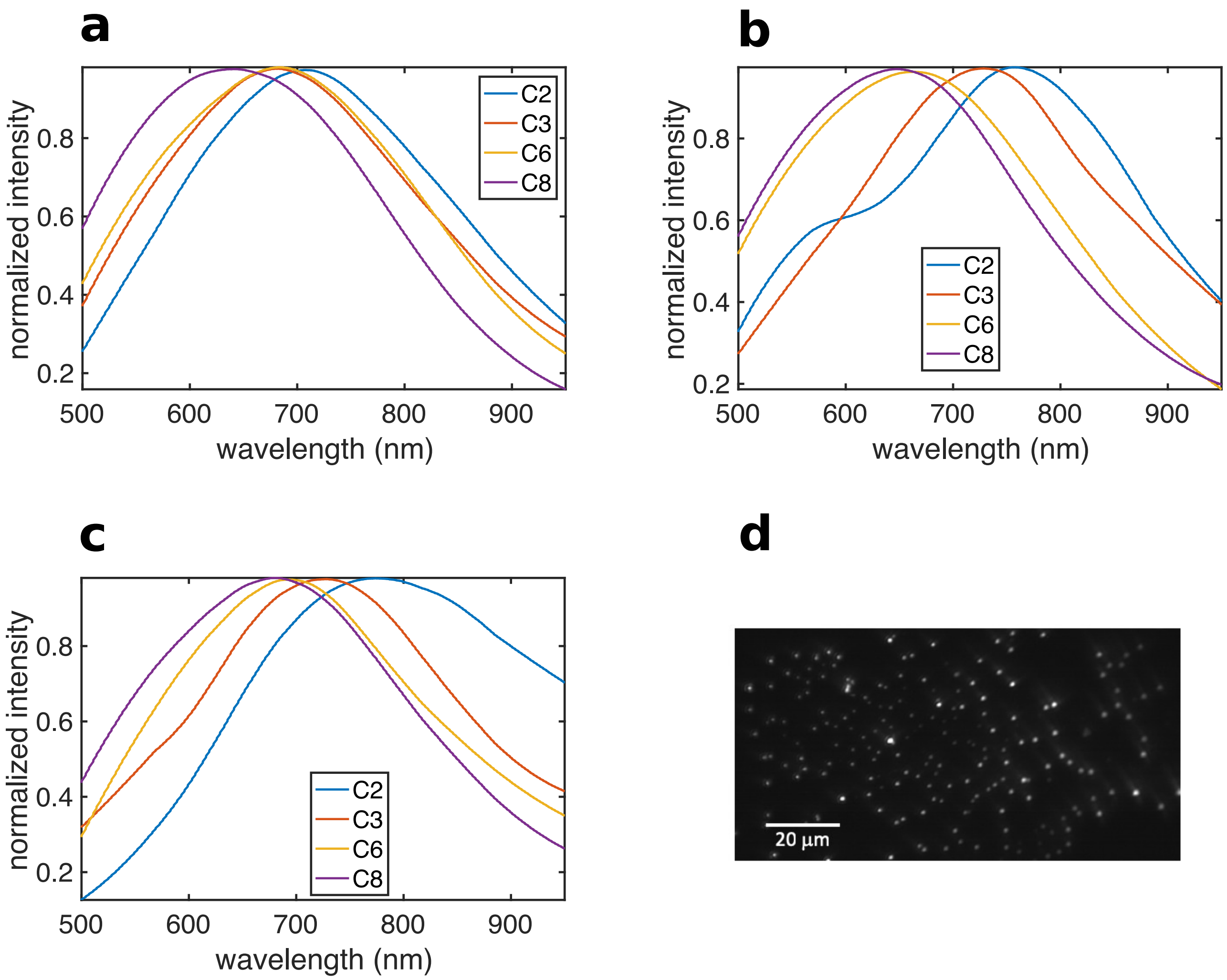

Figure C-S3: Dark-field scattering of samples with a) 5 nm NPs, b) 20 nm NPs and c) 60 nm NPs. d) Dark-field scattering CCD camera image.

Third harmonic generation measurement

Third harmonic generation (THG) measurement results are presented in Figure C-S4. A Calmar femtosecond laser centred at 1560 nm with average power of 100 mW was used as a laser source and signal was collected using a QE65000 Ocean Optics spectrometer with a ten second integration time. A bandpass filter was used to remove harmonics present in the laser and a neutral density filter was used to regulate the average power. When the SAM thickness was decreased, larger THG intensity was observed with a maximum for C3. THG intensity dropped for C2 due to onset of tunneling.(C-S1)

Figure C-S5 shows the power dependence of third harmonic generation with the slope of 3 for different SAMs, as expected from a three photon process.

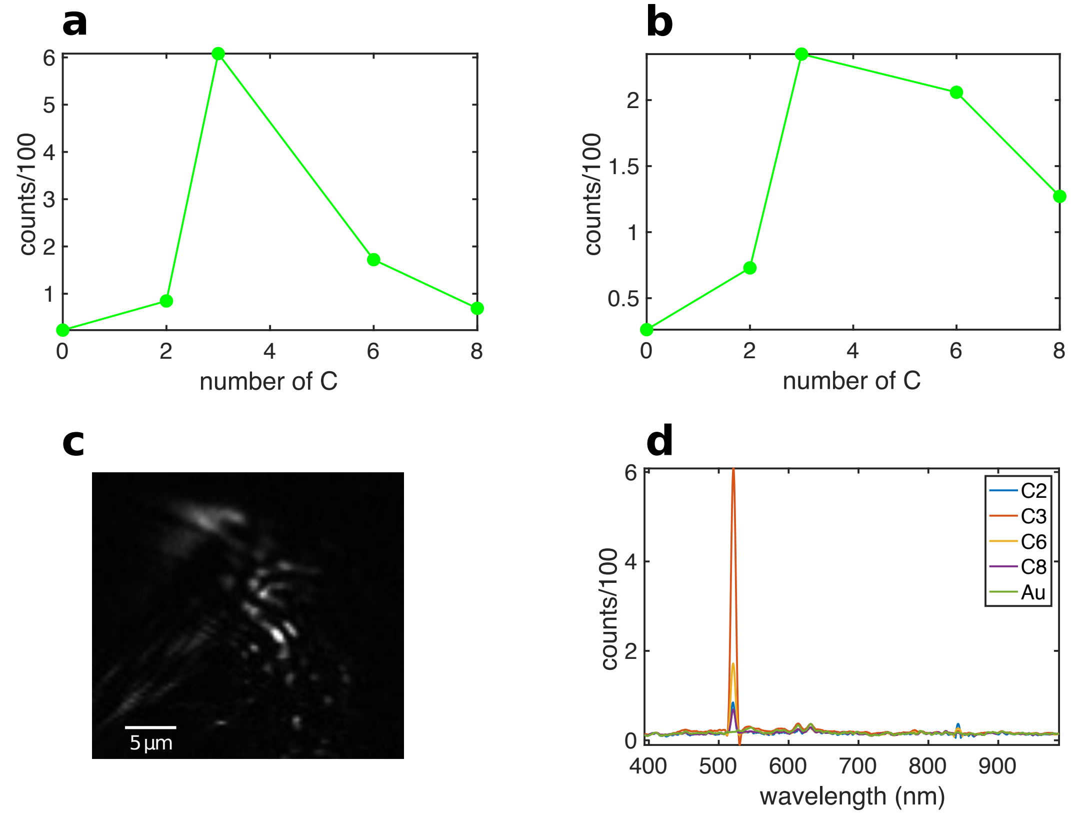

Figure C-S4: a) Third harmonic generation intensities for different SAMs of samples with 5 nm NPs and b) 60 nm NPs. c) CCD camera image of third harmonic generation. d) Third harmonic generation spectra.

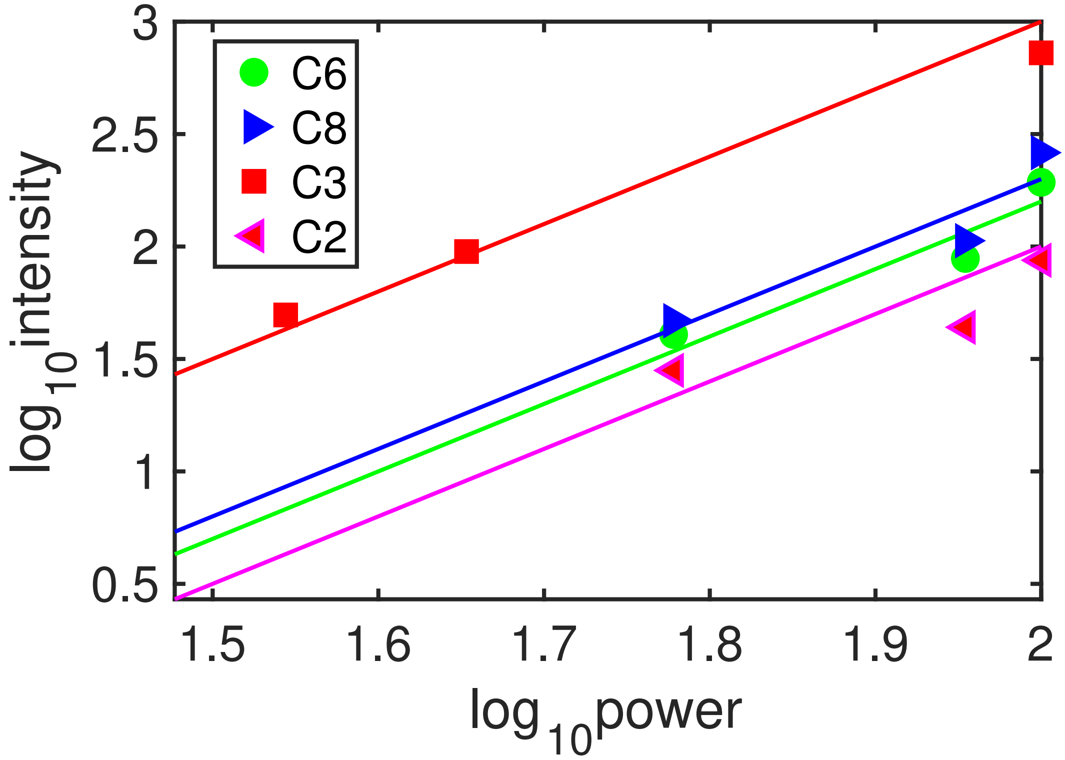

Figure C-S5: Third harmonic generation power dependence of samples with 5 nm NPs. Slope is 3 for all, as expected from a three photon process.

Two photon photoluminescence

Figure C-S6a shows two photon photoluminescence (TPPL) for different incident powers. No shift is observed. The wavelength axis is truncated at 1000 nm because of the range of spectrometer. Figure C-S6b shows the power dependence of TPPL with the slope of 2, as expected from a two photon process.

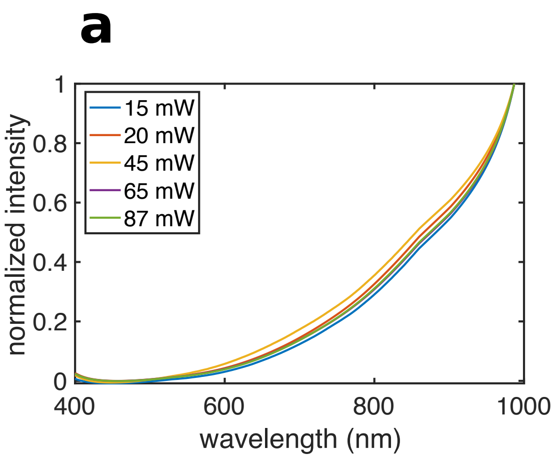

Figure C-S6: a) TPPL with different incident power from C3 with 5 nm Au NPs. b) power dependence of TPPL with slope equal 2, as expected from a two photon process.

Light-induced inelastic tunneling emission

Figure C-S7 shows LITE of the C2 sample. A blue shift was observed with larger intensities of the incident laser. The spectra are truncated at 1000 nm because of the range of spectrometer.

Figure C-S8 shows that for larger incident laser power, LITE is faster than 100 ms second. In an attempt to measure decay time, integration time was reduced to 50 ms and 10 ms without showing sufficient time resolution to resolve the decay for these conditions.

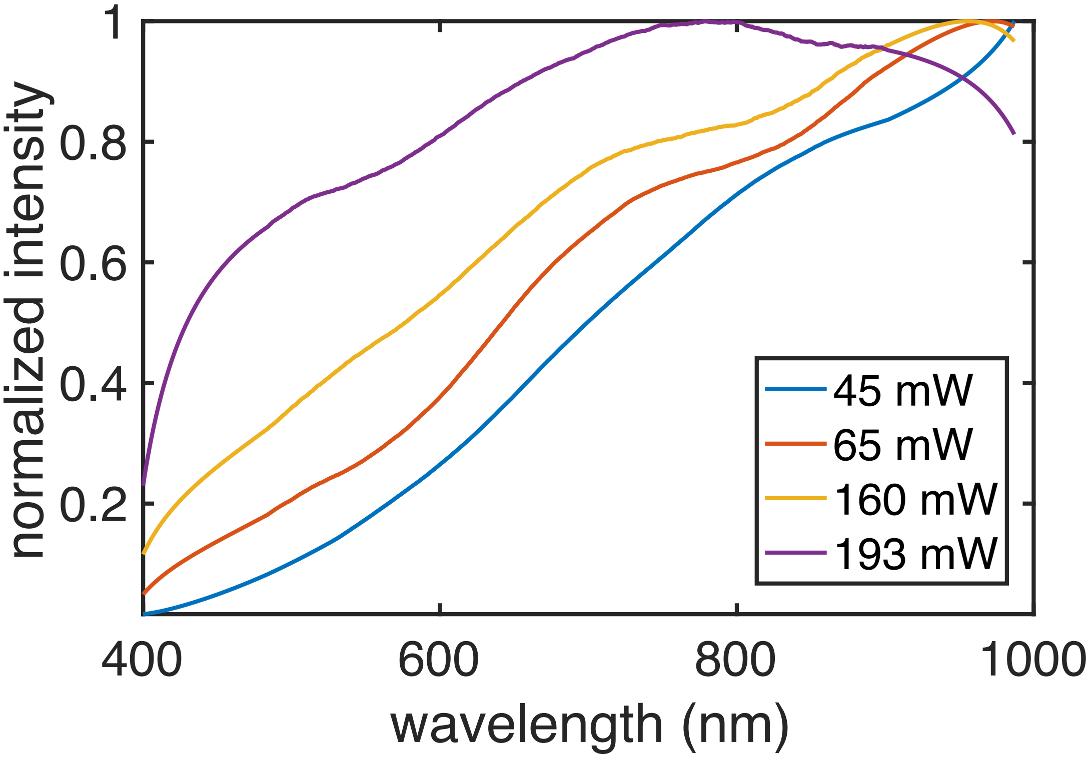

Figure C-S7: LITE of C2 with 5 nm Au NPs.

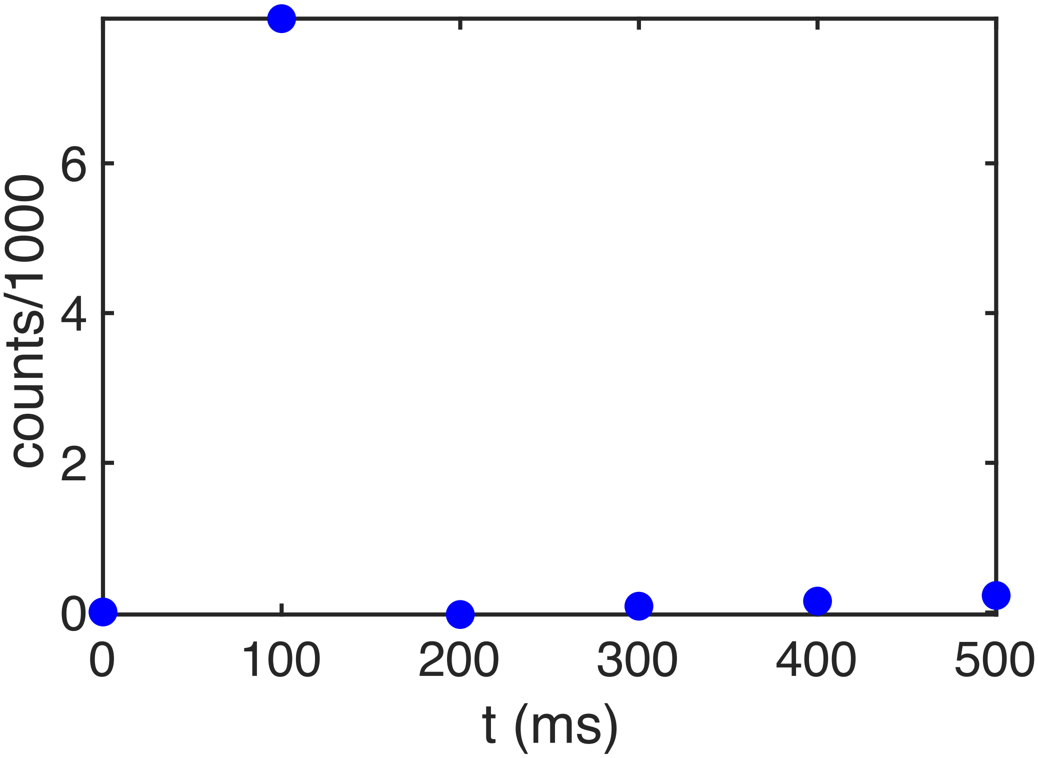

Figure C-S8: Brief LITE observed for C3 with 144 mW average power

Simulation

A finite difference time domain (FDTD - Lumerical v. 8.20.1731) simulation was used with the following parameters: 0.05 nm mesh size in the gap and 10 nm over nanoparticle, refractive index of the gap is 1.4, total field scattered field source (100 fs pulse source with centre wavelength at 1560 nm) at the 58 degree angle (to account for off-axis alignment). Perfectly Matched Layer boundaries were used. Although C3 and C2 have subnanometer thickness (0.69 nm and 0.51 nm),(C-S2) tunneling was neglected in the FDTD simulation because other works show that for C3 field amplitude in the gap for quantum corrected and classical models are similar .(C-S1),(C-S3)

Comparing electric field at the source and in the gap on Figure C-S9, an enhancement factor of 5.8 was determined, and it was used to calculate the actual experimental electric field in the gap using:

$$E_{\mathrm{exp}} = F\sqrt{\frac{E_{\mathrm{s}}^2 I_{\mathrm{exp}}}{I_{\mathrm{s}}}} \tag{C-S1}$$

where F is enhancement factor, E_{exp} is field amplitude of the experiment, E_{s} field amplitude of the simulation, I_{exp} source intensity of the experiment calculated using equation C-S2, I_{s} source intensity of the simulation.

$$I_{\mathrm{s}} = \frac{P_{\mathrm{peak}}}{A} \tag{C-S2}$$

where P_{peak} is peak laser power and A is illuminated area. P_{peak} was calculated from:

$$P_{\mathrm{peak}} = \frac{P_{\mathrm{avg}}}{R\tau} \tag{C-S3}$$

where P_{avg} is average source power, R is repetition rate, τ is pulse width. Repetition rate is 80 MHz, pulse width 100 fs.

Once electric field amplitude of the experiment is known, cut off wavelength is

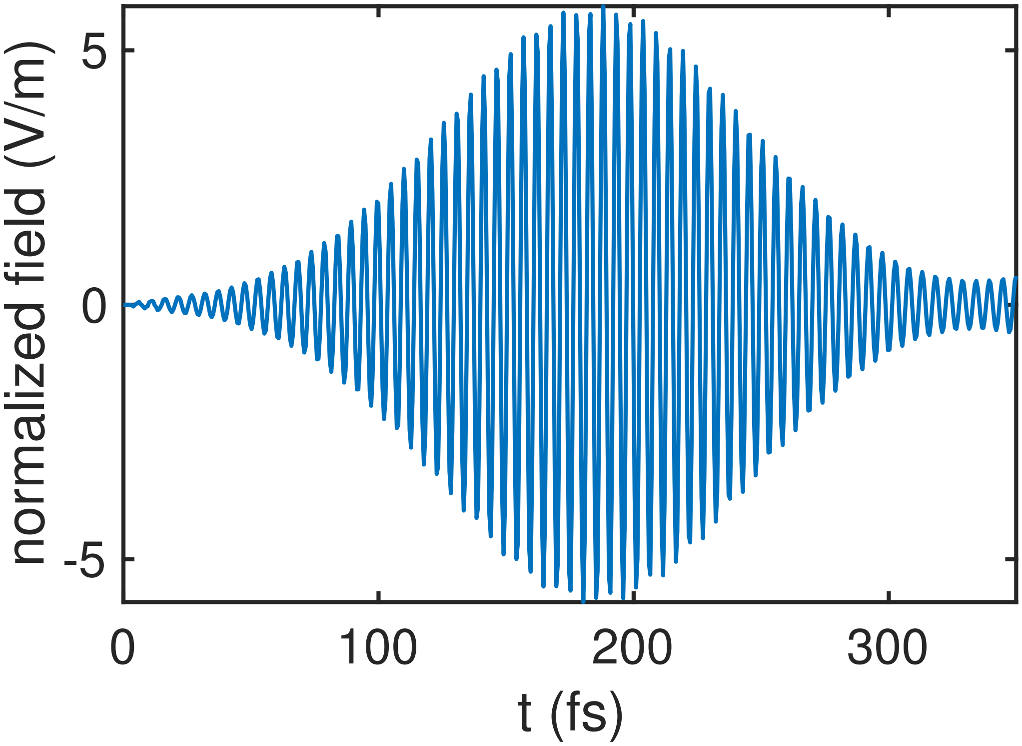

Figure C-S9: Time-domain information of the field in the gap.

calculated using:

$$\lambda_c = \frac{hc}{Edq} \tag{C-S4}$$

where λ_c is cut-off wavelength, h is Planck's constant, c is speed of light, E is field amplitude, d is gap size, q is electron charge.

References

[C-S1] Hajisalem, G.; Nezami, M. S.; Gordon, R. *Nano Letters* **2014**, *14*, 6651–6654.

[C-S2] Ciracì, C.; Hill, R.; Mock, J.; Urzhumov, Y.; Fernández-Domínguez, A.; Maier, S.; Pendry, J.; Chilkoti, A.; Smith, D. *Science* **2012**, *337*, 1072–1074.

[C-S3] Khademi, A.; Dewolf, T.; Gordon, R. *Optics Express* **2018**, *26*, 15656–15664.

D Harvesting Dual-Wavelength Excitation with Plasmon-Enhanced Emission from Upconverting Nanoparticles

(2018, ACS Photonics, volume 5, pp 3507-3512)

Harvesting dual-wavelength excitation with plasmon-enhanced emission from upconverting nanoparticles

Mirali Seyed Shariatdoust,[†,§] Adriaan L. Frencken,[‡,§] Ali Khademi,[¶,§]
Amirhossein Alizadehkhaledi,[¶,§] Frank C.J.M. van Veggel,[‡,§] and Reuven
Gordon[*,¶,§]

†*Department of Electrical and Computer Engineering, University of Victoria, Victoria, British Columbia V8P 5C2, Canada*

‡*Department of Chemistry, University of Victoria, British Colombia V8W 3V6, Canada*

¶*Department Electrical and Computer Engineering, University of Victoria, Victoria, British Columbia V8P 5C2, Canada*

§*Center for Advanced Materials & Related Technologies (CAMTEC), University of Victoria, Victoria, British Columbia V8W 2Y2, Canada*

E-mail: rgordon@uvic.ca

Phone: +1 250 472 5179 . Fax: +1 250 721 6052

Abstract

We demonstrate dual wavelength (1210 nm and 1520 nm) excitation of upconverter nanoparticles (Er doped nanoparticles) with plasmon-enhanced emission. 25 nm diameter gold nanorods with resonances at 808 nm and at 980 nm selectively enhance the upconversion emission of 2% erbium-doped

$NaYF_4$ nanoparticles at 808 nm and at 980 nm. No upconversion is seen for 1210 nm excitation alone and 1520 nm excitation alone provides lower upconversion. The sequential 1520 nm and 1210 nm absorption yields the most upconversion and the power dependence of emission supports the sequential absorption mechanism. This provides a promising avenue for harvesting from the two strongest infrared bands of the solar spectrum with selective emission tuned to either the Si or GaAs bandgap.

Keywords

upconverting nanoparticles; plasmon enhanced emission; lanthanides; dual-wavelength excitation; energy conversion; nanorods

Upconversion is an optical process that combines the energy from low energy photons to provide higher energy photon emission. It is typically more efficient than nonlinear harmonic generation, and so it is of interest for solar harvesting applications whereby photons that do not have sufficient energy to be absorbed can be converted into higher energy photons.(D1)–(D5) Lanthanides have long-lived electronic excitations that can be used as intermediate states for upconversion. While having typically lower efficiency than bulk, lanthanide doped nanoparticles are well suited for simple processing and plasmon coupling schemes(D6)–(D15) Beside rare-earth lanthanides, dye-sensitizers using triplet-triplet annihilation is another system that benefits from plasmonic enhancement.(D16),(D17)

Most work has focused on 980 nm excitation of Yb sensitized Er; however, for the dominant silicon based solar cell technology, upconversion for wavelengths larger than the bandgap wavelength (>1100 nm) is desired.(D18)–(D22) Several works have reported on ∼1520 nm upconversion of Er for emission at 980, 808, 655, 544 nm.(D23)–(D27) This has the disadvantage of harvesting only a small part of the IR solar spectrum. There is also the interesting possibility of sequential absorption of a 1520 nm photon from $I_{15/2}$

– $I_{13/2}$ followed by a 1210 nm photon from $I_{13/2}$ — $F_{9/2}$ and subsequent upconversion. We have found only one work where an analogous 1130 nm + 1500 nm barium vapor laser was used to achieve this sequential excitation and upconversion of Er doped fluorzirconate in a preform.(D28) The excitation at 1130 nm is not ideal, however, since it is in the minimum of the solar excitation spectrum.

Figure D1 shows the solar spectrum and the sequential excitation and upconversion emission scheme of interest for dual wavelength upconversion. For Silicon solar cells, currently operating above 26% efficiency,(D29)–(D31) additional upconverted photons may provide (albeit extremely modest) additional energy close to the bandedge by enhancing the 980 nm transition. This preferential enhancement will provide less heating in the bulk of the solar cell. For GaAs solar cells, currently operating close to 28.8% efficiency,(D31),(D32) 980 nm photons are not absorbed, and so selective emission of 808 nm upconverted photons is desired. Plasmonic enhanced upconversion is one of the most promising schemes for selecting the excitation and emission wavelengths.(D33)–(D42)

In this work, we provide a proof-of-principle demonstration of dual-wavelength excitation and plasmon-enhanced selective emission from Er doped nanoparticles. We first characterize the Er doped nanoparticles in solution and then drop-coated on glass and gold. Then we drop coat different resonance gold nanorods for selectively enhanced emission.

Figure D2 shows the upconversion emission spectrum of the Er doped nanoparticles in hexane solution with excitation at >1200 nm. The emission peaks of interest are around 980 nm and 808 nm, since these lie just below the bandedge wavelengths for Si and for GaAs.

Figure D3 shows the emission intensity at the 808 nm and 980 nm peaks for selective excitation. The selective excitation was achieved by filtering the excitation from a supercontinuum source. The intensity of the source was 0.4 W/cm^2 and the density

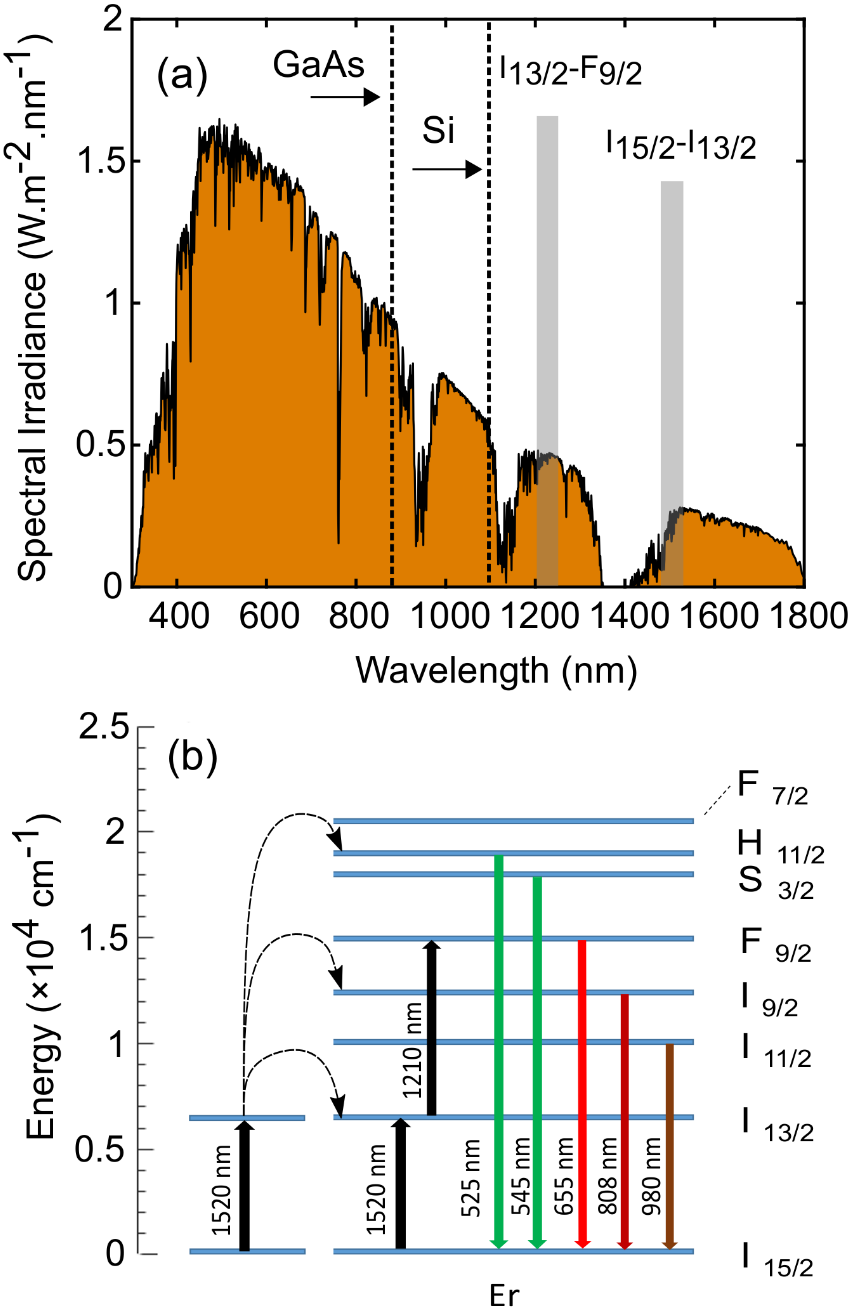

Figure D1: (a) AM 1.5 solar spectrum with IR absorption bands of Erbium shown in grey and band-edges of Si and GaAs shown with vertical dashed lines. (b) Energy diagram for Erbium showing upconversion fluorescence for pumping at 1520 nm, and dual pumping at 1520 nm + 1210 nm.

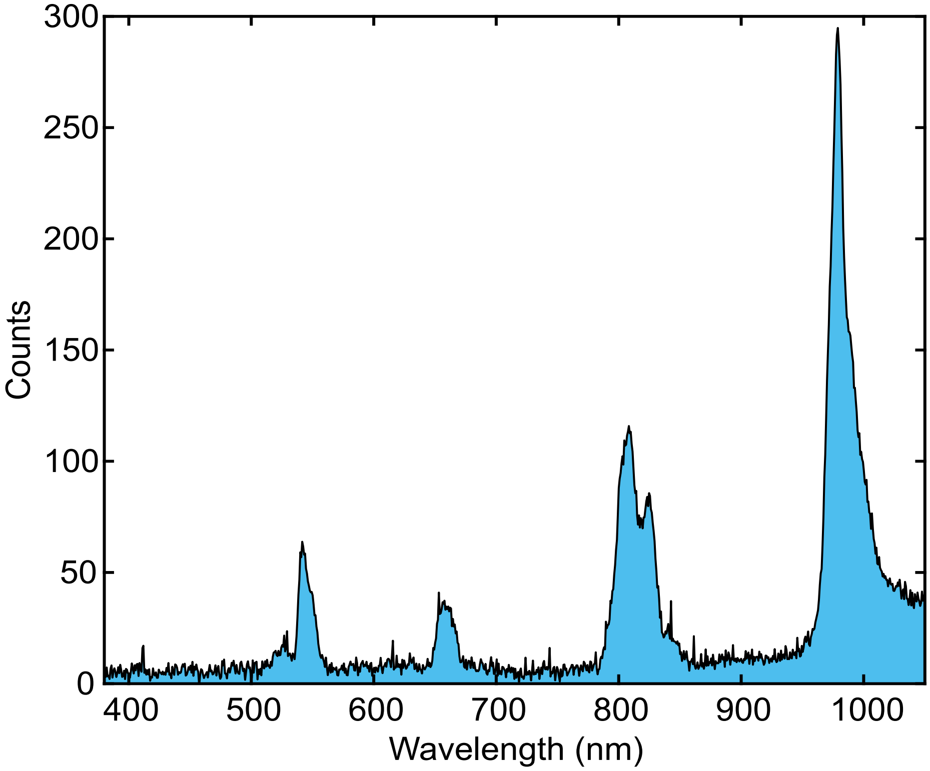

Figure D2: Upconversion emission spectrum of Er doped nanoparticles in hexane pumped with supercontinuum source >1200 nm wavelength.

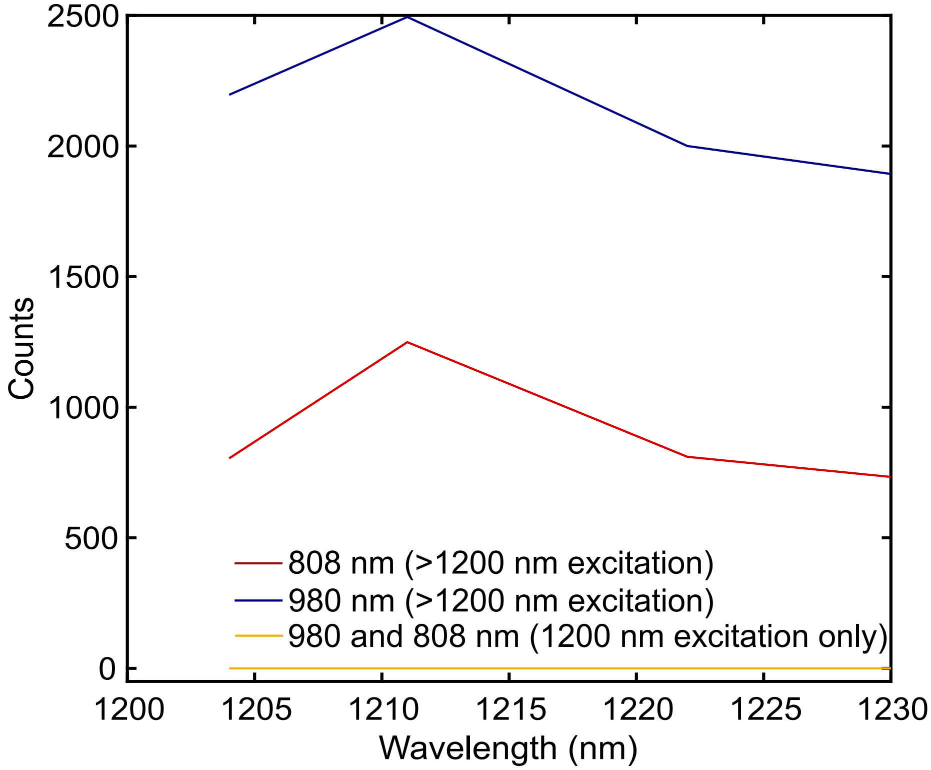

Figure D3: Emission at 808 nm and 980 nm when tuning the ~1200 nm excitation for the cases of simultaneous 1520 nm excitation and no 1520 nm excitation.

of Er doped nanoparticles in hexane was 14 mg/ml. Upconversion is not observable without 1520 nm excitation. Figure D3 shows upconversion emissions of 980 nm and 808 nm is increased by adding 1210 nm excitation. The >1200 nm excitation shows greater emission than the >1500 nm excitation alone. This shows that sequential absorption at 1520 nm and then 1210 nm is required to observe enhanced upconversion as shown in the scheme of Figure D1(b). Without the 1520 nm excitation, none of the 1210 nm photons can be harvested in the upconversion scheme. (Due to the low resolution of the prism selection of excitation, an absorption bandwidth of ∼10 nm is estimated around 1210 nm).

Figure D4 shows the power dependence for the excitation at 1520 nm and for >1200 nm (broadband). The >1500 nm excitation shows an approximately linear power dependence, whereas the >1200 nm excitation has an exponent between 2 and 3. The exponent between 2 and 3 supports that this is a multi-stage process.(D43) The linear slope for the >1500 nm excitation in Figure D4(a) suggests that the process is limited by an energy transfer step.

For one sun power density at 1210 nm and 1520 nm with 20 nm bandwidths, the accumulative power density is 0.0014 W/cm^2. With total power of 0.4 W/cm^2 for 1200-1600 nm excitation, the applied power density is 0.04 W/cm^2 for only 1200-1220 nm and 1510-1530 nm ranges. This shows our pump has approximately 28 times the sun power in that range. It is possible to increase the power via solar concentrators and have more energy harvesting of the 1210 nm and 1520 nm bands. Saturation occurs when the upconversion emission changes from a second order to a first order power dependence.(D44) Due to the fact that saturation for Er doped nanoparticles for 980 nm excitation happens in the range of 100-200 W/cm^2 power density,(D45) the applied power density in this investigation is far from saturation. Based on these findings, we believe that adding nanorods with resonances at 1210 nm and 1520 nm may provide additional near-field solar concentration and enable practical application

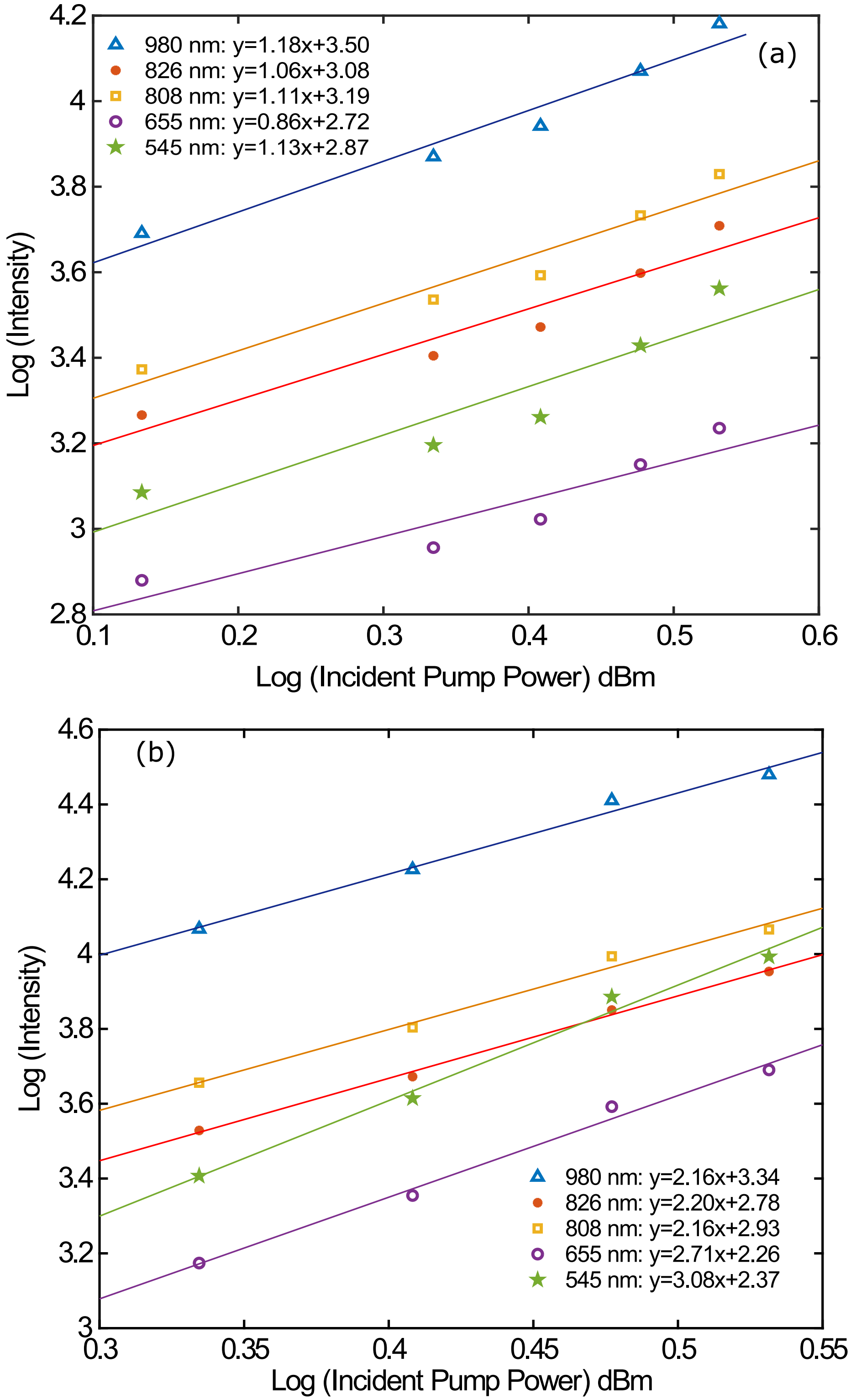

Figure D4: Power dependence of different emission bands for excitation wavelengths (a) 1520 nm, and (b) >1200 nm. Incident laser is 1 mm diameter.

of this scheme for enhancing solar cell performance.

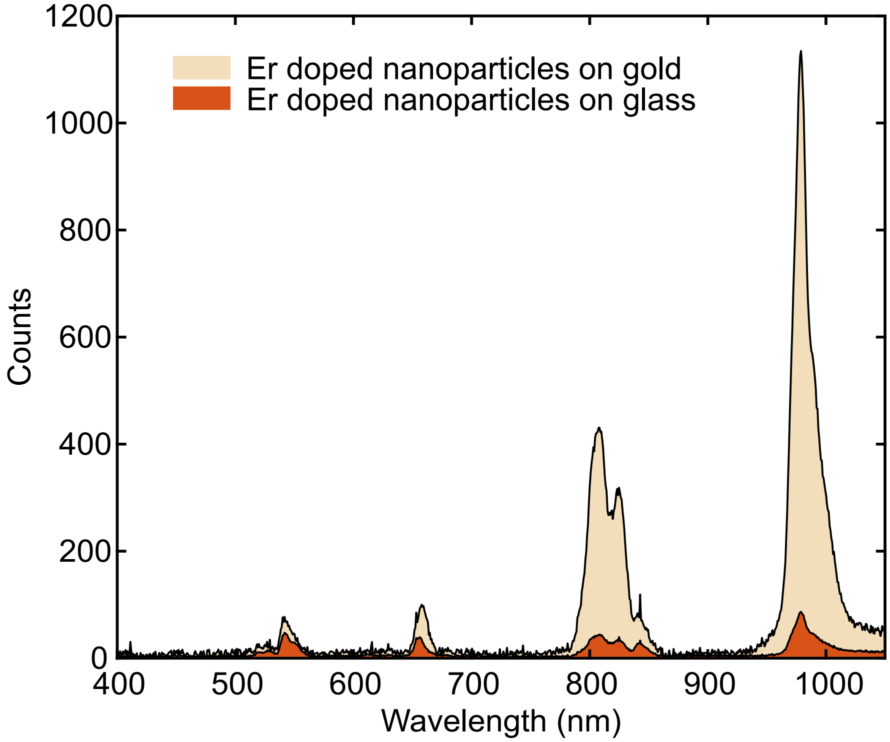

Figure D5: Increase in upconversion emission when drop coating on gold as compared with glass.

Figure D5 shows the spectra for the Er doped nanoparticles drop coated on glass and on gold for excitation >1200 nm. The gold enhances the upconverted emission by approximately doubling the local magnetic field at the surface and reflecting photons that would have been emitted preferentially into the glass substrate.(D46)–(D50) The 980 nm emission increased by a factor of 13 when drop-coating on gold as compared to on glass.

Figure D6 shows additional plasmonic enhanced upconversion when nanorods are drop-coated on top Er doped nanoparticles. Both 808 nm (E12-25-808-NPO-HEX-50, NanoPartz) and 980 nm nanorods (E12-25-980-NPO-HEX-50, NanoPartz) were used. The 980 nm nanorods selectively enhanced emission from the 980 nm band and the 808 nm Er doped nanoparticles selectively enhanced emission from the 808 nm band. (We also studied only >1500 nm excitation, and the reduction in emission is

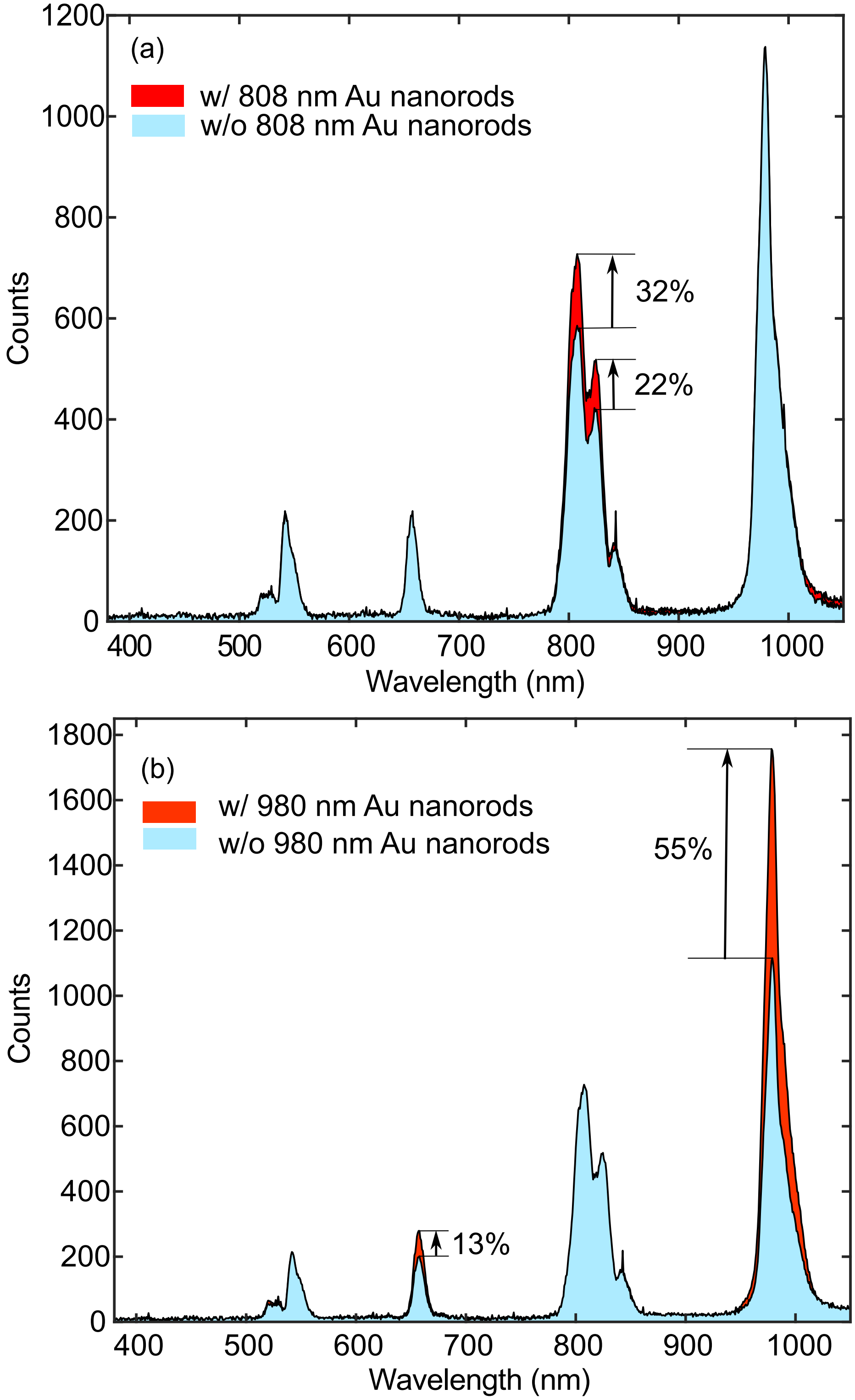

Figure D6: (a) Enhanced upconversion at 808 nm when using 808 nm nanorods. (b) Enhanced upconversion at 980 nm when using 980 nm nanorods.

similar to found in solution of Fig. D2, so not presented here). In Figure D6(b), the enhancement at 980 nm is 55% with none shown at 808 nm. Detailed permutations were not attempted. We did, however, try one additional run in which the nanorod density was increased by a factor of four and the enhancement doubled for emission at 980 nm. There is a moderate enhancement at 655 nm which is interesting because the nanorods do not show a plasmonic resonance in the extinction spectrum for that wavelength. We have investigated this further by finite-difference time-domain simulation and found that there is a dark mode plasmonic resonance at that wavelength (see Supporting Information).

The nanorods have little influence for the excitation beam because the incident wavelength range is greater than 10 times the size of the nanorods (well into the Rayleigh regime) and also well away from the plasmonic resonance. Therefore, the main function of the nanorods is to selectively enhance the emission rate at the plasmonic resonance. There is also expected to be some enhancement in the outward scattering and absorption by the nanorods themselves. The relatively contributions of these different factors will require more precise control of the relative placement of the nanorods and the Er doped nanoparticles. The present scheme merely identifies that there is plasmon selective enhancement of the detected emission. We note that the ratio of Er doped nanoparticles to nanorods is ∼15000:1; therefore, we expect that most of the Er doped nanoparticles are not in the vicinity of the plasmon hotspot. Controlled placement of the Er doped nanoparticles is required to fully quantify the plasmonic enhancement.(D51)–(D57)

In addition, it is possible to consider adding plasmonic resonances at 1520 nm and 1210 nm to enhance the absorption processes. We note that Figure D4 shows we are not in the saturated regime for either of the excitation bands, and therefore greater conversion efficiency is expected by enhancing the absorption efficiency at those wavelengths as well. We also observe a small amount of blue upconversion (see Supporting Information); however, this is weak because we are not in the strong excitation regime and blue upconversion requires four photon absorption at 1520 nm.

In conclusion, we have investigated dual-band upconversion that uses two of the IR solar bands at 1210 nm and 1520 nm by sequential absorption. We demonstrated that nanorods could be used to selectively enhance the upconverted wavelengths of 980 nm and 808 nm, which is of interest to silicon and GaAs solar cell technologies. In the present scheme, we have not optimized the coupling of the plasmonic resonance to the Er doped nanoparticles, and further work is required to quantify this effect to determine whether it can provide significant benefit for solar harvesting applications. It is interesting to use this upconversion scheme because the harvested bands are outside of the region of the usual silicon solar cells, and so the upconverting material with plasmonic enhancement may be placed at the back electrode of the solar cell without degrading in-band incident photons before they interact with the absorbing region.

Experimental Methods

$NaYF_4$: 2% Er Chemicals

Yttrium(III) chloride hexahydrate (99.99%), erbium(III) chloride hexahydrate (99.995%), ammonium fluoride (99.99%), tech grade oleic acid (90%), tech grade 1-octadecene (90%), and hexanes were purchased from Sigma-Aldrich. Anhydrous ethanol from Commercial Alcohols, methanol from Caledon, and sodium hydroxide from Bio Basic Canada inc. were used. All chemicals were used as received.

Synthesis

A synthesis was adapted from a previously reported procedure.(D58) In a 100 mL three-neck round-bottom flask, 300 mg $YCl_3{\cdot}(H_2O)_6$ and 8 mg $ErCl_3{\cdot}(H_2O)_6$ are added to 15 mL 1-octadecene and 6 mL oleic acid. The mixture was heated to 160 °C under vacuum and kept at that temperature for 30 minutes before cooling to room temperature. Once cooled, a solution of 100 mg sodium hydroxide and 148 mg ammonium fluoride in 10 mL methanol is added dropwise while stirring. The mixture was heated to 70 °C for 60 minutes to evaporate the methanol. The mixture was put under a blanket of argon and the temperature was raised to 300 °C over 15 minutes. The temperature was kept between 295 and 305 °C for 60 minutes. The reaction mixture was then cooled, washed with 20 mL ethanol, centrifuged at 1800 g for 10 min, and washed with 20 mL ethanol again before dispersing the particles in 20 mL hexane. We have performed X-ray diffraction and transmission electron microscope for the characterization of Er doped nanoparticles, as detailed in the Supporting Information.

Measurements

For the solution-based measurements 14.4 mg/mL Er doped nanoparticles in hexane were placed in a quartz cuvette and illuminated with supercontinuum source (Fianium SC400). The maximum integrated intensity of the source was 0.4 W/cm^2. A prism and slit, neutral density filter (NE10A, Thorlabs) as well as bandpass filter (FEL 1200, Thorlabs) were used to select desired bands of excitation. The excitation spectrum was measured with a fiber-based near-IR spectrometer (Ocean Optics NIR512). The emission spectrum was measured with a fiber-based spectrometer (Ocean Optics QE65000) with ten seconds integration. A 2.3 cm focal length lens was used for coupling to the spectrometer. For the substrate-based measurements, 8 drops of 8 μL were dropped on microslides (LAB-033, Bio Nuclear Diagnostics) and gold-on-glass (EMF CA134), allowing to dry between each drop. For the 808 nm gold nanorods in hexane (E12-25-808-NPO-HEX-50, Nanopartz), or 980 nm gold nanorods in hexane (E12-25-980-NPO-HEX-50, Nanopartz) were drop-coated after the first four drops of Er doped nanoparticles, and this was followed with 4 more drops of Er doped nanoparticles. Gentle mixing on the surface was performed after each drop. Detailed permutations were not attempted.

Associated content

Supporting Information

Er doped nanoparticles X-ray diffraction characterization, Er doped nanoparticles transmission electron microscope, size distribution of Er doped nanoparticles, spectrum of upconversion emission at 411 nm, finite difference time domain modeling for electrical field intensity around gold nanorods.

Author Information

Corresponding Author

*E-mail (R. Gordon): rgordon@uvic.ca

Author Contributions

M.S.S. prepared and measured the samples. A.K. and A.A. assisted in the measurements. A.L.F. synthesized and characterized the nanoparticles under the supervision of F.v.V. R.G. supervised the project, providing ideas and facilities and performed the simulations. All authors contributed to writing the manuscript.

ORCID

Reuven Gordon: 0000-0002-1485-6067

Note

The authors declare no competing financial interest.

Acknowledgements

The authors acknowledge funding support from the NSERC CREATE program Materials for Enhanced Energy Technologies (MEET) and the NSERC Discovery Grants program.

References

[D1] Huang, X.; Han, S.; Huang, W.; Liu, X. Enhancing solar cell efficiency: the search for luminescent materials as spectral converters. *Chemical Society Reviews* **2013**, *42*, 173–201.

[D2] Hagstrom, A. L.; Deng, F.; Kim, J.-H. Enhanced triplet–triplet annihilation upconversion in dual-sensitizer systems: translating broadband light absorption to practical solid-state materials. *ACS Photonics* **2016**, *4*, 127–137.

[D3] Frazer, L.; Gallaher, J. K.; Schmidt, T. Optimizing the efficiency of solar photon upconversion. *ACS Energy Letters* **2017**, *2*, 1346–1354.

[D4] Auzel, F. Upconversion and anti-stokes processes with f and d ions in solids. *Chemical Reviews* **2004**, *104*, 139–174.

[D5] Sun, G.; Chen, R.; Ding, Y. J.; Khurgin, J. B. Upconversion due to optical-phonon-assisted anti-stokes photoluminescence in bulk GaN. *ACS Photonics* **2015**, *2*, 628–632.

[D6] Boyer, J.-C.; Vetrone, F.; Cuccia, L. A.; Capobianco, J. A. Synthesis of colloidal upconverting NaYF4 nanocrystals doped with Er3+, Yb3+ and Tm3+, Yb3+

via thermal decomposition of lanthanide trifluoroacetate precursors. *ACS Photonics* **2006**, *128*, 7444–7445.

[D7] Wu, D. M.; García-Etxarri, A.; Salleo, A.; Dionne, J. A. Plasmon-enhanced upconversion. *The Journal of Physical Chemistry Letters* **2014**, *5*, 4020–4031.

[D8] Wisser, M. D.; Fischer, S.; Maurer, P. C.; Bronstein, N. D.; Chu, S.; Alivisatos, A. P.; Salleo, A.; Dionne, J. A. Enhancing quantum yield via local symmetry distortion in lanthanide-based upconverting nanoparticles. *ACS Photonics* **2016**, *3*, 1523–1530.

[D9] Garfield, D. J.; Borys, N. J.; Hamed, S. M.; Torquato, N. A.; Tajon, C. A.; Tian, B.; Shevitski, B.; Barnard, E. S.; Suh, Y. D.; Aloni, S.; Neaton, J. B.; Chan, E. M.; Cohen, B. E.; Schuck, P. J. Enrichment of molecular antenna triplets amplifies upconverting nanoparticle emission. *Nature Photonics* **2018**, 1.

[D10] Gargas, D. J.; Chan, E. M.; Ostrowski, A. D.; Aloni, S.; Altoe, M. V. P.; Barnard, E. S.; Sanii, B.; Urban, J. J.; Milliron, D. J.; Cohen, B. E.; Schuck, P. J. Engineering bright sub-10-nm upconverting nanocrystals for single-molecule imaging. *Nature Nanotechnology* **2014**, *9*, 300.

[D11] Lin, J. H.; Liou, H. Y.; Wang, C.-D.; Tseng, C.-Y.; Lee, C.-T.; Ting, C.-C.; Kan, H.-C.; Hsu, C. C. Giant enhancement of upconversion fluorescence of NaYF4: Yb3+, Tm3+ nanocrystals with resonant waveguide grating substrate. *ACS Photonics* **2015**, *2*, 530–536.

[D12] Chan, E. M.; Gargas, D. J.; Schuck, P. J.; Milliron, D. J. Concentrating and recycling energy in lanthanide codopants for efficient and spectrally pure emission: the case of NaYF4: Er3+/Tm3+ upconverting nanocrystals. *The Journal of Physical Chemistry B* **2012**, *116*, 10561–10570.

[D13] Rabouw, F. T.; Prins, P. T.; Norris, D. J. Europium-Doped NaYF4 Nanocrystals as Probes for the Electric and Magnetic Local Density of Optical States throughout the Visible Spectral Range. *Nano Letters* **2016**, *16*, 7254–7260.

[D14] Podhorodecki, A.; Misiewicz, J.; Wójcik, J.; Irving, E.; Mascher, P. 1.54 μm room temperature emission from Er-doped Si nanocrystals deposited by ECR-PECVD. *Journal of Luminescence* **2006**, *121*, 230–232.

[D15] Podhorodecki, A.; Zatryb, G.; Golacki, L. W.; Misiewicz, J.; Wojcik, J.; Mascher, P. On the origin of emission and thermal quenching of SRSO: Er 3+ films grown by ECR-PECVD. *Nanoscale Research Letters* **2013**, *8*, 98.

[D16] Poorkazem, K.; Hesketh, A. V.; Kelly, T. L. Plasmon-enhanced triplet–triplet annihilation using silver nanoplates. *The Journal of Physical Chemistry C* **2014**, *118*, 6398–6404.

[D17] Trupke, T.; Green, M.; Würfel, P. Improving solar cell efficiencies by up-conversion of sub-band-gap light. *Journal of Applied Physics* **2002**, *92*, 4117–4122.

[D18] Han, G.; Wang, M.; Li, D.; Bai, J.; Diao, G. Novel upconversion Er, Yb-CeO2 hollow spheres as scattering layer materials for efficient dye-sensitized solar cells. *Solar Energy Materials and Solar Cells* **2017**, *160*, 54–59.

[D19] Ramachari, D.; Esparza, D.; López-Luke, T.; Romero, V.; Perez-Mayen, L.; De la Rosa, E.; Jayasankar, C. Synthesis of co-doped Yb3+-Er3+: ZrO2 upconversion nanoparticles and their applications in enhanced photovoltaic properties of quantum dot sensitized solar cells. *Journal of Alloys and Compounds* **2017**, *698*, 433–441.

[D20] Chen, X.; Xu, W.; Song, H.; Chen, C.; Xia, H.; Zhu, Y.; Zhou, D.; Cui, S.; Dai, Q.; Zhang, J. Highly Efficient LiYF4: Yb3+, Er3+ Upconversion single crystal under solar cell spectrum excitation and photovoltaic application. *ACS Applied Materials & Interfaces* **2016**, *8*, 9071–9079.

[D21] Yan, C.; Dadvand, A.; Rosei, F.; Perepichka, D. F. Near-IR photoresponse in new up-converting CdSe/NaYF4: Yb, Er nanoheterostructures. *Journal of the American Chemical Society* **2010**, *132*, 8868–8869.

[D22] Huang, Y.; Hemmer, E.; Rosei, F.; Vetrone, F. Multifunctional liposome nanocarriers combining upconverting nanoparticles and anticancer drugs. *The Journal of Physical Chemistry B* **2016**, *120*, 4992–5001.

[D23] Chen, G.; Ohulchanskyy, T. Y.; Kachynski, A.; Ågren, H.; Prasad, P. N. Intense visible and near-infrared upconversion photoluminescence in colloidal LiYF4: Er3+ nanocrystals under excitation at 1490 nm. *ACS Nano* **2011**, *5*, 4981–4986.

[D24] Shalav, A.; Richards, B.; Trupke, T.; Krämer, K.; Güdel, H.-U. Application of NaYF 4: Er 3+ up-converting phosphors for enhanced near-infrared silicon solar cell response. *Applied Physics Letters* **2005**, *86*, 013505.

[D25] Ivanova, S.; Pellé, F. Strong 1.53 μm to NIR-VIS-UV upconversion in Er-doped fluoride glass for high-efficiency solar cells. *JOSA B* **2009**, *26*, 1930–1938.

[D26] Fischer, S.; Johnson, N. J.; Pichaandi, J.; Goldschmidt, J. C.; van Veggel, F. C. Upconverting core-shell nanocrystals with high quantum yield under low irradiance: On the role of isotropic and thick shells. *Journal of Applied Physics* **2015**, *118*, 193105.

[D27] Shao, W.; Chen, G.; Damasco, J.; Wang, X.; Kachynski, A.; Ohulchanskyy, T. Y.; Yang, C.; Ågren, H.; Prasad, P. N. Enhanced upconversion emission in colloidal (NaYF 4: Er 3+)/NaYF 4 core/shell nanoparticles excited at 1523 nm. *Optics letters* **2014**, *39*, 1386–1389.

[D28] Goh, S. C. Red, green and blue upconversions in erbium-doped fluorozirconate glass. *Journal of Non-Crystalline Solids* **1993**, *161*, 227–230.

[D29] Yoshikawa, K.; Kawasaki, H.; Yoshida, W.; Irie, T.; Konishi, K.; Nakano, K.; Uto, T.; Adachi, D.; Kanematsu, M.; Uzu, H.; Yamamoto, K. Silicon heterojunction solar cell with interdigitated back contacts for a photoconversion efficiency over 26%. *Nature Energy* **2017**, *2*, 17032.

[D30] Adachi, D.; Hernández, J. L.; Yamamoto, K. Impact of carrier recombination on fill factor for large area heterojunction crystalline silicon solar cell with 25.1% efficiency. *Applied Physics Letters* **2015**, *107*, 233506.

[D31] Green, M. A.; Hishikawa, Y.; Dunlop, E. D.; Levi, D. H.; Hohl-Ebinger, J.; Ho-Baillie, A. W. Solar cell efficiency tables (version 52). *Progress in Photovoltaics: Research and Applications* **2018**, *26*, 427–436.

[D32] Wanlass, M. Systems and methods for advanced ultra-high-performance InP solar cells. 2017; US Patent 9,590,131.

[D33] Schuck, P.; Fromm, D.; Sundaramurthy, A.; Kino, G.; Moerner, W. Improving the mismatch between light and nanoscale objects with gold bowtie nanoantennas. *Physical Review Letters* **2005**, *94*, 017402.

[D34] Pelton, M.; Aizpurua, J.; Bryant, G. Metal-nanoparticle plasmonics. *Laser & Photonics Reviews* **2008**, *2*, 136–159.

[D35] Anger, P.; Bharadwaj, P.; Novotny, L. Enhancement and quenching of single-molecule fluorescence. *Physical Review Letters* **2006**, *96*, 113002.

[D36] Hoang, N.-V.; Pereira, A.; Nguyen, H. S.; Drouard, E.; Moine, B.; Deschamps, T.; Orobtchouk, R.; Pillonnet, A.; Seassal, C. Giant Enhancement of

Luminescence Down-Shifting by a Doubly Resonant Rare-Earth-Doped Photonic Metastructure. *ACS Photonics* **2017**, *4*, 1705–1712.

[D37] Michieli, N. T.; Kalinic, B.; Scian, C.; Cesca, T.; Mattei, G. Emission Rate Modification and Quantum Efficiency Enhancement of Er3+ Emitters by Near-Field Coupling with Nanohole Arrays. *ACS Photonics* **2018**,

[D38] Rafiei Miandashti, A.; Kordesch, M. E.; Richardson, H. H. Effect of Temperature and Gold Nanoparticle Interaction on the Lifetime and Luminescence of NaYF4: Yb3+: Er3+ Upconverting Nanoparticles. *ACS Photonics* **2017**, *4*, 1864–1869.

[D39] Huang, Y.; Rosei, F.; Vetrone, F. A single multifunctional nanoplatform based on upconversion luminescence and gold nanorods. *Nanoscale* **2015**, *7*, 5178–5185.

[D40] Zhang, H.; Li, Y.; Ivanov, I. A.; Qu, Y.; Huang, Y.; Duan, X. Plasmonic modulation of the upconversion fluorescence in NaYF4: Yb/Tm hexaplate nanocrystals using gold nanoparticles or nanoshells. *Angewandte Chemie* **2010**, *122*, 2927–2930.

[D41] Naik, G. V.; Welch, A. J.; Briggs, J. A.; Solomon, M. L.; Dionne, J. A. Hot-carrier-mediated photon upconversion in metal-decorated quantum wells. *Nano letters* **2017**, *17*, 4583–4587.

[D42] Chen, H.; Shao, L.; Li, Q.; Wang, J. Gold nanorods and their plasmonic properties. *Chemical Society Reviews* **2013**, *42*, 2679–2724.

[D43] Pollnau, M.; Gamelin, D. R.; Lüthi, S.; Güdel, H.; Hehlen, M. Power dependence of upconversion luminescence in lanthanide and transition-metal-ion systems. *Physical Review B* **2000**, *61*, 3337.

[D44] Schulze, T. F.; Schmidt, T. W. Photochemical upconversion: present status and prospects for its application to solar energy conversion. *Energy & Environmental Science* **2015**, *8*, 103–125.

[D45] Boyer, J.-C.; Van Veggel, F. C. Absolute quantum yield measurements of colloidal NaYF 4: Er3+, Yb3+ upconverting nanoparticles. *Nanoscale* **2010**, *2*, 1417–1419.

[D46] Kalkman, J.; Kuipers, L.; Polman, A.; Gersen, H. Coupling of Er ions to surface plasmons on Ag. *Applied Physics Letters* **2005**, *86*, 041113.

[D47] Karaveli, S.; Zia, R. Strong enhancement of magnetic dipole emission in a multilevel electronic system. *Optics letters* **2010**, *35*, 3318–3320.

[D48] Karaveli, S.; Zia, R. Spectral tuning by selective enhancement of electric and magnetic dipole emission. *Physical Review Letters* **2011**, *106*, 193004.

[D49] Li, D.; Jiang, M.; Cueff, S.; Dodson, C. M.; Karaveli, S.; Zia, R. Quantifying and controlling the magnetic dipole contribution to 1.5- μ m light emission in erbium-doped yttrium oxide. *Physical Review B* **2014**, *89*, 161409.

[D50] Mertens, H.; Polman, A. Plasmon-enhanced erbium luminescence. *Applied Physics Letters* **2006**, *89*, 211107.

[D51] Ma, L.-C.; Subramanian, R.; Huang, H.-W.; Ray, V.; Kim, C.-U.; Koh, S. J. Electrostatic funneling for precise nanoparticle placement: a route to wafer-scale integration. *Nano letters* **2007**, *7*, 439–445.

[D52] Imura, K.; Okamoto, H.; Hossain, M. K.; Kitajima, M. Visualization of localized intense optical fields in single gold- nanoparticle assemblies and ultrasensitive Raman active sites. *Nano letters* **2006**, *6*, 2173–2176.

[D53] Toderas, F.; Baia, M.; Baia, L.; Astilean, S. Controlling gold nanoparticle assemblies for efficient surface-enhanced Raman scattering and localized surface plasmon resonance sensors. *Nanotechnology* **2007**, *18*, 255702.

[D54] Saboktakin, M.; Ye, X.; Oh, S. J.; Hong, S.-H.; Fafarman, A. T.; Chettiar, U. K.; Engheta, N.; Murray, C. B.; Kagan, C. R. Metal-enhanced upconversion luminescence tunable through metal nanoparticle–nanophosphor separation. *ACS Nano* **2012**, *6*, 8758–8766.

[D55] Schietinger, S.; Aichele, T.; Wang, H.-Q.; Nann, T.; Benson, O. Plasmon-enhanced upconversion in single NaYF4: Yb3+/Er3+ codoped nanocrystals. *Nano letters* **2009**, *10*, 134–138.

[D56] Zhang, W.; Ding, F.; Chou, S. Y. Large Enhancement of Upconversion Luminescence of NaYF4: Yb3+/Er3+ Nanocrystal by 3D Plasmonic Nano-Antennas. *Advanced Materials* **2012**, *24*.

[D57] Verhagen, E.; Kuipers, L.; Polman, A. Field enhancement in metallic subwavelength aperture arrays probed by erbium upconversion luminescence. *Optics Express* **2009**, *17*, 14586–14598.

[D58] Li, Z.; Zhang, Y. An efficient and user-friendly method for the synthesis of hexagonal-phase NaYF4: Yb, Er/Tm nanocrystals with controllable shape and upconversion fluorescence. *Nanotechnology* **2008**, *19*, 345606.

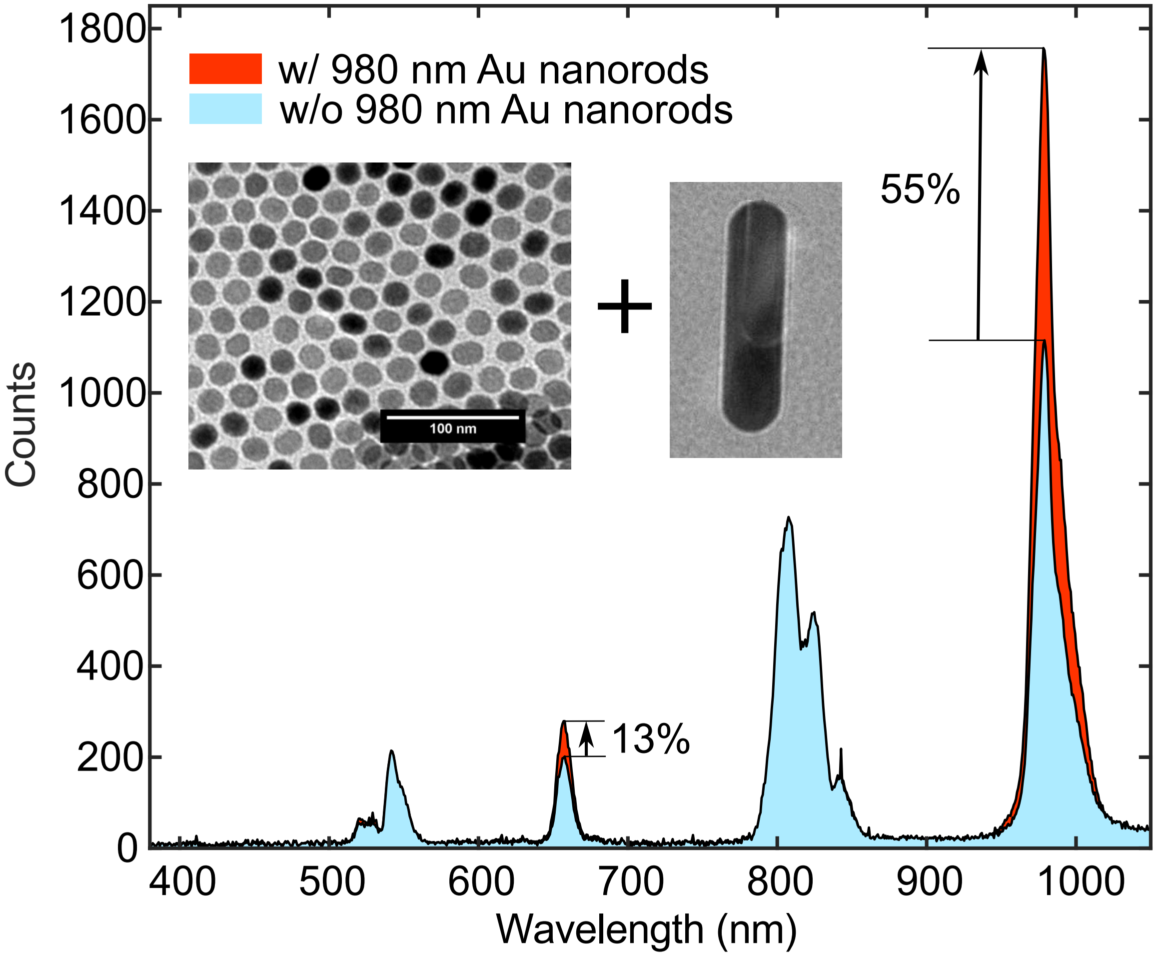

Table of contents figure: Dual band (1210 nm and 1520 nm) wavelength absorption of upconverting nanoparticles enhanced by plasmonic nanorods selectively for emission at 980 nm and 808 nm. TEM figure of nanorod provided by Nanopartz.

Supporting information for : Harvesting dual-wavelength excitation with plasmon-enhanced emission from upconverting nanoparticles

Mirali Seyed Shariatdoust,[†,§] Adriaan L. Frencken,[‡,§] Ali Khademi,[¶,§] Amirhossein Alizadehkhaledi,[¶,§] Frank C.J.M. van Veggel,[‡,§] and Reuven Gordon*,[¶,§]

†*Department of Electrical and Computer Engineering, University of Victoria, Victoria, British Columbia V8P 5C2, Canada*

‡*Department of Chemistry, University of Victoria, British Colombia V8W 3V6, Canada*

¶*Department Electrical and Computer Engineering, University of Victoria, Victoria, British Columbia V8P 5C2, Canada*

§*Center for Advanced Materials & Related Technologies (CAMTEC), University of Victoria, Victoria, British Columbia V8W 2Y2, Canada*

E-mail: rgordon@uvic.ca

Phone: +1 250 472 5179 . Fax: +1 250 721 6052

Figure D-S1 shows X-ray diffraction for phase analysis and confirmation of NaYF4: 2% in nano particles. X-ray diffractograms with a resolution of $0.0263^{c}irc2\theta$ were collected using a PANalytical Empyrean X-ray System with a Cu source (Kα radiation,

$\lambda = 1.54060$ Å) operating at 45 kV and 40 mA.

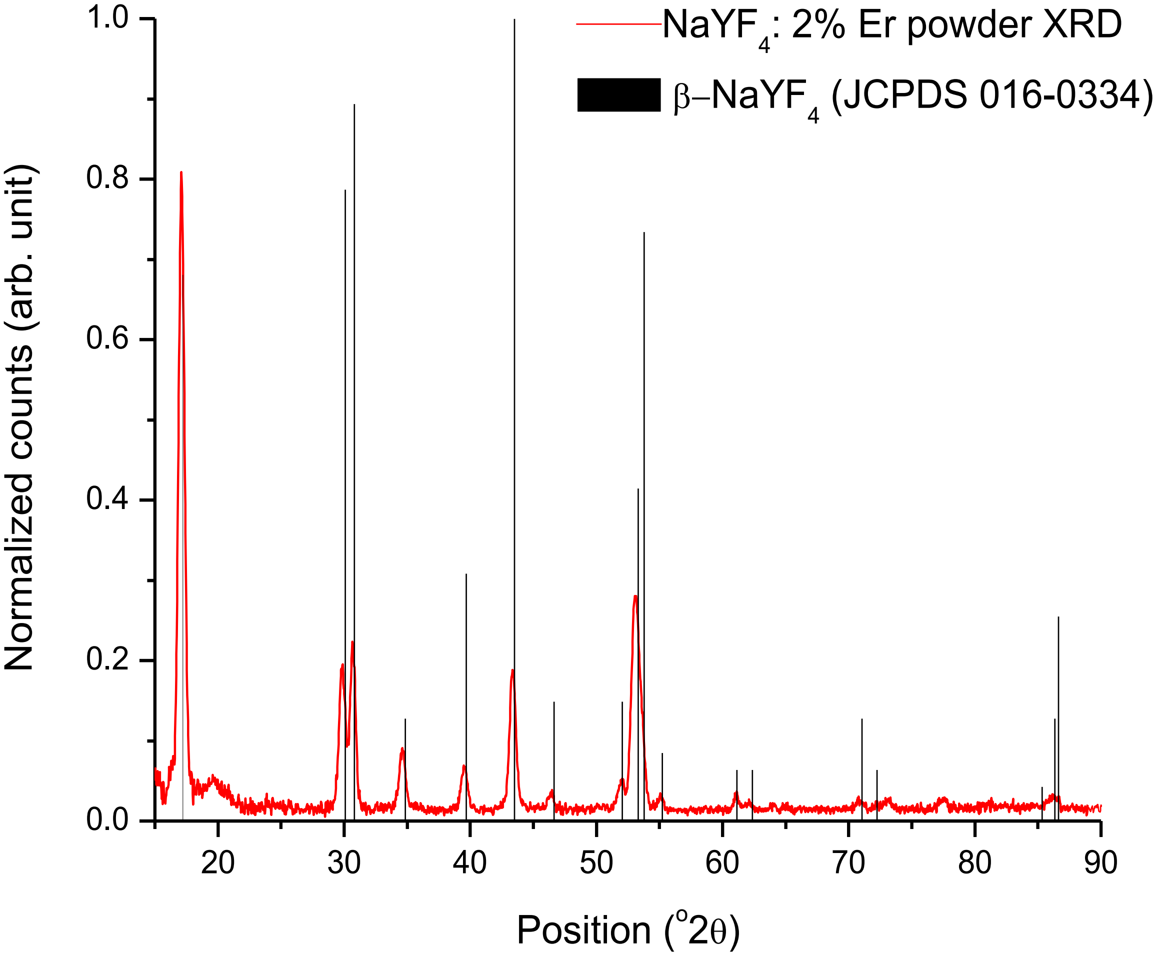

Figure D-S1: Experimental x-ray diffractogram of NaYF4: 2% Er NPs and a reference pattern of hexagonal NaYF4

Figure D-S2 depicts transmission electron microscopy of the spherical NaYF4: %2 upconverting nano particles under 250k times magnification. Transmission electron microscopy images were obtained using a JEOL JEM-1400 microscope operating at 80 kV. Hexane dispersions of the NPs were drop-cast on a Formvar carbon- oated grid (300 mesh Cu) and air-dried before imaging.

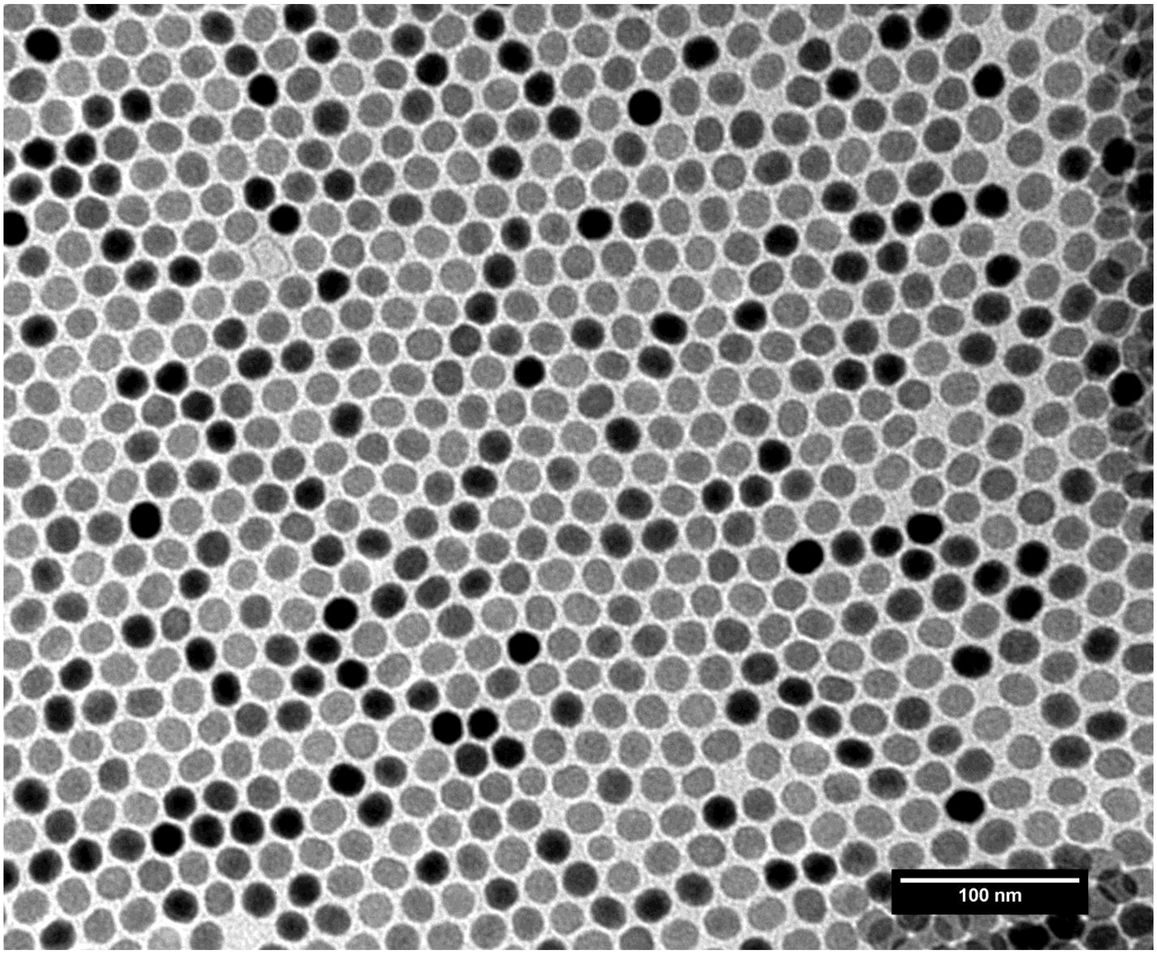

Figure D-S2: Representative TEM image of NaYF4: 2% Er nanoparticles magnified 250k times.

Figure D-S3 illustrates UCNPs size distribution in hexane. Size analysis of NCs from the images was performed by measuring the surface area of at least 800 particles.

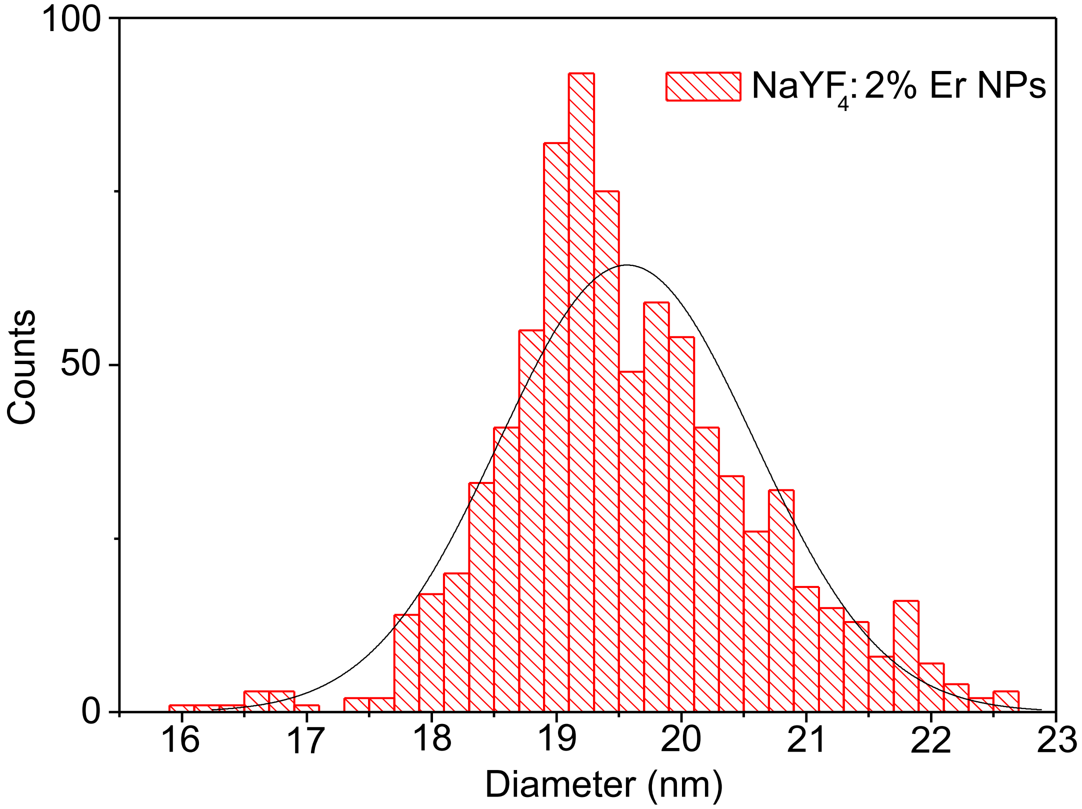

Figure D-S3: Size distribution of measured NaYF4: 2% Er NPs with a mean diameter of 19.56 nm and standard deviation 1.02 nm.

Figure D-S4 depicts weak peak around 410 nm for Er UCNPs while hey where drop casted on the gold surface, since the intensity of this peak in low in comparison to other peaks considering Er energy states as well we can conclude that four photon upconversion process happened. Due to low pump power for four photon upconversion process the detected peak has very low intensity.

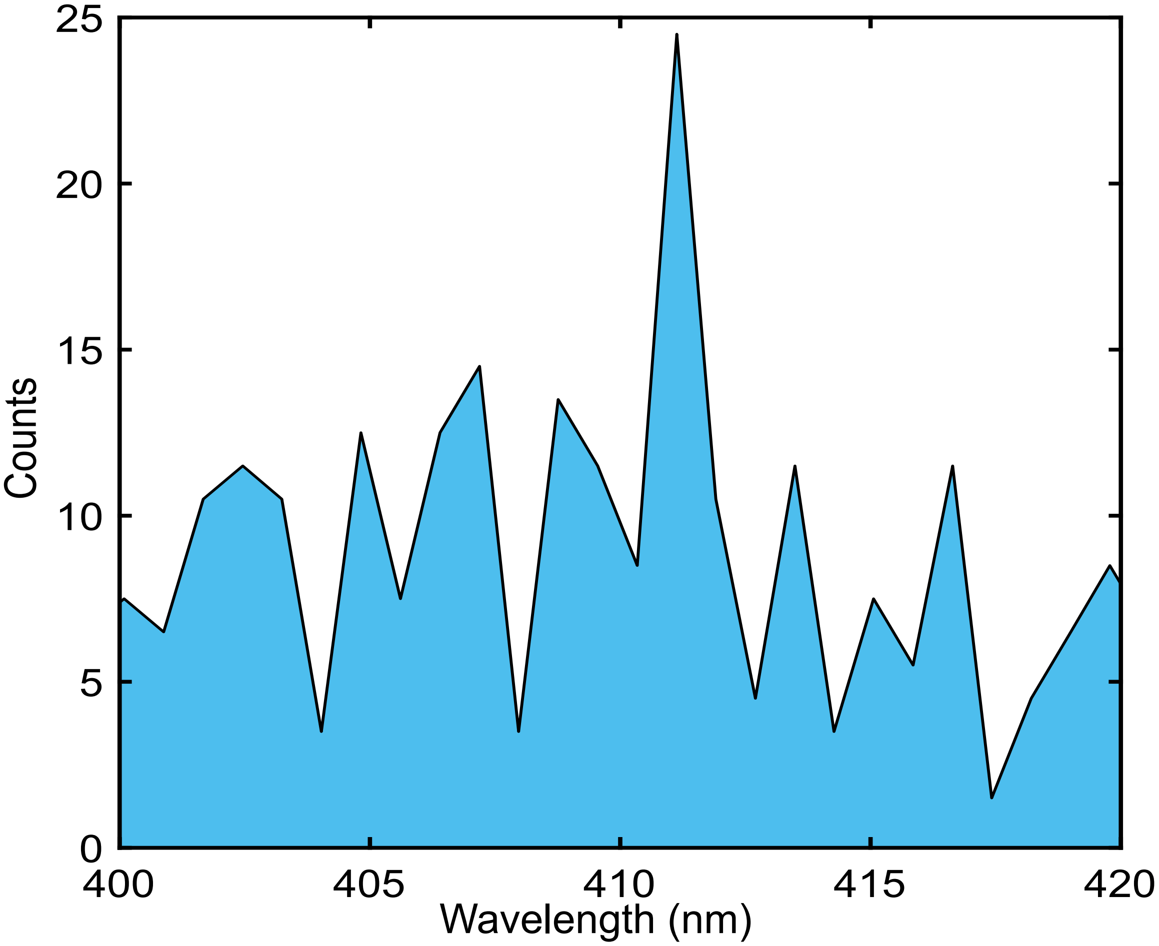

Figure D-S4: Weak upconversion emission at 411 nm.

Figure D-S5 shows the 3D simulation of a gold nanorod using finite-difference time-domain (FDTD) analysis, Lumerical Solutions Inc., release 2017b, version 8.18.1365. Uniform mesh type with staircase mesh refinement was chosen. The mesh size was set to 1 nm in x, y, and z directions. The FDTD simulation region had a length of 0.1 μm in the x direction, 0.2 μ the y direction, and 0.1 μm in the z direction with PML boundary conditions. The field monitor geometry was 2D-Z normal with dimensions

0.1 μm×0.15 μm. We used an electricdipole source with wavelength range from 400 to 1100 nm, located 70 nm away from thetip of the gold nanorod. The monitor collected the data for 100 wavelength points at theother side of the nanorod. The time stability factor was 0.99 and auto shutoff condition was 1×10^5. The field is enhanced at 658 nm and 994 nm, and significantly less so at 812 nm.The peak of the dark mode resonance of 980 nm gold nanorods occurs at 658 nm and it has a full width at half maximum of 45 nm. Therefore, the 655 nm emission band occurs inside this resonance region

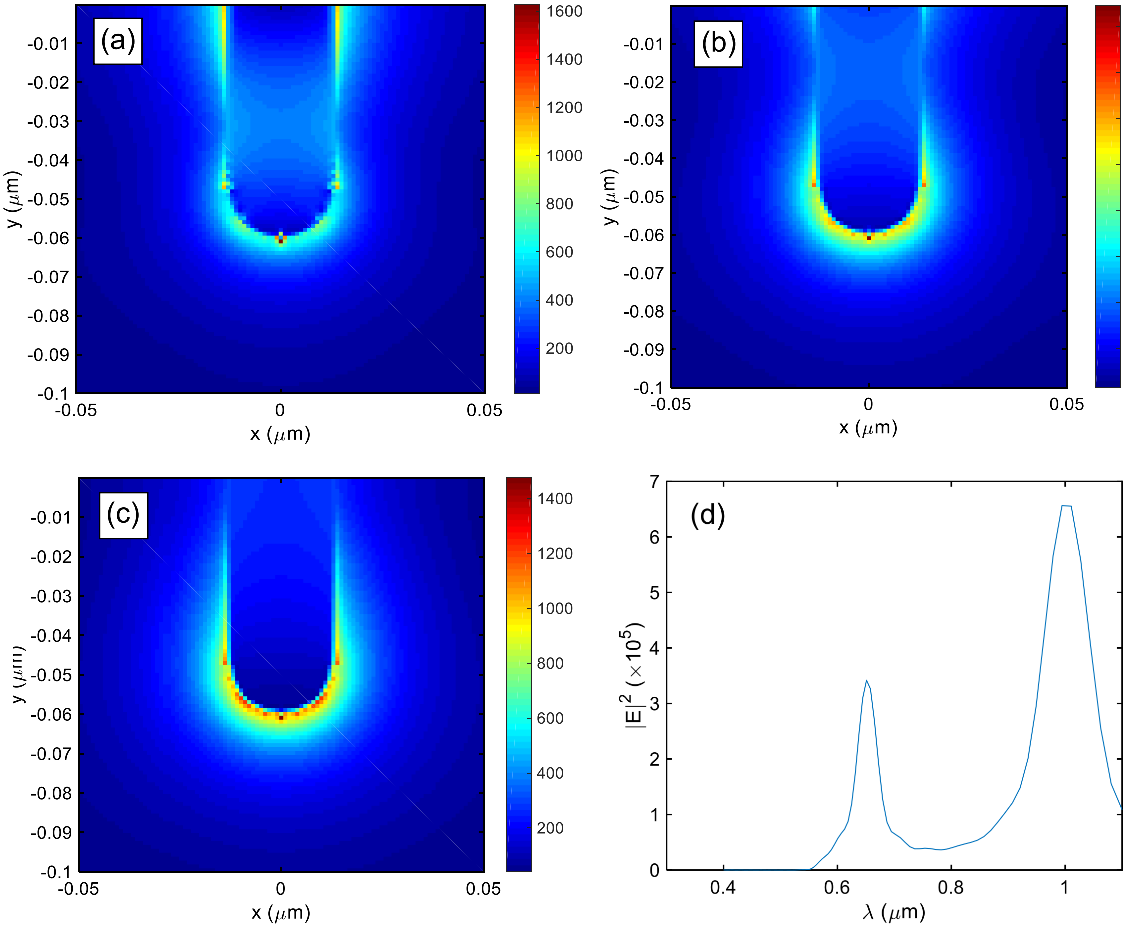

Figure D-S5: Finite differential time domain modeling for electrical field of gold nanorods in (a): 658 nm, (b): 812 nm, (c): 994 nm, (d): field enhancement close to gold nanorods in 300-1100 nm spectrum.